The University Of Sheffield.

Materials Discovery for Next Generation Li-ion Batteries

Submitted for degree of Doctor of Philosophy by

J Clough

2022

Materials Discovery for Next Generation Batteries

Submitted for the degree of Doctor of Philosophy

By Jasmin Clough

Department of Materials Science and Engineering

September 2022

ACKNOWLEDGEMENTS

First, I would like to thank my academic supervisors Professor Eddie Cussen and Professor Serena Cussen for providing excellent help and advice with this research, particularly Eddie for his patience and guidance throughout my PhD. The whole Cussen research group provided a lot of support and we always had great fun in and out of work.

Secondly, some of the research performed in my PhD was at Johnson Matthey alongside my amazing industrial supervisor Dr. Mark Feaviour, who was always helpful and provided great feedback with my reports, posters and presentations. I am also grateful for the time spent at JM alongside Mark and his colleagues, I got to perform some fun experiments and spend time in Reading.

Thirdly, I would not have gotten through the difficulty of this PhD without the support and love of all my friends in Glasgow and my family in Newcastle. Thank you for always letting me vent and providing a place for me to return to and enjoy your company and the beautiful city of Glasgow.

Finally, thank you to all the collaborators who helped with the research and to the University of Sheffield, Johnson Matthey and The Faraday institution for the research funding; without which none of this research would be possible.

I would like to give credit to those who completed work on my behalf, firstly Dr. Elvis Shoko and Dr Matthew Dyer at the university of Liverpool who performed and analysed the ab-initio molecular dynamics on the $Li_3Fe(MoO_4)_3$ material in Chapter 5 and generated Figure 4.12 Secondly, Alan Chadwick (Diamond light source reward of beam time as part of BAG SP14239) and his team for providing time for my cycled $Li_3Fe(MoO_4)_3$ material, the XAS data was crucial for understanding the role of Mo^{6+} in this material. Thirdly, Dr Laura Wheatcroft for performing TEM on my $Li_{2.2}Mn_{1.6}(MoO_4)_3$ samples and providing the image. Finally, I would like to acknowledge my JM supervisor for connecting me with S.Day and G. Goodlet who performed, analysed and provided figures for the SSNMR and EDX SEM, respectively, in Chapter 3 for my doped $LiTa_2PO_8$ samples.

Table of Contents

ABSTRACT

An increased use of electric vehicles and the need to store energy generated from intermittent sustainable power sources have given renewed urgency in the search for enhanced performance battery materials. [1] All-solid state batteries offer one solution to the safety concerns posed by conventional lithium-ion batteries, by using a solid fast Li-ion conductor in place of the flammable liquid electrolyte. When a Li-metal anode is used within an all-solid state battery, an increase in energy density and stability can be accomplished. [2] The limitations of commercialisation include the ionic conductivity of the solid electrolyte and the resistance associated with the electrolyte/cathode interface, therefore materials discovery covering the electrolyte as well as the electrodes can aid in the development of commercial solid state batteries. This thesis aims to investigate the structure property relationship of electrolyte and cathode materials, by changing the unit cell structure and investigating the electrochemical properties of the materials.

An investigation into doping $LiTa_{2-x}M_xPO8$ [M=Nb and Sb], a newly reported electrolyte structure, revealed a solubility limit of x~0.1 discovered via EDX SEM and XRD. An increase in bulk conductivity calculated through EIS, as well as the intrinsic activation energy calculated through SSNMR, is observed for $LiTa_{1.96}Sb_{0.04}PO_8$, in comparison to the parent $LiTa_2PO_8$ structure. This suggests further research into doping $LiTa_2PO_8$ and synthesising other family members can generate a material with an improved total conductivity of the reported structure; ~ 2 x 10^{-4} S cm^{-1} at room temperature. [3] Research into the structure and Li-ion transport properties of $Li_3Fe(MoO_4)_3$, a reported NASICON cathode material, revealed vacancies on the M3 site in the NPD, previously considered fully occupied, and ab-initio molecular dynamics exposed that these vacancies are crucial in allowing Li^+ hopping to occur. [4] Its unusual behaviour as a cathode is captured in the galvanostatc discharge of this material and XAS reveals Mo^{6+} does not play a role in the large capacity observed, instead the parent structure decomposes giving way to a mixture of structures which can be cycled thereafter. The parent structure, $Li_3Fe(MoO_4)_3$, has a smaller electrochemical window than isostructural materials however can provide a discharge capacity ~ 100% of its theoretical capacity.

CHAPTER 1: INTRODUCTION

1.1 Batteries

1.1.1 Conventional batteries

Batteries are electrochemical energy storage devices; they convert chemical energy into electrical energy. The main components of a battery include a cathode and anode connected via an electrolyte, the cathode and anode are then connected to an external circuit in which electrons flow. A conventional cell is made with a liquid electrolyte which connects the cathode and anode, therefore all cells suffer with interfacial redox reactions which occur simultaneously over both surfaces. [5] The redox reactions cause electrons to flow through the external circuit producing electricity to power devices such as phones. To date, this type of technology has sustained its demand, however, the need for batteries with improved performance has increased as we move from fossil fuels to more sustainable sources of electricity. Batteries now need to store a greater amount of energy whilst also becoming lighter and smaller and this leads to a demand for research into new battery materials including cathode, anode and electrolyte, which can increase the power provided. [6] Typical forms of renewable energy like solar and wind energy are intermittent or unreliable and often times when energies are at their highest does not correspond to peak times of electricity demand; grid storage is therefore needed to optimize supply and demand of electricity. For battery technology to reach this level it must provide increased performance (cycle life, energy density, efficiency), decreased cost and decreased safety concerns. [7]

Goodenough and colleague's [8] worked on a rechargeable alkali-ion cell which used an aqueous cathode and solid electrolyte, giving a cell with high electrical efficiency at room temperature. This cell does not consist of typical materials used in conventional cells, two porous electrodes connected with a liquid electrolyte, this research showed that new ideas can lead to cells which satisfy many of the criteria needed to meet the demand of new electrochemical energy storage systems. This cell still suffers limitations particularly regarding the anode and the need for thinner materials. An "Ideal" battery would ultimately satisfy all criteria and this is a long list of demands, it is more likely that future energy storage will be a combination of electrochemical

devices including fuel cells, batteries and capacitors. [9] For this to occur, battery technology must still provide greater energy density (volumetric, $WhKg^{-1}$, gravimetric, $WhrL^{-1}$), stability (Chemical, material, thermal), temperature range (operating conditions) and cycle life (ability to maintain capacity), the first step in this task would be to consider the materials needed.

Li-ion batteries are used in a wide variety of applications including portable electronics, electric vehicles and within medical devices and were developed by Sony in 1991. [10] Li-ion technology provided a solution to the demand for increased energy density and smaller batteries; a similar problem faced today. To date, Li-ion technology has the most favourable characteristics needed in a battery including long cycle life and high energy density in comparison to other technologies such as lead-acid. [1] However, Li-ion batteries still have limitations including safety issues, cost and sustainability problems. [11] Minimizing these issues in Li-ion batteries is the next step in battery research and will pave the way for future technologies including Li-air and Li-S technologies. Materials which make up the battery require the most research as the chemistry occurring at interfaces can cause unwanted side reactions which can lead to capacity fade. The electrolyte also causes the greatest safety concern as it includes flammable organic or polymer liquids and when used in the battery short circuits and fires can occur. [12] These key issues must be addressed as demand for large scale energy storage and electric vehicle growth increases.

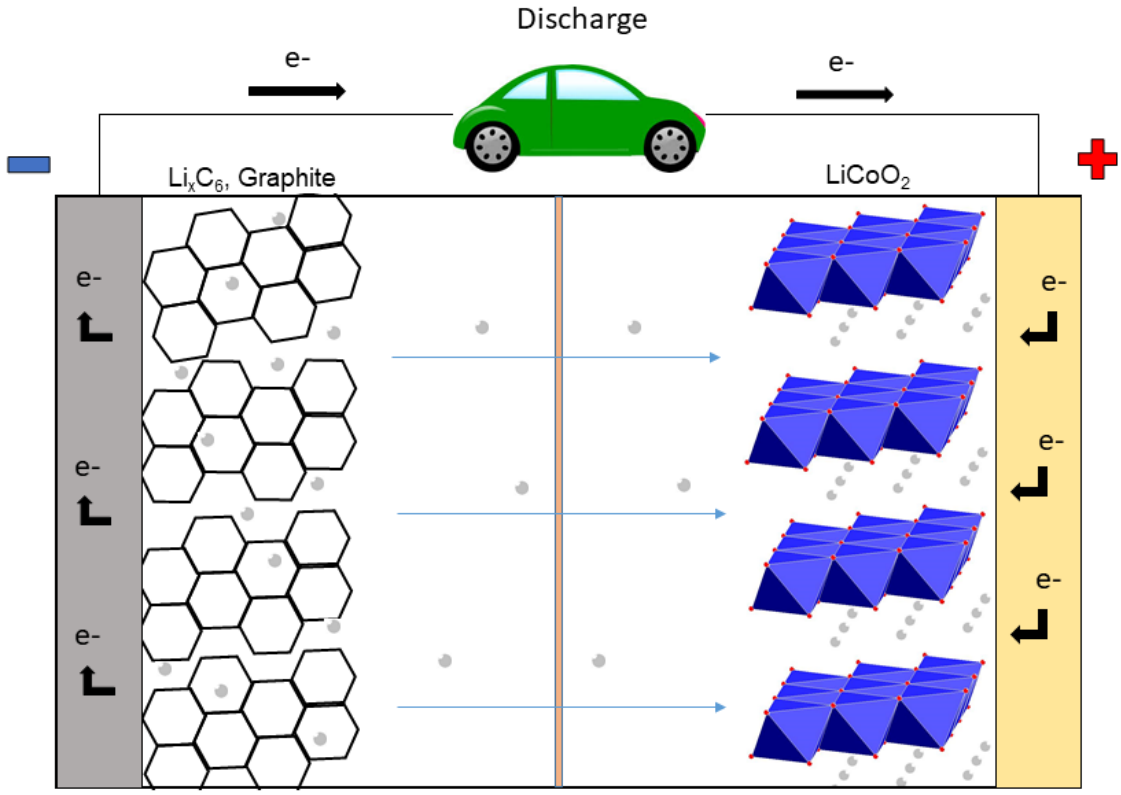

Figure 1.1 : A conventional Li-ion cell during discharge showing migration of Li^+ (shown as grey spheres) from the anode, graphite (hexagonal sheets), to the interlayer spaces of a rock salt transition metal oxide, cathode (blue octahedra).

A conventional Li-ion cell (**Figure 1.1**) is made up of a graphite anode, a layered oxide cathode such as $LiCoO_2$, a liquid electrolyte and a separator. The liquid electrolyte consists of a Li-ion salt, usually $LiPF_6$, and an organic carbonate solvent. During discharge, Li-ions de-intercalate from the graphite anode move through the electrolyte and intercalate into a layered oxide cathode. To balance the charge across the cell, the electrons released from the anode move through the external circuit creating electricity. [13] Over time, the lithium intercalation/ de-intercalation mechanism causes a loss of active material and capacity fade is experienced. [14] The conventional Li-ion battery is therefore not the safest or most efficient for use in electric vehicles or large-scale grid storage systems, the whole cell system must be further researched including the battery chemistries occurring within the cell.

As stated previously, the limitations facing the use of batteries in next generation electric vehicles is the chemical stability, energy density, safety and cost of materials

involved. [11] For current Li-ion technology the interface between the electrodes and the liquid electrolyte poses the greatest concern. When using a liquid electrolyte, a solid-electrolyte interface (SEI) is produced at the anode, this can be beneficial, when small, as it protects the anode from degradation. However, as this layer increases in size it can penetrate the separator which leads to a short circuit and thermal runaway. [15] Modifying this interface through materials discovery and selection will play a key role in moving Li-ion technology forward. Eliminating the liquid electrolyte will also solve the safety concerns, but materials must still be stable over a wide electrochemical voltage window be non-volatile and be stable at the electrode interfaces. [16] These materials should also meet the criteria needed for battery technology including lower cost, increased energy density and longer cycle life.

Li-ion battery research is ongoing and covers a wide range of chemistries some of which include all-solid state batteries, Li-S and Li-air, aqueous Li-ion technology and polymer Li-ion technology as well as a combination of these. [17, 18] Each technology has its own advantages and disadvantages. Solid state batteries offer safety, high energy densities as well as easier design and assembly options, these are limited by the conductivity of the electrolyte, the electrode-electrolyte interface and electrode stability in contact with Li metal. [19] Li-S technology offers the highest energy density, however this technology suffers with multiple side reactions leading to poor cycle life and efficiency. [20] Li-air batteries offer high energy density with the favourable material choice due to the use of O_2 from the atmosphere, unfortunately this also leads to problems with moisture in air affecting the electrodes and side reactions leading to a decrease in cycle life. [21] Aqueous technology offers high conductivity and high rate capability, however the use of water limits the electrochemical window of the cell and cycling stability in comparison to using organic electrolytes. [22] Polymer technology offers safety and flexibility, though research into the electrolyte is still needed to overcome the ionic conductivity, interfacial resistances, electrochemical window as well as preparation techniques. [18] Of these technologies, solid-state batteries have been the most extensively researched for the longest period of time hence some progress has been made in this area. [23] A combination of the above technologies is likely to solve the most drawbacks associated with utilizing Li-ion technology within electric vehicles, therefore material research is still required to meet future demands in Li-ion battery technology.

1.1.2 All-Solid State Batteries

As discussed above, the all-solid state battery eliminates the liquid electrolyte used in conventional Li-ion batteries, hence alleviates the safety concerns posed by the flammable organic electrolyte, while providing high energy densities. This technology has been in development since the 1950's but is still limited by the solid state electrolyte as this material must possess a high ionic conductivity comparable to liquid electrolytes if it is to be used commercially. [24] A high voltage battery system was first reported by Land and Bro [25] in 1969 and consisted of a Li | LiI | AgI system which could work at high voltages and used film batteries to overcome problems arising from the high resistivity of the solid electrolyte. Future energy storage requires large scale batteries to supply electric vehicles or the grid, which is driving a search for new materials capable of meeting these demands. An all-solid state battery works in the same way as a conventional battery but a solid electrolyte separates the two electrodes within the cell. This eliminates the safety concerns associated with the liquid electrolyte, but is accompanied by other limitations such as decreased ionic conductivity in the electrolyte, increased interfacial resistance and structural changes upon charge/discharge. [26] These disadvantages are mostly associated with the solid electrolyte and research has focussed on this area in recent years. [19]

Li-ion technology is still widely used today and making an all-solid-state Li-ion battery would combine the high energy density of Li-ion technology with the decreased safety aspects associated with solid state batteries. The fundamental science surrounding solid state technology can also be applied across Li-air, Li-S and polymer-based technologies, with the potential to be employed over future chemistries, such as Na-ion technology. All-solid-state Li-ion technology provides the most versatility with the earliest promise in making next generation batteries commercially accessible. The limiting factor in this technology is the electrode-electrolyte interface, due to the slow kinetics associated with solid-solid interfaces. [27] Simply increasing the ionic conductivity of the electrolyte does not provide sufficient increase to the overall Li-ion transport through the cell, and understanding the physical concepts of Li diffusion through a solid-solid interface requires further research. [28] To minimise this issue a thin film battery could be used and manufacturing of thin film solid-state Li-ion batteries

were amongst the first to be scaled-up, however they are still limited by cost of production [29] and therefore, these are not an option for large scale applications.

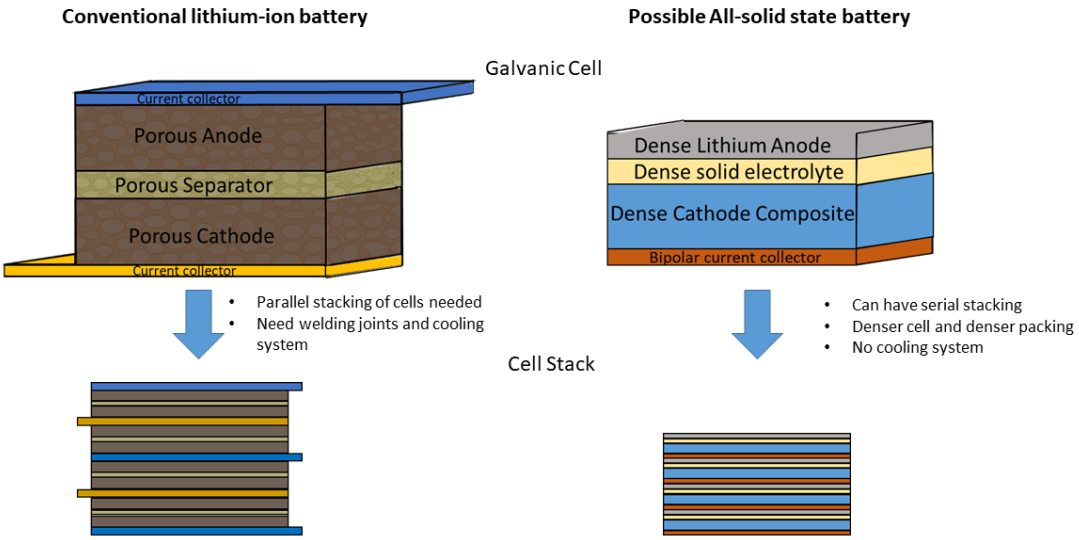

Figure 1.2: Comparison of conventional Li-ion technology against a possible next generation all-solid state Li-ion cell pack.[2]

All-solid state batteries were first used in electric vehicles in 2011, manufactured by the Bolloré group and advanced all-solid state batteries are being developed by companies including Toyota, Samsung and Sony.[30] **Figure 1.2** highlights the key battery pack design benefits of transferring Li-ion technology into an all-solid state battery system. If a lithium anode is used alongside a dense solid electrolyte the volumetric energy density of the cell can be increased by up to 70%, [2] the use of a dense solid electrolyte also provides electronic insulation between the anode and cathode, while providing less voids for dendrite growth. The composite cathode increases Li diffusion whilst limiting the interfacial resistances associated with solid-solid boundaries. Unfortunately, the Li metal used as the anode causes the growth of dendrites, which are more prominent in solid state electrolytes due to voids across particles, across the electrolyte leading to cell failure. [31, 32] The need to understand the fundamental concept of the interface and the growth of dendrites is still a key area of research in solid state batteries. [33]

The battery pack design may also differ to conventional liquid Li-ion technology as the removal of the liquid electrolyte provides the opportunity to re-engineer the cell and cell stack design. A conventional battery pack requires a cooling system to prevent fires occurring, in the case of an all-solid state battery the greater temperatures would actually increase ionic conductivity and the cooling system is no longer needed. [2] Further to this, due to less packaging needed to seal in a liquid electrolyte and the ability to generate thin film electrolytes and hence cells, the battery pack design can be engineered smaller as represented in **Figure 1.2.** Research is on-going in this area and is the next challenge in the industry, provided the materials used within the cell constrain the problems associated with interfacial issues and electrolyte conductivity. [34, 35] Ultimately, an all-solid state Li-ion battery will be smaller, safer and have an increased cycle life.

1.2 Electronic properties

1.2.1 Conductivity

Materials can be grouped depending on their electrical properties, they can be conductors, insulators or a combination of both; semiconductors. The type of conductivity a material possesses' is variable and depends on the conditions, composition and structure of the material being examined. Conductors require movement of charge carriers through a structure and this can vary depending on the amount of extrinsic and intrinsic defects present, dissolved impurities can change the defect chemistry with temperature and modify the electrical properties of materials. [36] On the other hand, pure $SrTiO_3$ is an insulator as it doesn't have enough vacancies present to conduct, however when dopants are added, it can become an electrical conductor as dopants introduce extra defects into the structure allowing ions to move. [37] Defects must be introduced to a crystal structure for conductivity to occur and this is achieved through the addition of dopants, most doping is done through adding aliovalent ions to a structure and this is most effective when the atomic radii of the dopant and parent element are similar. [38] The structure and defect chemistry of crystals is important in materials discovery as this determines the electrical behaviour of the material, introducing dopants also greatly benefits its conductivity, however understanding the mechanism of introducing dopants is still difficult.

The materials used in a battery must be capable of conductivity in order to store and release energy in the form of electricity. Ionic conductivity depends on the amount of charge carriers available in the structure and their mobility. Often the structures contain a rigid framework of a crystal which contains a mobile lattice of vacancies and interstitial sites that allow ions to move. [39] The simplest movement mechanism is considered a “hopping” mechanism and hence this sub lattice must have a low energy barrier associated with an ion moving from one vacant site to the next.

For movement to occur an ion must move from its original site to a vacant neighbouring site leaving its own site vacant, for the ion to “hop” into this new site it must overcome an energy barrier which is low enough to be feasible (activation energy), described by the Arrhenius equation. If the energy barrier is too large the ion will remain and hence conduction does not occur, however if low enough, the ion will move. For the ion to remain in this new site for a reasonable amount of time the new site should be lower in energy than the previous or the ion will simply “hop” back within seconds. [40] Hence, the minimum number of vacancies in a pure crystal may not produce the mobile framework needed for long range ion movement, or the energy required for ions to move in this sub lattice is too high for practical uses. Therefore, vacancies or interstitial sites need to be created to allow fast ionic conduction at reasonable temperatures.

Ionic conduction within solid materials has many benefits over liquid materials when used in batteries, they decrease the amount of packaging, provide stability and allow miniature batteries to be assembled. [41] Fast ionic conductors should have similar conductivities to liquid electrolytes however, solid electrolytes are ultimately temperature dependent as they require a large number of vacancies to be present. They are also diffusion-limited and grain boundaries or interfaces can decrease overall conductivities within cells. Producing materials capable of fast ionic conduction in a reliable and cost effective way also poses problems due to the high temperatures needed during synthesis, this is to create the vacancies and ordered frameworks required. [42] It is therefore important to consider low temperature synthesis and minimise the interfacial resistance within a battery, both of which can be achieved by choosing the appropriate materials for use.

1.3 Battery Materials

1.3.1 Electrolyte structures

Although ideal crystals rarely have enough vacancies to produce ionic conduction for application, fast ionic conductors (FIC's) exist, in which ions have a substantially high ion mobility. Fast ionic conduction can occur through structurally disordered solids and highly defective solids as both lead to ions being disordered within the solid in a similar manner to how ions are mobile within a liquid. [43] The major structural characteristics needed for fast ionic conduction include a highly ordered framework within which a secondary mobile sub lattice is used to support a random distribution of carrier ions. The secondary mobile framework has a high carrier density structured to minimize the activation needed for ion migration. The most promising structures for use as a solid electrolyte include NASICON, LISICON, perovskite and garnet structures. Their individual structure allows them to be utilized in room temperature applications and can give rise to various advantages and disadvantages for use as a solid electrolyte. These materials must possess high ionic conductivities at room temperature, negligible electronic conductivity and have wide electrochemical windows. [44]

One of the first families of FIC's are LISICON-type structures (LIthium Super Ionic CONductors), these are based on lithium silicate and lithium germanate compounds. The first LISICON structure was reported by Hong et al [45] with the structural formula of $Li_{16-2x}D_x(TO_4)_4$ where *D* is a divalent cation and *T* is a tetravalent cation. The highest conductivity of 1.25 x 10^{-1} S cm^{-1} at 300 ^oC was reported for the structure of $Li_{14}Zn(GeO_4)_4$, this is a high conductivity but the temperature at which this occurs is too high for use as a solid electrolyte in batteries. Research then progressed to solid solutions of γ_{II}-Li_3VO_4 and Li_4GeO_4 and LISICON type structures of composition $Li_{3+x}Ge_xV_{1-x}O_4$ were produced. [46] By doping the vanadium site with germanium, an increase in the amount of lithium is needed to maintain charge neutrality and this excess lithium sits on interstitial sites in the structure. The conductivity of $Li_{3.6}Ge_{0.6}V_{0.4}O_4$ was the highest of the compositions studied and reached 4 x 10^{-5} S cm^{-1} at 18 ^oC. This room temperature conductivity is more favourable than that of $Li_{14}Zn(GeO_4)_4$ and can be attributed to the germanium replacing vanadium causing an

increase in lithium content, unfortunately this conductivity is still too low for practical use in a solid state battery.

NASICON-type structures are similar to LISICON-type structures however, the structure and conductivity is based on sodium ions in the lattice, they have a general formula of Na$M_2(PO_4)_3$. This general structure can be modified to contain lithium, such as $LiZr_2(PO_4)_3$. This structure has a phase transition above 50 ^oC where the lattice changes from monoclinic to rhombohedral and its conductivity increases as two lithium sites are now available for conduction. The room temperature ionic conductivity of the monoclinic phase is extremely low at ~10^{-9} S cm^{-1} [47] and modification of this structure to stabilize its rhombohedral phase produces an ionic conductivity of 1 x 10^{-4} S cm^{-1} at 25 ^oC. [48] The NASICON-type structure of $LiTi_2(PO_4)_3$ showed the minimum activation energy and ionic conductivity of the structures studied by Aono et al. [49] Its low sinterability makes its bulk conductivity low at room temperature, therefore research to replace the Ti^{4+} with aliovalent ions such as aluminium took place. $Li_{1.3}Al_{0.3}Ti_{1.7}(PO_4)_3$ produced the highest conductivity of 7.8 x10^{-5} S cm^{-1}, [50] however issues arise when in contact with lithium as titanium is easily reduced making this unusable as a solid electrolyte in an all-solid state battery. [51]

Perovskites have the general formula ABO_3 and the framework is constructed of corner sharing BO_6 octahedra around a large *A* cation residing in the interstitial site. [52] Perovskites are easily doped to obtain higher conductivities such as $Li_{3/8}Sr_{7/16}Ta_{3/4}Zr_{1/4}O_3$ (LSTZ) perovskites, where the *A* and *B* cations are partially substituted, this compound allows lithium ions to move freely within the structure and this leads to a total ionic conductivity of 2.7×10^{-4} S cm^{-1} at 27 ^oC. [53] LSTZ perovskites are promising but the preparation methods require high sintering temperatures and the resulting ionic conductivity does not outweigh this cost. Research continued on these perovskite type structures including varying the tantalum content [54] and attempting to further substitute with gallium and aluminium [55] to increase the total ionic conductivity by adding vacancies into the structure and changing the bottleneck sizes for lithium diffusion. Chen et al [56] looked into creating vacancies with a compound using niobium instead of tantalum ($Li_{3/8}Sr_{7/16}Zr_{1/4}Nb_{3/4}O_3$), this also led to a lower sintering temperature of 1200 ^oC which is favourable when creating all-solid state batteries, however its total ionic conductivity was reported as 2.00×10^{-5} S cm^{-1} at 30 ^oC which is still an order of magnitude lower than that reported for

$Li_{3/8}Sr_{7/16}Ta_{3/4}Zr_{1/4}O_3$. Perovskite type structures require further research into decreasing the sintering temperatures whilst maintaining the total ionic conductivities, different synthesis techniques would benefit this research area.

Garnet type structures show the most promise for use in all-solid-state batteries as they are stable in contact with lithium and possess the highest reported ionic conductivity. Lithium containing garnets were first reported by Kasper in 1969 [57] and were reported with composition of $Li_3Ln_3M_2O_{12}$, where *M*=Te, W. Ionic conductivities were not reported, but research continued on garnets and Murugan et al [58] was the first to prepare the well-researched garnet $Li_7La_5Zr_3O_{12}$ (LLZO). This garnet structure has a high ionic conductivity ~10^{-4} S cm^{-1}, and good stability in contact with electrode materials including lithium. Later it was discovered that LLZO has two phases,a cubic and tetragonal phase, and that only the cubic phase acts as a fast ionic conductor, this cubic phase contained small amounts of aluminium from the crucible and led researchers to focus on stabilizing this conducting phase with various other dopants. [59] Garnet type structures are easily doped and substituted to vary the cations and lattice parameters, including dual substitution where one dopant acts to stabilize the cubic conducting phase and another to increase the lithium content within the structure such as $Li_{6.65}Ga_{0.15}La_3Zr_{1.90}Sc_{0.1}O_{12,}$ which has a reported conductivity of 1.8 x 10^{-3} S cm^{-1} at 27 ^oC. [60] Garnets are promising candidates for solid-state batteries due to their high ionic conductivities, however LLZO-type materials are not stable in moisture and CO_2 found in the ambient atmosphere, making them difficult to handle outside of a sealed environment and hence commercially unfavourable for large scale synthesis. [61]

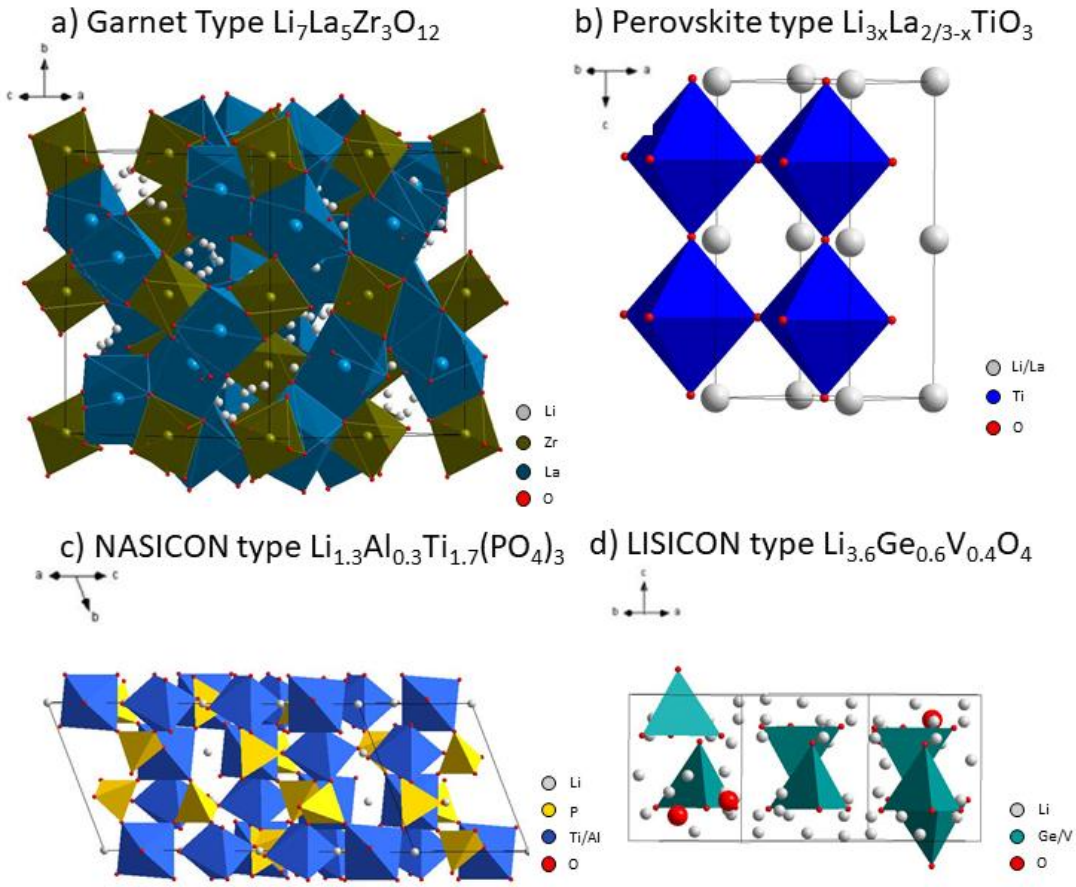

Figure 1.3: Image showing the crystal structure of the fast ionic conductors discussed in this section where a) is the garnet type $Li_7La_5Zr_3O_{12}$, [62] b) is the Perovskite type $Li_{3x}La_{2/3-x}TiO_3$, [63] c) is the NASICON type $Li_{1.3}Al_{0.3}Ti_{1.7}(PO_4)_3$, [64] and d) is the LISICON type $Li_{3.5}Ge_{0.5}V_{0.5}O_4$. [65] Crystallographic information was obtained from the references provided and all images were created using the DIAMOND software.

The structures discussed in this section all contain the necessary features to allow fast ionic conduction; they possess a framework structure and mobile sub-lattice which allows lithium movement (**Figure 1.3**). The highest conductivities reported are for structures which have been doped and the interstitials or vacancies present in these lattices allow fast ionic conduction to occur at room temperature which is not feasible for ideal crystals. Although there are other types of fast ionic conductors, those discussed in this section are promising because of their overall performance, ionic

conductivity, chemical and thermal stability. **Table 1.1** gives an example of each structure discussed along with their ionic conductivity, garnet type structures show the best ionic conductivity overall and are also stable in contact with lithium. All of these structures require further research for their use in all-solid-state batteries as they still have respective limitations which have been considered in this section.

Table 1.1: A summary of the conductivities for the structures discussed in this section.

Structure type	**Example**	**Total Ionic conductivity (S cm^{-1})**
LISICON	$Li_{3.6}Ge_{0.6}V_{0.6}O_4$ [46]	4 $x10^{-5}$ (18 ^oC)
NASICON	$Li_{1.3}Al_{0.3}Ti_{1.7}(PO_4)_3$ [50]	7.8 $x10^{-5}$ (RT)
Perovskite	$Li_{3/8}Sr_{7/16}Ta_{3/4}Zr_{1/4}O_3$ [53]	2.7 $x10^{-4}$ (27 ^oC)
Garnet	$Li_{6.65}Ga_{0.15}La_3Zr_{1.90}Sc_{0.1}O_{12}$ [60]	1.8 $x10^{-3}$ (27 ^oC)

1.3.2 Cathode structures

Structures considered for use as a cathode material in batteries are similar to those proposed above for electrolytes, however, the structure must contain a reducible element and allow electrons and ions to move within the structure, have a high capacity (energy stored per unit weight) and have high lithium reversibility upon insertion and extraction. [66] The cathode structure must also be stable in contact with the electrolyte to minimise degradation and interfacial resistance. [67] The structures used in lithium ion batteries as cathode materials are typically transition metal oxides which contain a transition metal capable of varying oxidation states, the first reported being $LiCoO_2$ (LCO) which is considered a layered transition metal oxide cathode material. [68] Since this breakthrough, research has focussed on improving the active elements within the cathode structure in order to increase the overall capacity of the cell, hence research into cathode structures is ongoing. Furthermore, the development of new battery technologies and solid electrolytes will in turn require the improvement of cathode materials to satisfy the demand in energy storage. The most common types of cathode structures include layered transition metal oxides, spinels and olivine type

structures. These structures show promise due to their high capacities, stability and rate capabilities required to perform as a cathode in a cell. [69]

Layered transition metal cathodes with the formula Li_xMO_2 [where *M*= Co, Ni, Mn], are attractive due to their high theoretical capacity. [68 ,70, 71] $LiNiO_2$ has a reported capacity of 260 mA h g^{-1},[70] however it faced capacity loss with further cycles. Due to its low cost and more abundant transition metal element, $LiMnO_2$ was considered the most environmentally friendly with a theoretical capacity of ~280 mA h g^{-1}, however the cathode undergoes many structural changes and experiences capacity fade over repeated cycles. [72] To mitigate these shortfalls $Li(Ni_xCo_{1-2x}Mn_x)O_2$ layered materials, commonly referred to as NMC, were synthesised and are widely researched. [73, 74, 75] NMC aims to accommodate the advantages of each transition metal; increased capacity of Ni, high stability of Co and the abundance of Mn, while maintaining a high capacity and good cycle life.[76] Although NMC is commercially used as a cathode in Li-ion batteries, such as NMC-811 which produces a capacity of ~ 200 mA g^{-1}, research continues in this field to maximise the materials potential for application in EV's and minimise degradation. [77]

Olivine structures have been shown great research interest due to $LiFePO_4$ (LFP) first reported by Goodenough,[78] which has been commercially used as a cathode in Li-ion batteries due to the environmentally friendly nature of Fe and low material cost. However, the theoretical capacity of LFP, 170 m A h g^{-1}, is lower than that of the above layered transition metal oxides. [79] The olivine structure $LiMPO_4$ [Where *M*= Fe, Mn, Co, Ni], [78, 80, 81, 82] is considered a safer alternative to some layered transition metal oxide cathodes due to the strength of *M*-P-O bonds, unfortunately an additional cost is inferred due to the low electronic conductivity of the material, hence particles often require carbon coating. [83] In a similar manner to that of NMC materials, research has moved to dope olivine structures and change the morphology to increase the electronic conductivity of the material, without the need for carbon coating. [84, 82, 85]

Spinel structures, LiM_2O_4 typically $LiMn_2O_4$, are becoming highly researched due to the low cost, low toxicity and high electrical potential of the material. [86] During lithium insertion and extraction the spinel structure undergoes structural changes, during which the spinel structure can be completely lost and a disordered rock salt phase is formed, often this leads to capacity loss. [87] To alleviate this capacity loss, spinel

structures can be doped with Fe,[88] Co [89] and Ni, [90] with Co doping leading to the most improved the capacity retention. [91] Spinels have a reported capacity of ~250 mA h g^{-1} during deep discharge [92] yet practical applications show they produce a lower capacity than both olivines and transition layered materials, where $LiNi_{0.45}Mn_{1.45}Cr_{0.1}O_4$ shows stable cycling abilities while only producing a reversible capacity of ~115 mA h g^{-1}. [90] The key area of research interest is maximising the capacity retention through doping of the spinel structure.

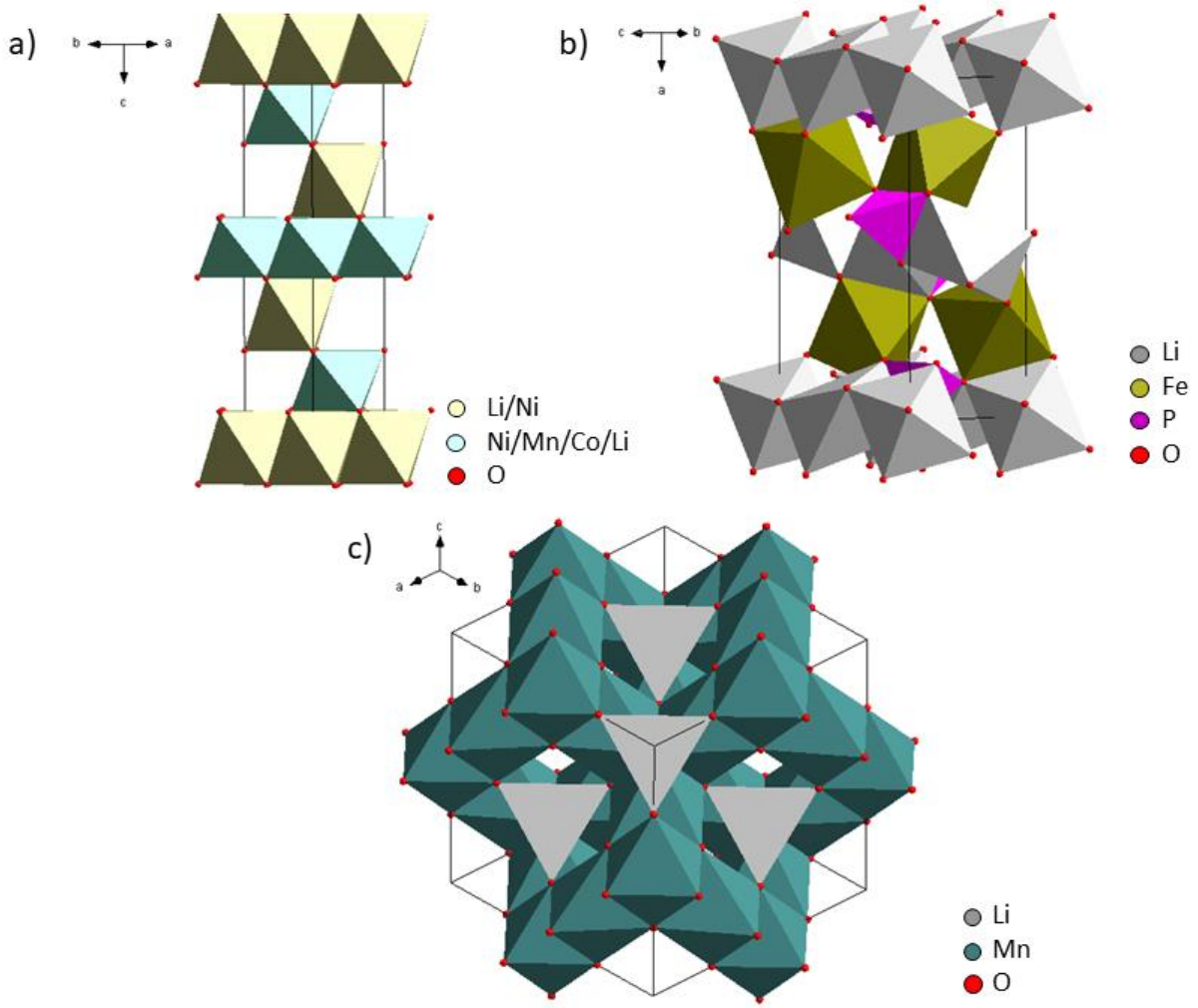

Figure 1.4: Image showing the cathode structures discussed in this section a) layered transition metal oxide NMC-811,[93] b) Olivine $LiFePO_4$,[94] c) Spinel $LiMn_2O_4$. [95] Crystallographic information was obtained from the references provided and all images were created using the DIAMOND software.

Table 1.2: Summary of the cathode structures discussed in this section, including structure type, example, reported capacity and the advantages and disadvantages associated with the structure.

Structure	**Example**	**Reported capacity/ mA h g^{-1}**	**Advantages/ Disadvantages**
Layered transition metal oxide	NMC- 811	200 [77]	High capacity and commercially used. Suffers from degradation issues
Olivine	$LiFePO_4$	170 [79]	Environmentally friendly low material cost. Low electronic conductivity.
Spinel	$LiNi_{0.45}Mn_{1.45}Cr_{0.1}O_4$	115 [90]	Low cost with good electronic properties. Structural changes during cycling causes capacity fade.

Table 1.2 provides a summary of the most common cathode structures (**Figure 1.4**) utilized in current batteries including the reported capacity as well as some of the advantages and disadvantages associated with the structures. As battery chemistries and battery technologies advance new cathode materials are needed to accommodate the type of batteries needed for the future. In the case of solid-state batteries, volumetric changes which accompany the insertion and extraction of lithium within a crystal lattice, particularly that of the cathode, has led to research aimed at lattice matching the electrolyte and cathode material. Interfacial resistance between the cathode and electrolyte has also prompted research into this area, hence synthesising and studying cathode materials with similar structures to that of solid state batteries is important to consider for generating commercially viable batteries for the future. [96, 97, 98]

1.4 Motivation, aims and thesis outline

It is evident that all-solid-state batteries offer one solution to the safety concerns posed by conventional Li-ion batteries, unfortunately, the limitations of commercially generating batteries with this technology still need mitigating. Key areas include: the ionic conductivity of the electrolyte, material stability (particularly in air), low-cost synthesis/manufacturing procedures as well as the interfacial resistances within a cell particularly that of the electrolyte/ cathode interface. These issues can potentially be mitigated through material choice, hence materials discovery and further research into the mitigation of these issues is required. Both the electrolyte and cathode material are in need of necessary research, particularly in relation to the application in solid state batteries, as other batteries technologies face different challenges.

Material discovery is a broad scientific concept which is utilised across all science and technology and involves the discovery of new materials and structures or the development of previous materials for use in a specific application. The choice of synthesis, characterisation and investigation of a materials microstructure play a crucial role in how this structure will be utilised commercially, it is therefore important to consider a materials application prior to research and fully understand the basic performance before a full technical product is developed. [99] Materials discovery based on synthesising and testing new materials is a timely and expensive step in the development of technology and this step is now moving towards the use computational modelling and artificial intelligence. [100, 101] However, experimental techniques to characterise promising materials and even reinvestigate materials for application in a different technology is still required.

Based on the literature reviewed, electrolyte structures benefit from small amounts of doping to increase the ionic conductivity or stabilise a particular polymorph, hence work on doping newly discovered families remains important in fully optimising a structures performance within a battery. Furthermore, investigating electrolyte structures which could contain a reducible transition metal element could yield structures capable of performing as a cathode, hence generating the possibility of materials which take advantage of lattice matching across the electrolyte/ electrode

interface, potentially decreasing the interfacial resistances within a cell. Full characterisation of structures is also important, as understanding a structure allows the materials properties to be better understood in a specific application. Often this can be generalised to a group of materials, for example, the sensitivity of garnet structures to moisture and CO_2. [61] This type of research can support accelerating the development of solid-state batteries for commercial use, hence, work contained in this thesis focusses on doping of electrolyte structures and reinvestigating materials for their application in batteries. Particular focus is paid to the structure of each material and how this varies the electrochemical properties of the material studied.

Chapter 2 provides background on the major experimental techniques used in this thesis including diffraction and electrochemical characterisation techniques, as well as an overview of solid state nuclear magnetic resonance (SSNMR) and x-ray absorption spectroscopy (XAS). Chapter 3, the first research chapter, provides information on $LiTa_2PO_8$, a new solid electrolyte structure and the impact of dopants on the ionic conductivity of the material. This is followed by chapter 4 which looks at the Li-ion transport properties of $Li_3Fe(MoO_4)_3$, a cathode material, and how this is related to its structure. Chapter 5 focusses on the structural changes which occur to $Li_3Fe(MoO_4)_3$ during cycling and aims to clarify some aspects of the literature already published on this structure and isostructural materials. Chapter 6 is a summary of the future work possible after this thesis and contains information on the next steps available for the materials covered in this work as well as the wider research aspect of modifying structures with reducible transition metal elements in to order to reduce the interfacial resistance with a cell.

CHAPTER 2: EXPERIMENTAL METHODS

2.1: Diffraction Techniques

When waves of the same magnitude interfere with a spacing or object, the incident waves interfere with each other, where constructive interference leads to an increase in intensity and destructive interference leads to a decrease in intensity, causing a diffraction pattern at a detector. As a crystal lattice contains atoms which are spaced with a similar magnitude to that of the wavelength of an x-ray, a diffraction pattern can

be produced. This can yield valuable information regarding the structure of a crystal. A crystal can be described as consisting of a regular repeating 3-dimensional group of atoms known as a unit cell. Typically, a unit cell is formed of the smallest possible repeating unit that also encompasses the full symmetry of the structure. The 2D image shown in **Figure 2.1** shows the unit cell of NaCl, presenting the full 3D symmetry of the crystal lattice (where each face of the cubic structure is **Figure 2.1**). Crystals belong to one of seven 3D crystal systems that can be differentiated by their unit cell geometry and symmetry elements and these are listed in **Table 2.1**.

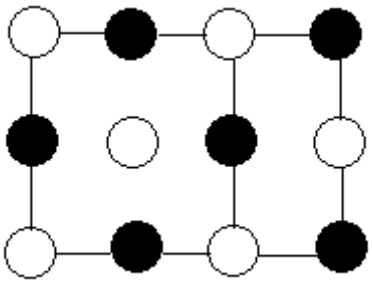

Figure 2.1: Image showing the unit cell of NaCl which best represents the 3D symmetry of the structure. Na is black, Cl white.

Table 2.3: Table showing the seven crystal systems, including shape, symmetry and allowed lattices. [102]

Crystal system	Unit cell shape	Essential symmetry	Allowed lattice
Cubic	a=b=c, $\alpha = \beta = \gamma = 90$	Four threefold axes	P, I, F
Tetragonal	a=b≠c, $\alpha = \beta = \gamma = 90$	Three fourfold axes	P, I
Orthorhombic	a≠b≠c, $\alpha = \beta = \gamma = 90$	Three twofold axes or a mirror plane	P, F, I, C
Hexagonal	a=b≠c, $\alpha = \beta = 90, \gamma = 120$	One sixfold axes	P
Trigonal	a=b≠c, $\alpha = \beta = 90, \gamma = 120$	One threefold axes	P,

Monoclinic	a≠b≠c, $\alpha = \gamma = 90, \beta \neq 90$	One twofold axes or a mirror plane	P, C
Triclinic	a≠b≠c, $\alpha \neq \beta \neq \gamma \neq 90$	None	P

Braggs law can be used to describe the interaction of waves with a crystal lattice. Due to the lattice symmetry shown in **Table 2.1**, only certain Bragg angles are allowed. Braggs law can be derived using **Figure 2.2**.

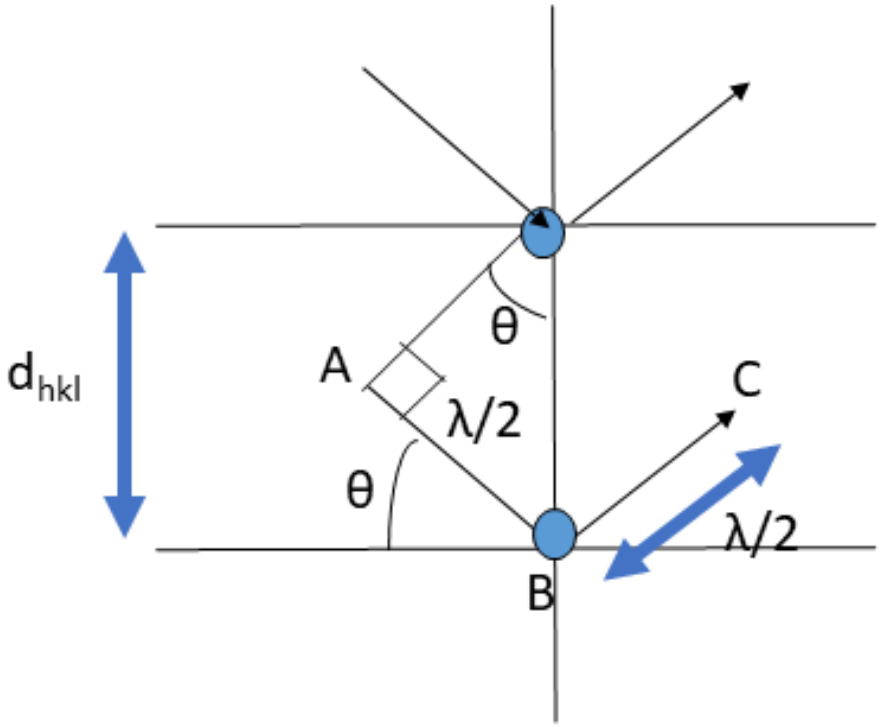

Figure 2.2: Image showing two crystal planes 1 d-spacing apart used for Braggs law derivation.

An incident wave approaches and atom at angle (θ) and is diffracted perpendicular to the atom. In order for the wave to interfere constructively with another wave it must travel an extra distance σ which is equal to an integer number (n) of wavelengths. Consider the distance between the three points ABC as one wavelength (λ), and the distance AB to be equal to dsin(θ). Then the extra distance travelled by the wave to interfere constructively to give a diffraction peak is as follows.

$$\sigma = n\lambda \quad \textbf{(2.1)}$$

And

$$ABC = \lambda = 2\mathrm{AB} \quad \textbf{(2.2)}$$

Combining (**2.1**) and (**2.2**) gives the path length (**2.3**) to be:

$$\sigma = \mathrm{n} \times 2\mathrm{AB} = 2\mathrm{dsin}(\theta) \equiv n\lambda \quad \textbf{(2.3)}$$

Braggs law is typically written as nλ= 2dsin(θ) and can be used to calculate the d-spacing between lattice planes. Both x-rays and neutrons can be diffracted by a crystal lattice and can provide useful information regarding the arrangement of atoms in a crystal.

2.1.1: X-ray diffraction

X-ray diffraction utilises the theory of Braggs law to experimentally calculate the arrangement of atoms in a crystal. There are two observed experimental patterns in X-ray diffraction i) single crystal and ii) powder diffraction. Single crystal x-ray diffraction uses a high-quality single crystal placed in different orientation within the x-ray beam resulting in a diffraction pattern resembling **Figure 2.3**. The position of the spots provides information of the crystal lattice symmetry and d-spacing's while the intensities and shape can be analysed to determine atomic position, crystallite size and microscopic strain. Single crystal diffraction provides the most information regarding a crystal structure however growing high quality crystals can be difficult. i. Powder diffraction involves many crystals of different shapes and sizes, the diffraction pattern is generated from the interaction of an x-ray spot on a section of a powder and is often represented as a line plot, The information provided summates the structure of the crystal and the morphology of the powder, for example, crystallite size and shape. Powder diffraction is used for phase identification and obtaining structural information of powdered substances and can be used to identify unknown structures.

Figure 2.3: Fourier transform of a TEM image to produce a diffraction pattern of a powdered $Li_{1.6}Mn_{2.2}(MoO_4)_3$ sample. TEM performed in Sheffield by Dr Laura Wheatcroft.

Powder x-ray diffractometers consist of 3 basic components: an x-ray source, a sample holder and a detector. The x-rays are generated from a cathode ray tube which produces electrons to bombard a target source (Cu, Mo, Fe), this produces k_α and k_β. Radiation. As k_α radiation is the most intense this interacts with the crystal structure generating $k_{\alpha1}$ and $k_{\alpha2}$ peaks, both of which are characteristic of the target material used to generate them. A monochromator is then used to collimate the two before being directed at the sample. The sample holder rotates across a 2θ angle range and the detector gathers the resulting x-rays. [103]

Laboratory based x-ray diffractometers, used within this work, are typically set up in reflection mode with the Bragg-Brentano geometry shown in **Figure 2.4**, where the angle between the incident beam and diffracted beam is 2θ. The only requirement for diffraction to occur is that the lattice planes occur at the Bragg angle θ to the incident beam. Powder diffraction heavily relies on sample preparation as, unlike single crystal diffraction, multiple particles and hence unit cells are contained within the powder in a random orientation. It is therefore paramount to prepare the sample to allow for the assumption, in an ideal specimen, that there are an infinite number of particles in an infinite number of orientations.

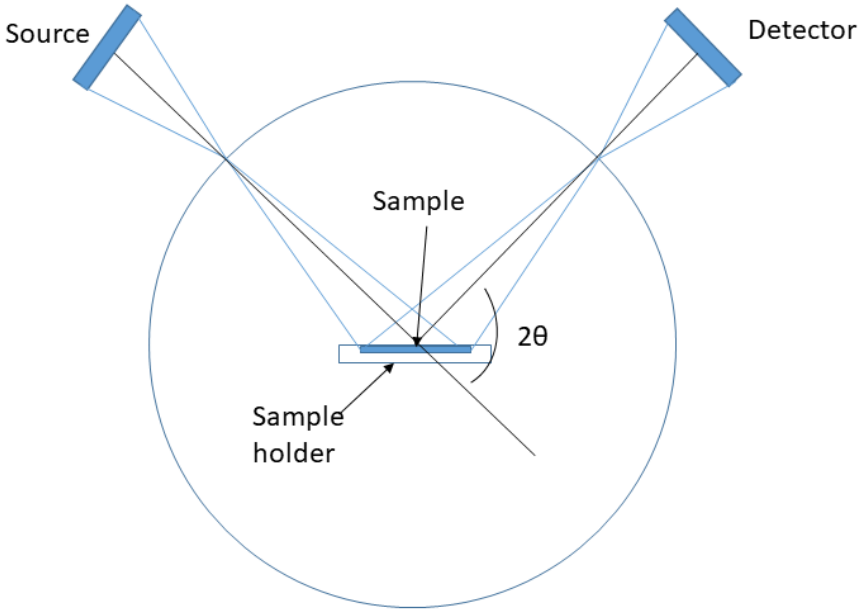

Figure 2.4: Typical Bragg-Brentano geometry laboratory x-ray diffractometer set-up**.**

The experiment then uses Braggs law to produce a plot of intensity vs 2θ. Here λ remains constant, θ is changed and the d-spacing is measured. The diffraction pattern on the intensity vs 2θ plot can then be indexed to a space group by a) matching the observed pattern to a database or b) using the calculated d-spacing's and miller indices to find the unit cell of a crystal. As an example, for a cubic system:

$$\frac{1}{d^2} = \frac{h^2+k^2+l^2}{a^2} \qquad \textbf{(2.4)}$$

The unit cell parameter can be calculated from the d-spacing of a h k l plane such as the 1 0 0 plane. Each crystal system has a symmetry allowed equation for relating the d-spacing's to the unit cell of the crystal.

The peak intensities (I_{hkl}) in a diffraction pattern can provide more information on the structure of material and is related to the collective scattering power of the atoms, structure factor (F_{hkl}), as so $I_{hkl} \propto |F_{hkl}|^2$. The intensity of the peak can also be affected by factors such as absorption, site occupancies, thermal vibrations and even experimental setup. The structure factor relies on the scattering factor of an atom (f), in x-ray diffraction the wave is diffracted by the electron density around an atom hence greater peak intensities are observed for heavier elements. The atomic form factor

decreases with increasing θ, shown in **Figure 2.5** hence the peak intensities decrease with increasing θ also.

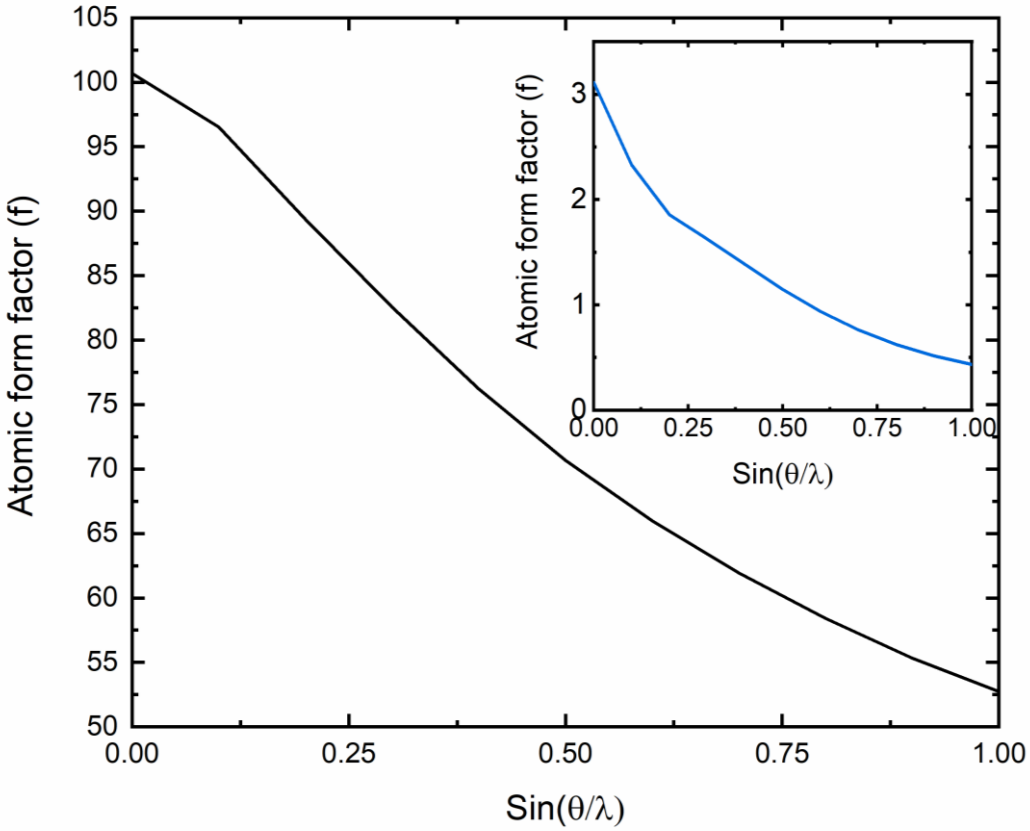

Figure 2.5: Atomic form factor for tantalum with the inset showing the atomic form factor for lithium.

Using both the position and intensity of each peak, x-ray diffraction can provide a complex image of a material and provides information on the unit cell, the atoms within the cell, the thermal parameters of the atoms, crystallite size and shape, electronic configuration of the atoms and site occupancies. For unknown materials powder XRD is a crucial tool used to understand the structure of a material which can provide insight into the physical properties of the material.

2.1.2: Neutron diffraction

One downside to x-ray diffraction is the technique's difficulty in providing information regarding light elements, such as lithium, due to the scattering ability of the electron density and hence atomic form factor. Neutron diffraction is a complementary technique which uses neutrons in place of x-rays. According to the De Broglie relationship, ($\lambda=h/mv$), moving neutrons have a wavelength and so also produce a diffraction pattern. Unlike x-rays, neutrons interact with the nucleus of the atom and the scattering intensity is related to an atoms coherent scattering length, as shown in **Figure 2.6**, this allows elements such as Li to be distinguished from heavier elements.

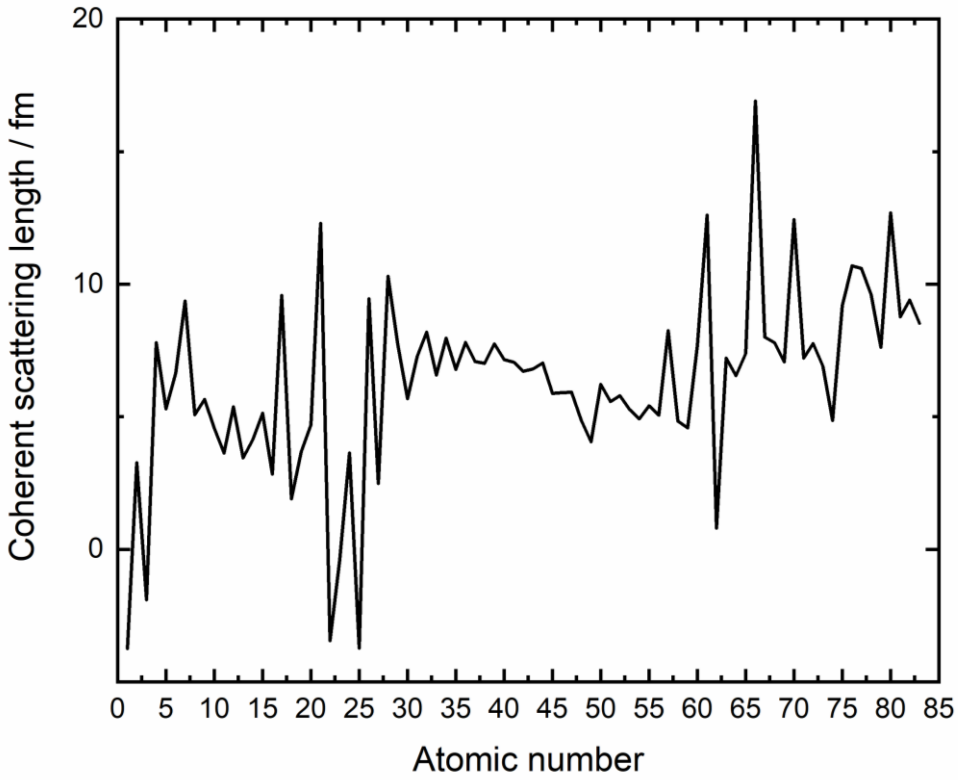

Figure 2.6: Neutron diffraction coherent scattering length change vs atomic number.

The experimental setup used in this thesis for neutron diffraction (**Figure 2.7**) is a time of flight (TOF) diffractometer. This setup utilises Braggs law but keeps the angle of diffraction, θ constant with the wavelength, λ, variable. The wavelength of each neutron is calculated based on its TOF from the source to the detectors, commonly referred to as path length l. The de Broglie relationship can be rewritten as:

$$\lambda = \frac{h}{mv} = \frac{ht}{ml} \qquad \textbf{(2.5)}$$

Combining with equation (**2.3**) and rearranging for d-spacing, Braggs law can be rewritten as:

$$d = \frac{ht}{2ml \sin\theta} \qquad \textbf{(2.6)}$$

Where t is time, l is the path length of the neutron, h is Planks constant and m is the mass of a neutron. As θ remains constant neutron diffractometers, such as the one shown in **Figure 2.7**, have multiple detectors surrounding the sample.

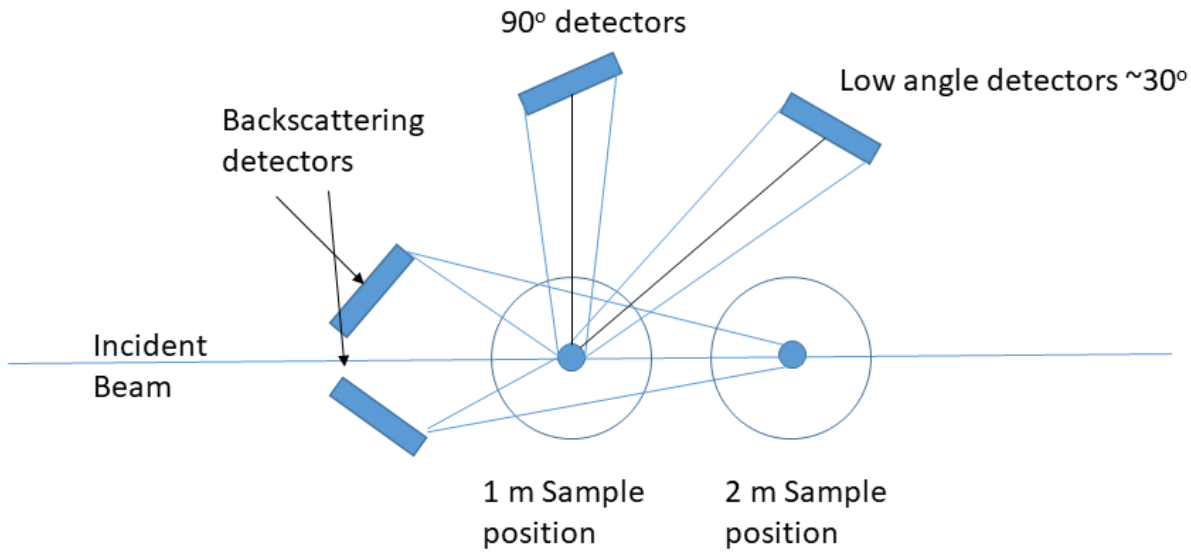

Figure 2.7: Neutron diffraction setup based on the high resolution powder diffractometer (HRPD) at ISIS. [104]

Neutron diffraction is typically performed at central facilities due to the high energy required to generate neutrons and so is often not performed unless required due to the time and expense of the experiment. Neutron diffraction is vital, when the scattering density of an atom is small, to identify the position and distribution of light elements, such as lithium. This is significant when the position of these elements is needed to fully understand the properties of the material, such as battery materials where the distribution of lithium is key in understanding the diffusion mechanism within the structure.

2.1.3 Rietveld refinement

Rietveld refinement is a method used to analyse diffraction data and is used to calculate a diffraction pattern from an input model it then uses a least squares procedure to make small adjustments to the calculated model in order to best fit the observed data.[105] A Rietveld refinement can now be performed on computer packages such as GSAS [106, 107] in order to obtain structural information of a crystal. The agreement parameters include the weighted regression coefficient R_{wp} and difference in observed and expected outcome (GOF) X^2 which are defined as follows: [108]

$$R_{wp} = \left\{ \frac{\sum w_i (y_i^{obs} - y_i^{calc})^2}{\sum w_i \, (y_i^{obs})^2} \right\}^{\frac{1}{2}} \quad \textbf{(2.7)}$$

$$\chi^2 = \frac{R_{wp}}{R_{exp}} \quad \textbf{(2.8)}$$

Where,

- $R_{exp} = \left\{ \frac{(N-P)}{\sum w_I \, (y_i^{obs})^2} \right\}^{\frac{1}{2}}$
- $w_i = \frac{1}{y_i^{obs}}$
- y_i^{obs}- observed peak intensity at the ith step
- y_i^{call}- calculated peak intensity at the ith step
- N – number of points
- P- number of parameters

Statistically, each refinement should try to minimize R_{wp} and achieve a X^2 of 1, while maintaining physical meaning of the refinement parameters used. A full list of parameters and how this relates to a physical property is listed in the GSAS manual.[106] A Rietveld refinement should yield full structural information regarding a sample including: lattice parameters, site occupancies, thermal atomic displacement parameters and phase fractions (if multiple phases are present in a sample). This allows an image to be generated of the crystal structure which can provide useful information regarding the materials properties. A Rietveld refinement can be performed against neutron and x-ray powder diffraction data where fitting parameters can be customised as per the GSAS manual. [106, 107]

2.2: Electrochemical techniques

In order to understand a battery material electrochemical techniques must be used to assess the performance of a material or an electrochemical cell.[109] The parameters used within electrochemical testing typically involve changing and measuring either voltage) or current (i), which are related as per Ohms Law:

$$\mathrm{E} = \mathrm{iR} \quad \textbf{(2.9)}$$

Where,

- R= resistance

In basic electrochemistry voltage is defined as the work needed per unit of charge to move 1 electron between two points and can be calculated using the Gibbs free energy change between reactants and products (ΔG_r). Such that:

$$\mathrm{E} = \frac{-\Delta \mathrm{G_R}}{\mathrm{nF}} \quad \textbf{(2.10)}$$

Where,

- n=number of electrons exchanged
- F= Faraday constant.

Current (i) is defined as the rate of flow of charge (q) and can be defined as:

$$i = \frac{dq}{dt} \quad \textbf{(2.11)}$$

The electrical resistance of a material ® can be defined as the obstruction of current, and is related to a materials resistivity (ρ) as shown:

$$R = \frac{\rho L}{A} \quad \textbf{(2.12)}$$

Where,

- L= Path length of the resistor
- A= Cross-sectional area of the resistor

The above parameters can be used in electrochemical experiments to provide information regarding a batteries performance as well as a materials ability to be used within a battery. The three most common techniques include: Cyclic voltammetry

(CV), galvanostatic charge-discharge and electrochemical impedance spectroscopy (EIS). DC polarisation can also be used as a supplementary technique to EIS and can be used to determine the electronic conductivity of a material.

2.2.1: Cyclic voltammetry

Cyclic voltammetry (CV) is a potential technique where the current is measured over a defined potential range, and can give information regarding the redox reactions present in a battery. The experimental set up involves a voltage scan (0.1- 10 mV s^{-1}) between two voltages, E_1 and E_2 (or electrochemical window) and measuring the produced current, this generates a voltagram (**Figure 2.8**). Typically, two peaks are produced one cathodic (E_{pc}) and anodic (E_{pa}), each correspond to reduction and oxidation reactions respectively occurring at that voltage.

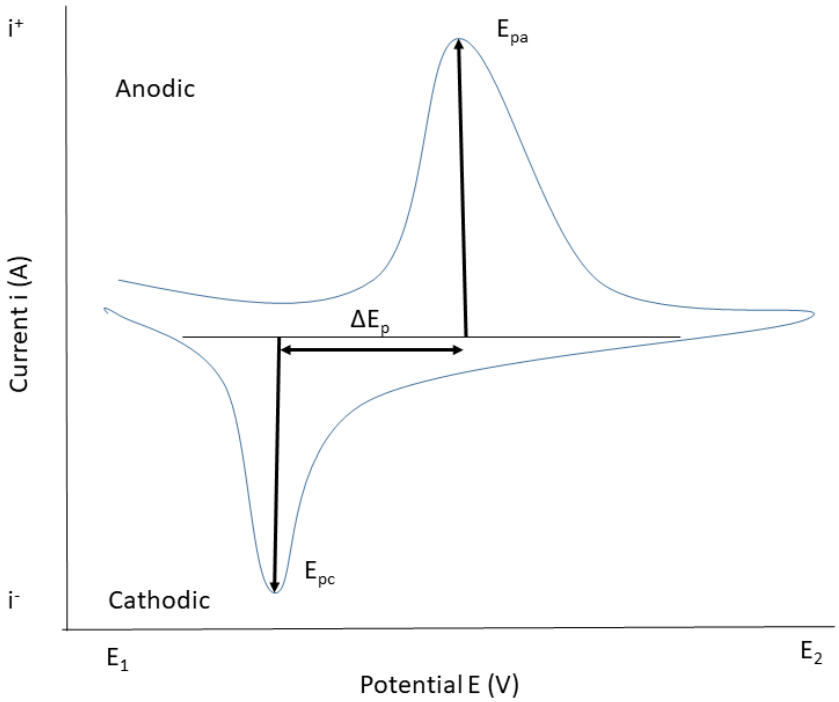

Figure 2.8: Example cyclic voltagram between two potentials E1 and E2.

The Nernst equation (**equation 2.13**) can be used to describe the equilibrium in a half-cell reaction and relates the potential of the cell to the concentration of the oxidized and reduced ions. The potential at which the reduction and oxidation peaks occur can

be related to a half cell reaction of a species.[110] ΔE_p gives an indication of the diffusion rates of the redox species and the ratio of anodic to cathodic peak currents allows the reversibility of the reaction to be understood, where the ratio is equal to 1 the reaction can be deemed reversible.

$$E = E^o + \frac{RT}{nF}\ln[\frac{[ox]}{[red]}] \quad \textbf{(2.13)}$$

Cyclic voltammetry is a useful technique for identifying redox couples in a battery and whether the redox processes are reversible. This technique can yield powerful information on a materials ability to be used within a battery.

2.2.2: Galvanostatic charge-discharge

Galvanostatic charge-discharge experiments are considered the opposite of cyclic voltammetry, and are performed under a constant current within a voltage window (E1-E2) with the potential being measured. Typically, charge-discharge curves are represented as potential Vs capacity (the amount of charge in a material per unit weight), and yields information regarding a materials performance as a cathode. The experiment requires the theoretical capacity (Q) of the material to be used to calculate the applied current, Q is related to the molecular weight of the material used (M_w), shown in **equation 2.14** and has units of mA g^{-1}.

$$Q = \frac{nF}{M_w} \quad \textbf{(2.14)}$$

Where n is the number of charge carriers and F is the Faraday constant. A C-rate, the amount of time required to fully discharge a battery, can then be used to determine the applied current. This results in a graph similar to that shown in **Figure 2.9**, where plateaus often represent redox reactions. The data obtained from a galvanostatic charge-discharge experiment can be analysed as a differential capacity (dQ/dV) plot and compared with CV data, the dQ/dV plot represents plateaus as peaks and the voltage at which this occurs can be easily distinguished. dQ/dV plots indicate the voltage at which the cell is losing/gaining capacity and this is often associated with redox couples. Combining the analysis of CV with dQ/dV data, a greater understanding can be reached on the electrochemical reactions occurring within a cell.[111]

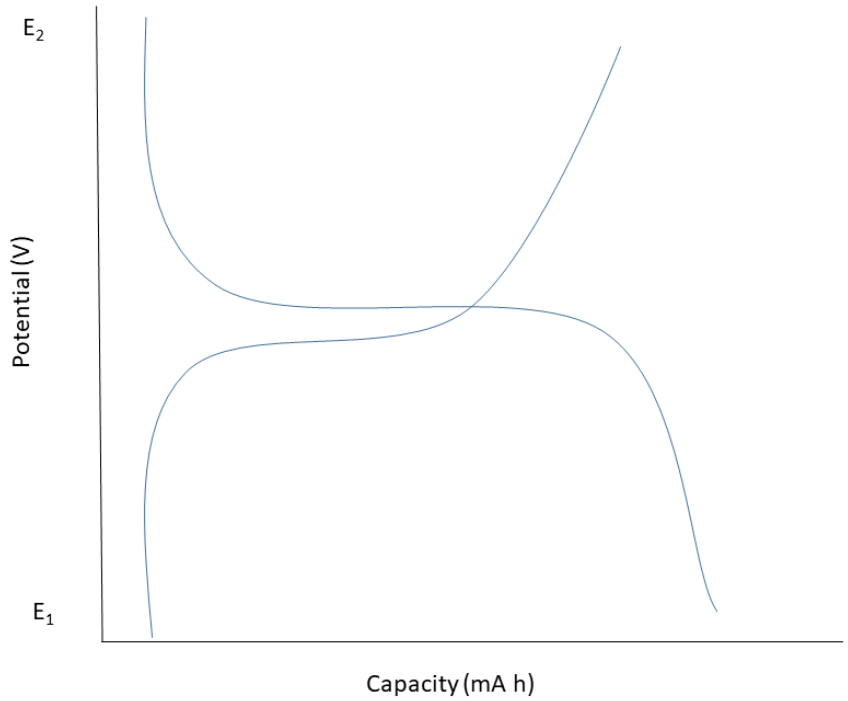

Figure 2.9: Example of a typical galvanostatic charge-discharge curve.

Galvanostatic cycling yields important information regarding a cells performance including the cycle life, efficiency and capacity; particularly when a cell is cycled over a long period of time and using different C-rates. [109]

2.2.3: Electrochemical impedance spectroscopy

Electrochemical impedance spectroscopy (EIS) is the experimental technique used to measure the conductivity of a material. The experimental procedure involves applying a voltage perturbation across a cell and measuring the current response over a defined frequency range. Impedance (Z) is classed as the resistance of current in a circuit, if the circuit only includes a resistor, then Z=R, however there are multiple circuit elements available which will change the current output. When a sinusoidal voltage is applied a sinusoidal current response is produced with a phase difference (θ), both the amplitude and phase of the input and output signals require representation and this is accomplished using complex exponentials. At a given time (t) the Voltage and current can be found in relation to the angular frequency ω and phase difference θ.

$$E_t = E_o \sin(\omega t) \quad \textbf{(2.15)}$$

$$i_t = i_o \sin(\omega t + \theta) \quad \textbf{(2.16)}$$

Equations 2.15 and **2.16** can be rewritten in complex exponentials as:

$$E_t = E_o e^{j\omega t} \quad \textbf{(2.17)}$$

$$i_t = i_o e^{j\omega t} e^{j\theta} \quad \textbf{(2.18)}$$

Using Ohms law (**equation 2.9)** Z is:

$$Z_t = \frac{E_o}{i_o} e^{-j\theta} \quad \textbf{(2.19)}$$

Therefore, impedance is represented on a complex plane (**Figure 2.10**).

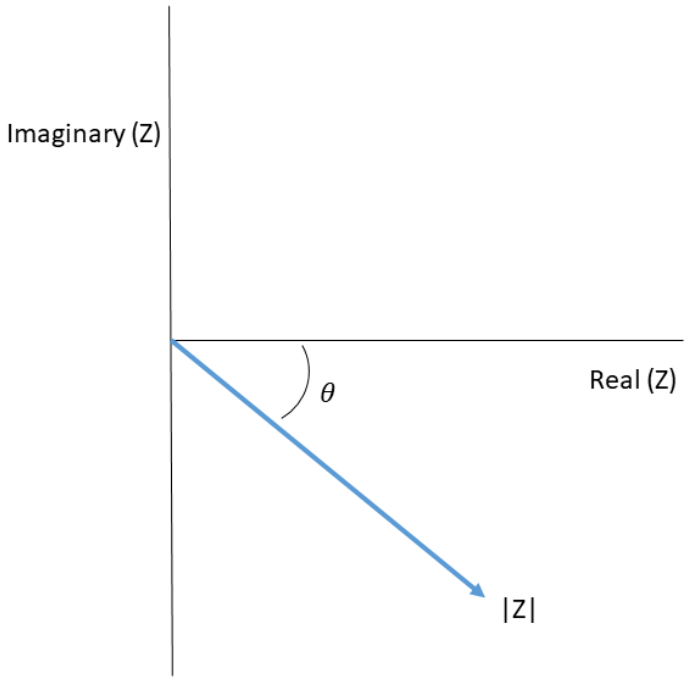

Figure 2.10: Example complex plane representation of impedance at a given frequency.

EIS is performed over a frequency range, at each frequency an impedance response will have a real and imaginary component, these are typically plotted as a Nyquist plots shown in **Figure 2.10.** A resistor and capacitor in parallel produces a semi-circle, where a capacitor will respond to the voltage perturbation as shown in **Equation 2.20**.

$$i_t = C\frac{dV_t}{dt} \quad \textbf{(2.20)}$$

And for parallel circuit elements:

$$\frac{1}{Z} = \frac{1}{Z1} + \frac{1}{Z2} \quad \textbf{(2.21)}$$

$$Z1 = R \quad \textbf{(2.22)}$$

$$Z2 = \frac{-j}{\omega C} \quad \textbf{(2.23)}$$

Therefore, the total impedance is,

$$Z = \frac{R}{1+jR\omega C} \quad \textbf{(2.24)}$$

This can be separated into real and imaginary parts and results in a semicircle shown n **Figure 2.11**.

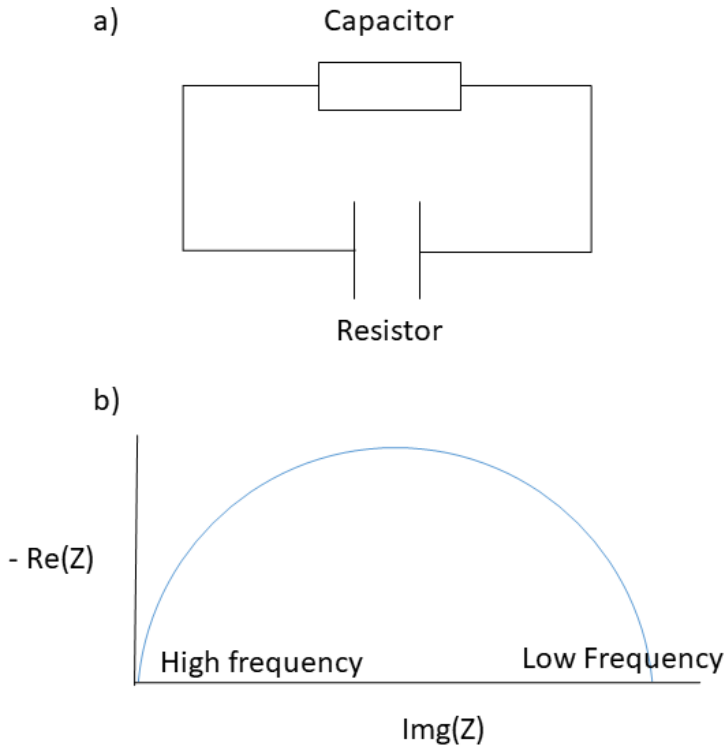

Figure 2.11: Example of a typical Impedance response produced by an RC circuit a) equivalent circuit used to fit the data b) Nyquist plot produced by the material.

Each circuit element will respond to the voltage perturbation differently and this yields a different impedance response. When real materials are investigated circuit elements

(equivalent circuits) shown in **Figure 2.11 a)** are used to model the impedance response observed and this allows an understanding of the physical properties of the material to be generated. In this work a constant phase element (CPE) is used to model the inhomogeneity of an electrode interface as a CPE is a circuit element used to describe non-ideal capacitance behaviour. The impedance response of a CPE can be described using **equation 2.25**:

$$Z_{CPE} = \frac{1}{C(j\omega)^n} \quad \textbf{(2.25)}$$

Where n is a dimensionless parameter between 0 and 1, when n=1 the impedance is described as a pure capacitor. The Nyquist representation of a CPE (**equation 2.25**) is a straight line at an angle of 90 x n or when used in series with a resistor, a depressed semi-circle depending on the value of n. Therefore, a CPE can be used to describe the low frequency spike observed in solid-electrolyte structure characteristic of the Li^+ ions reaching the blocking electrode as well as an inhomogeneous interface formed at an electrode which results in a depressed semi-circle in the Nyquist plot.[112]

It is important to consider the physical properties and behaviour of a material when assigning circuit elements during the fitting procedure so that the extraction of information, such as the ionic conductivity, is relatable to the material studied. In the case of solid electrolyte structures the resistance, extracted from the fitted equivalent circuit can be used to calculate the conductivity via **equation 2.12** to calculate the resistivity of the material; the inverse of which is the conductivity.

2.2.4 DC polarisation

DC polarisation is a technique first developed by Hebb-Wagner and is a technique that can be used to calculate the electronic conductivity of a solid oxide structure. [113] Polarisation techniques typically involve changing the potential of the system and measuring the resultant current. Tubandt's method allows for the transference number of ionic solids to be measured using Faradays Law of electrolysis, where the amount of substance deposited at an electrode is proportional to the electrical energy transferred and be written as **equation 2.26**.[114]

$$m = \frac{q}{zF} \quad \textbf{(2.26)}$$

Where m is the amount of substance deposited, q is the charge transferred, z is the no.1 of electrons and F is the Faraday constant. When a voltage is applied across a substance the ions will move to deposit on the respective electrodes increasing the mass of each electrode. This change of mass within the electrodes as well as the amount of charge transferred leads the way to calculate the transport number or a material and hence a way to measure the electronic and ionic conductivity contribution of a material. The transference number [t_{ion} and t_e] gives a way of measuring the extent of the ionic and electronic conductivity. If the total conductivity of a material can be classed as the summation of the ionic conductivity and electronic conductivity [$\sigma_T = \sigma_e + \sigma_{ion}$], the transference number can be writing as:

$$t_{ion} = \frac{\sigma_{ion}}{\sigma_T} = \frac{I_{ion}}{I_T} \quad \textbf{(2.27)}$$

$$t_e = \frac{\sigma_e}{\sigma_T} = \frac{I_e}{I_T} \quad \textbf{(2.28)}$$

Where I_{ion}, I_e and I_T represents the ionic current, electronic current and total current associated with the application of a potential across a substance. Combining **equations 2.27 and 2.28** yields **equation 2.29** for the lithium transference number of solid electrolyte.

$$t_+ = \frac{I_e}{I_T} \quad \textbf{(2.29)}$$

Experimentally, a potential is applied across a substance and the resultant current measured. If the substance is a pure ionic conductor ($t_+=1$) the current will approach 0 with time, however should the material be a mixed conductor the current will approach a non-zero value equal to the electronic current contribution (I_e). The ratio of the steady-state current (I_e) with respect to the initial current gives rise to the Li transference number of a material. The electronic current (I_e) can then be used to calculate the associated resistance and hence electronic conductivity of a material using **equations 2.9 and 2.12.**

2.3 Other experimental techniques

The experimental techniques described in this section have been performed outside of the university by collaborators. These techniques provide extra information regarding the structure and the Li^+ hopping mechanism of the materials researched in

this work. These techniques will be discussed for use exploring solid-state ionic conductor materials.

2.3.1 X-ray absorption spectroscopy

X-ray absorption spectroscopy, first reported experimentally in 1971, can be used, among other things, to determine the local structure of materials. [115] When an atom absorbs electromagnetic radiation of sufficient energy an electron can "jump" to a higher energy shell, referred to as an excited state, or be excited beyond the ionization energy, this energy is detected and recorded in XAS. This can be split into the X-ray absorption near edge structure (XANES) and extended X-ray absorption fine structure (EXAFS) (**Figure 2.12**). XANES typically provides information regarding the oxidation state of the atom, whereas EXAFS provides the local structural information, however, both provide complementary information regarding the local structure and electronic configuration of the absorbing atom. XAS can therefore provide crucial information regarding the oxidation state and coordination number of an atom, which can useful when combined with structural information obtained via diffraction techniques.

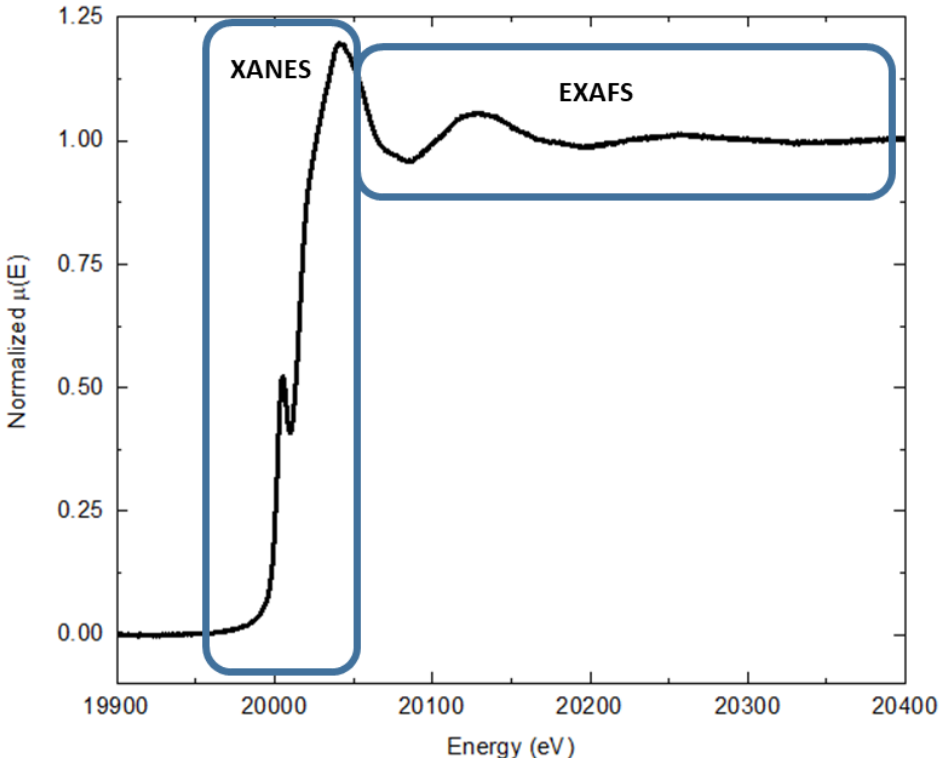

Figure 2.12**: XAS data collected via BAG experiment on Li_2MoO_4.**

2.3.2 Solid-state nuclear magnetic resonance

Solid-state nuclear magnetic resonance (SSNMR) is an atomic based technique which provides information regarding the local environments of atoms and can also indicate the dynamics of a material. For an atom to be considered magnetic it must contain non-zero spins, when atoms of this nature are placed within a magnetic field an energy difference (ΔE) is generated. This energy difference can be described using **equation 2.30**:

$$\Delta E = \frac{\gamma h}{2\pi}(1-\sigma)B_o \qquad \textbf{(2.30)}$$

Where γ is the gyromagnetic ratio fundamental of each isotope, h is planks constant, σ is the shielding surrounding a nucleus and B_o is the strength of the external magnetic field. This energy difference causes NMR transitions which are sensitive to the local electron environment surrounding the nucleus. NMR transitions are typically reported a chemical shift, δ / ppm which is the frequency ratio of the transition studied and a standard. An example static SSNMR spectrum is shown in **Figure 2.13** and typically gives a representation of the local environment of the magnetic atom under investigation.[116]

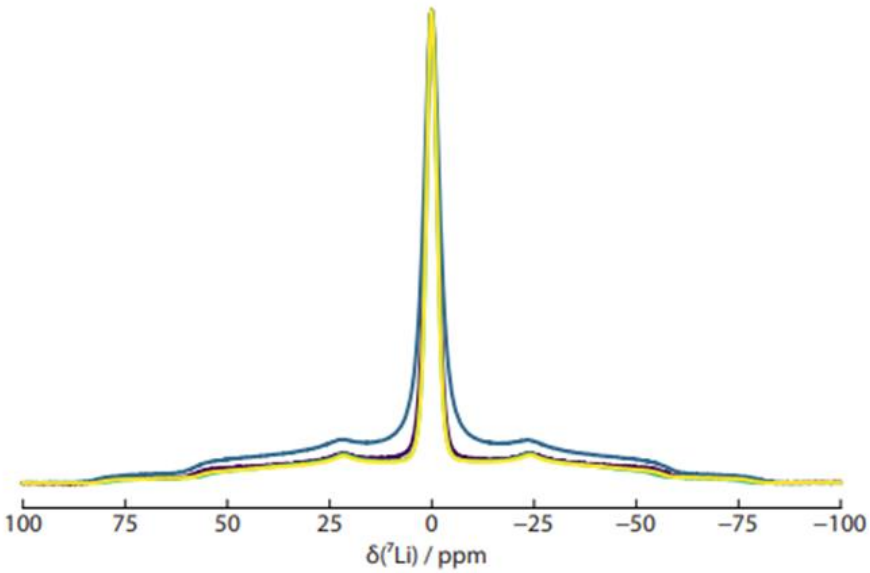

Figure 2.13: Example static NMR spectrum of $LiTa_2PO_8$ doped samples performed by S.Day at JM.

NMR relaxometry used within this thesis can provide information regarding the Li^+ movement within a solid-state **ionic conductor. First described in 1948 by Bloembergen et al,** [117] **the motion of magnetic atoms can be described using an exponential function $G_{(T)}$, which is a way to measure the temperature dependent relaxation of a magnetic atom. A Fourier transform of this function provides a spin-lattice relaxation rate (T_1^{-1}), assuming Arrhenius behaviour, this can be plotted on an inverse logarithmic scale Vs inverse temperature and used to estimate the activation energy of atomic hopping. SSNMR probing of activation energies typically gives a microscopic measure of the Li^+ diffusion occurring through a structure contrary to EIS which provides a macroscopic understanding of the material's diffusion mechanism. Therefore, when SSNMR is used in conjunction with EIS a better understanding of the structure-property relationship can be obtained.**

CHAPTER 3: DOPING OF $LITA_2PO_8$ FOR USE AS A SOLID ELECTROLYTE

3.1 Introduction

$LiTa_2PO_8$ was first synthesised by Kim et al [3] and is the first of a new family of solid electrolyte structures with a total ionic conductivity of 2.5×10^{-4} S cm^{-1}, comparable to that of well researched structures such a perovskites and garnets. [53, 118] Research has focussed on increasing the ionic conductivity of the material which has been theoretically reported to be as high as 35.3×10^{-3} S cm^{-1} for its intrinsic ionic conductivity.[119] Processing of this material has produced conductivities as high as 3.12×10^{-3} S cm^{-1} when hot pressed, however no other family members have been reported thus far. [120] Further research is needed to fully investigate the ionic conductivity of this material and to identify other family members with the potential of further increasing the conductivity of the parent phase

Doping of solid electrolytes is well documented in the literature of other solid electrolyte structures, such as garnets, in order to increase the conductivity of the material. [121]

When first reported, garnets produced an ionic conductivity of ~ 1 x 10^{-6} S cm^{-1} and through optimization of the structure a total ionic conductivity of ~1 x 10^{-3} S cm^{-1} can be achieved. [122, 123] Doping materials with small amounts of aliovalent transition metals changes the charge carrier concentration and can aid in increasing the ionic conductivity of a material, this has been reported on structures such as $Li_{7-x}La_3Zr_{2-x}Sb_xO_{12}$. [62] Al-doped LLZO is also well researched and known to have an increased conductivity as the Al dopant can stabilize the more conductive cubic polymorph of the structure.[59] Increasing a materials physical properties can also lead to an increase in conductivity as is the case for $Li_{1.3}Al_{0.3}Ti_{1.7}(PO_4)_3$, here a small amount of Al dopant leads to an increase in its sinterability and hence bulk conductivity of the material. [50] The addition of small amounts of dopants into a solid electrolyte structure tends to lead to an increased ionic conductivity via means of changing charge carrier concentration or physical properties of the material.

Although research has yielded a greater increase in conductivity of garnet materials, the structures still possess disadvantages when used in a battery. Namely, i) reactivity with air which can lead to a Li_2CO_3 layer on the surface of the electrolyte, ii) Li dendrite formation through the electrolyte leading to a decrease in overall conductivity and potential short circuiting, iii) poor interfacial contact with cathodes leading to an overall increase in ionic conductivity within the cell. [124] Using the knowledge acquired in garnet investigations and applying this to a new family of solid electrolyte structures, such as $LiTa_2PO_8$ which already has a high reported total ionic conductivity, can yield an improved solid electrolyte material which is stable in contact air, has improved interfacial contact and a decrease in potential dendrite formation.

This section will focus on doping the $LiTa_2PO_8$ structure with various cations to vary the charge carrier concentration and alter the structure of the material. As shown through well researched garnets, doping can offer the potential of increased ionic conductivity by increasing the charge carrier concentration i.e lithium stuffed garnets, or altering the structure of the cations within the unit cell i.e stabilization of the cubic polymorph. [125, 126, 127] Ultimately varying the unit cell of the structure could yield an increase in ionic conductivity of the solid electrolyte material.

3.2 Experimental

Solid state Synthesis: $LiTa_2PO_8$ was synthesised using the published solid state method.[3] Stoichiometric amounts of starting materials, Li_2CO_3, Ta_2O_5 and $(NH_4)_2HPO_4$ were ground in a pestle and mortar until homogeneous before being transferred to an aluminium crucible and heated for 8 hr at 600 ^oC. The powder is then reground pressed into a pellet and heated for a further 8 hr at 1000 ^oC. Samples containing Zr and Sb followed the same method with Sb_2O_5 and ZrO_2 used as the Sb and Zr source respectively.

Nb containing samples were synthesised at Johnson Matthey under the supervision of Mark Feaviour using the same starting materials for the Li, Ta and P source with the addition of Nb_2O_5 as the Nb source. Stoichiometric amounts of materials were weighed out and ground in a pestle and mortar with ~8 ml of ethanol as a grinding aid due to the larger volume of powder (~10 g). The powder was then heated to 600 ^oC for 8 hr then reground and heated to 1000 ^oC for 8hr. The powders were pressed into pellets and a third reheat to 1200 ^oC for 8 hrs was required to get the desired phase of $LiTa_2PO_8$.

Structural characterisation using X-ray diffraction: A benchtop Miniflex Rigaku Diffractometer using Cu $K\alpha_1$ (λ =1.5405 Å) was used to collect data in the range 10 $^o \leq 2\theta \leq 70$ ^{o}. The data for full Rietveld refinement were collected at a speed of 1 ^{o} min^{-1} and step size of 0.01 ^{o}. A Rietveld refinement against the data was performed using the GSAS II software [107] from the published structure of $LiTa_2PO_8$.[3] Multiple phases were added to some refinements where appropriate to model the impurities. The data were fitted with the shifted Chebyschev background function with 6 terms and the refinements involved the following parameters: lattice parameters, pseudo-Voight parameters for the peak shape and phase fraction.

Structural characterisation using SEM and EDX: Measurements were performed by JM (G. Goodlet 21/4/2020), the following has been provided alongside the results. “for the cross-sections the samples were embedded in resin, ground, polished (by P Verlinden) and carbon-coated for SEM. Sample advised hazards were assessed prior to analysis. The samples were analysed using a Zeiss ultra 55 Field emission electron microscope equipped with in-lens Secondary electron and backscattered detectors.

Compositional analysis and low-resolution general imaging. Accelerating voltage: 20kV Aperture used: 30-60micron Working distance (WD): 7-8mm Detectors: Standard Secondary electron and standard backscattered electron detectors".

SSNMR: Measurements were performed by JM (S. Day 24/10/2022), the following has been provided alongside the results. "SSNMR spectra were acquired at a static magnetic field strength of 14:1 T (0(1H) = 600 MHz) on a Bruker Avance Neo console using TopSpin 4.0 software. For 7Li, the probe was tuned to 233:27 MHz and referenced to 0.1M LiCl at 0:0 ppm. Powdered samples were packed into MAS rotors, with before and after weighings providing the sample mass. Sample advised hazards were assessed. The total experiment time to acquire these spectra was 14 hours."

Electrochemical impedance spectroscopy: Studies were performed on thin pellets of $LiTa_2PO_8$, $LiTa_{1.96}Nb_{0.04}PO_8$, $LiTa_{1.96}Sb_{0.04}PO_8$ sintered with the addition of 2% PVA solution at 1050 ^oC and 1200 ^oC for $LiTa_{1.96}Nb_{0.04}PO_8$ (1 mm, 1.1 mm, 0.7 mm thick, respectively and 13 mm in diameter) using Au electrodes. Au electrodes were sputter coated onto both sides of the pellet using a sputter coater. The sputtering time was 200 s, using 20 mA sputtering current and an Ar pressure of ~0.02 mbar. The pellets were loaded into a CESH-e cell within an Ar-filled glovebox and attached to a MTZ-35 potentiostat via a ITS-e where impedance data were collected using Au current collectors under Ar atmosphere. Impedance data were recorded in the temperature range 293-373 K with intervals of 20 K in the frequency range of 5 MHz to 1 Hz with an electrical perturbation of 10 mV. At each temperature the pellets were left to reach equilibrium for 30 min prior to measurements.

3.3 Results

Structural characterisation of $LiTa_2PO_8$: A Rietveld refinement against room temperature x-ray data for $LiTa_2PO_8$ (**Figure 3.1**) yielded a GOF of 5.12 and Rwp of 8.841. The calculated lattice parameters are a = 9.71664(8) Å, b = 11.53772(9) Å, c = 10.69995(1) Å and β= 90.031(1) ^{o} with a unit cell volume of 1199.50(2) $Å^3$, this is in agreement with the published data: a = 9.71545(2) Å, b = 11.53580(2) Å, c = 10.69708(3) Å, and β = 90.0355(3) °.[3] A small impurity of $LiTa_3O_8$ (0.046 wt. fraction) is present in the sample, similar to that of the published data.

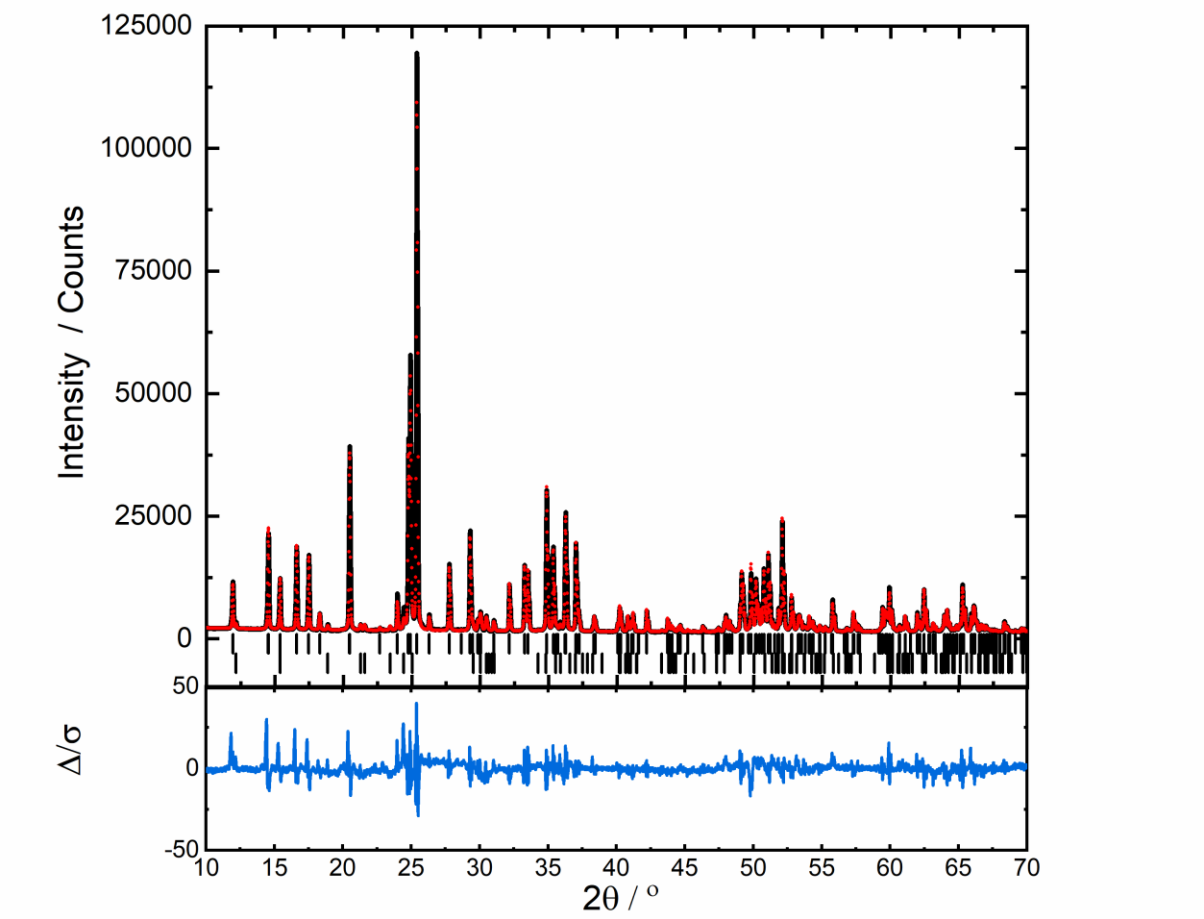

Figure 3.1: Rietveld refinement against room temperature $LiTa_2PO_8$, observed data shown in red circles, calculated in black and Δ/σ in blue. Allowed Bragg reflections for $LiTa_2PO_8$ (upper) and $LiTa_3O_8$ (lower) are shown in dashes below.

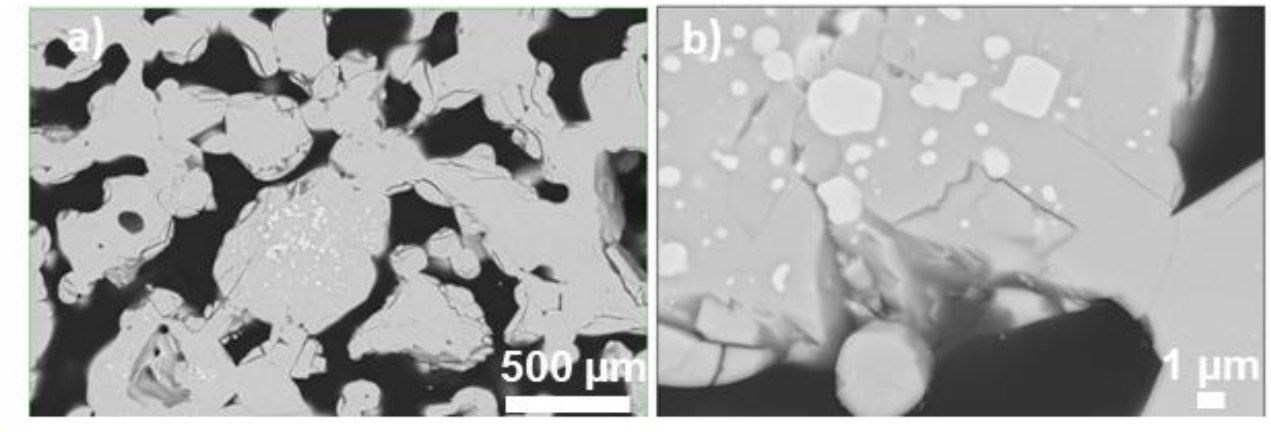

Figure 3.2: SEM images of a $LiTa_2PO_8$ pellet

SEM images (**Figure 3.2**) of a $LiTa_2PO_8$ pellet show large voids between the grains alongside small areas of lighter areas which suggests impurities are present at the surface of the grains, and are likely that of $LiTa_3O_8$ also present in the XRD data. The voids between the grains within the pellet support the low density of the $LiTa_2PO_8$ pellet calculated to be 63%.

Structural characterisation of $LiTa_{2-x}NbxPO_8$: Refinements against data collected for $LiTa_{2-x}NbxPO_8$ (**Figure 3.3**) yielded the statistics shown in **Table 3.1**. When x≥0.2 Nb-containing impurities are present, namely that of Nb_9PO_{25}, indicating that the solubility limit of $LiTa_{2-x}NbxPO_8$ has been reached; the fitting statistics also increase. The change in lattice parameters shown in **Figure 3.4**, involve an increase with initial introduction of Nb followed by a decrease with increase in x up to x=0.2 where the lattice parameter change plateaus. This is accompanied by an increase in β resulting in an overall decrease in unit cell volume.

Table 3.4:Calculated unit cell parameters and fitting statistics for $LiTa_{2-x}Nb_xPO_8$.

x	a/ Å	b/ Å	c/ Å	β/ °	Volume/ Å^3	GOF	R_{wp}
0	9.71664(8)	11.53772(9)	10.69995(1)	90.031	1199.50	5.12	8.841
0.04	9.7213(2)	11.5431(2)	10.7055(2)	90.016(3)	1201.31(3)	4.67	8.234
0.1	9.7212(2)	11.5404(2)	10.7029(2)	90.007(8)	1200.74(4)	4.86	9.043
0.2	9.7184(8)	11.5366(9)	10.7001(8)	90.06(1)	1199.6(2)	14.41	9.127
0.3	9.7188(2)	11.5372(2)	10.6994(2)	89.962(5)	1199.71(4)	5.43	12.521

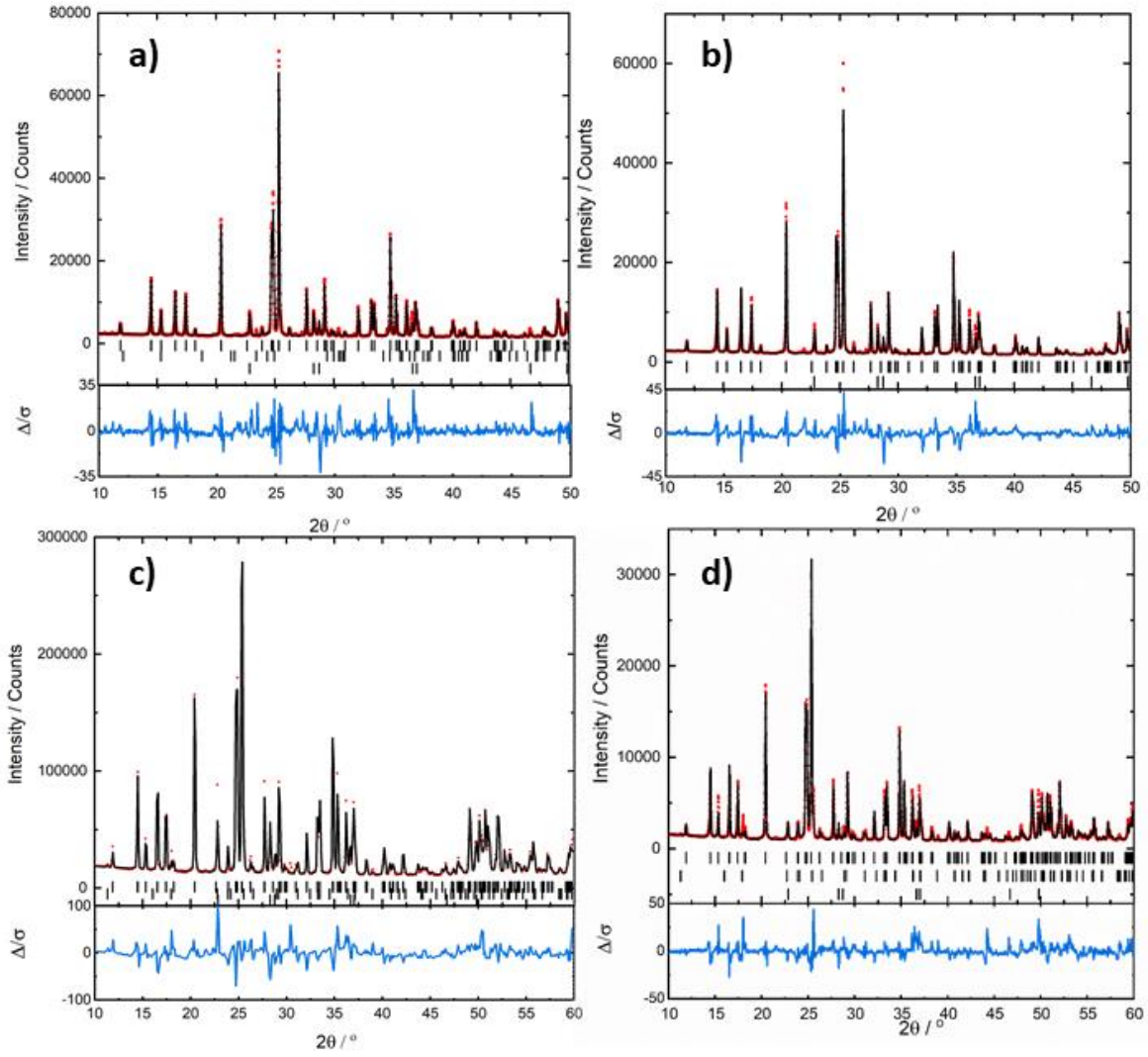

Figure 3.3: Rietveld refinements against room temperature $LiTa_{2-x}NbxPO8$, observed data shown in red circles, calculated in black and Δ/σ in blue. a) Refinement for x=0.04 where allowed Bragg reflections are shown for $LiTa_2PO_8$ (upper), $LiTa_3O_8$ (middle)Ta_2O_5 (Lower). b) Refinement for x=0.1 where allowed Bragg reflections are shown for $LiTa_2PO_8$ (upper) and Ta_2O_5 (Lower). c) Refinement for x=0.2 where allowed Bragg reflections are shown for $LiTa_2PO_8$ (upper), Nb_9PO_{25} (middle) and Ta_2O_5 (Lower). d) Refinement for x=0.3 where allowed Bragg reflections are shown for $LiTa_2PO_8$ (upper), Nb_9PO_{25} (middle) and Ta_2O_5 (Lower).

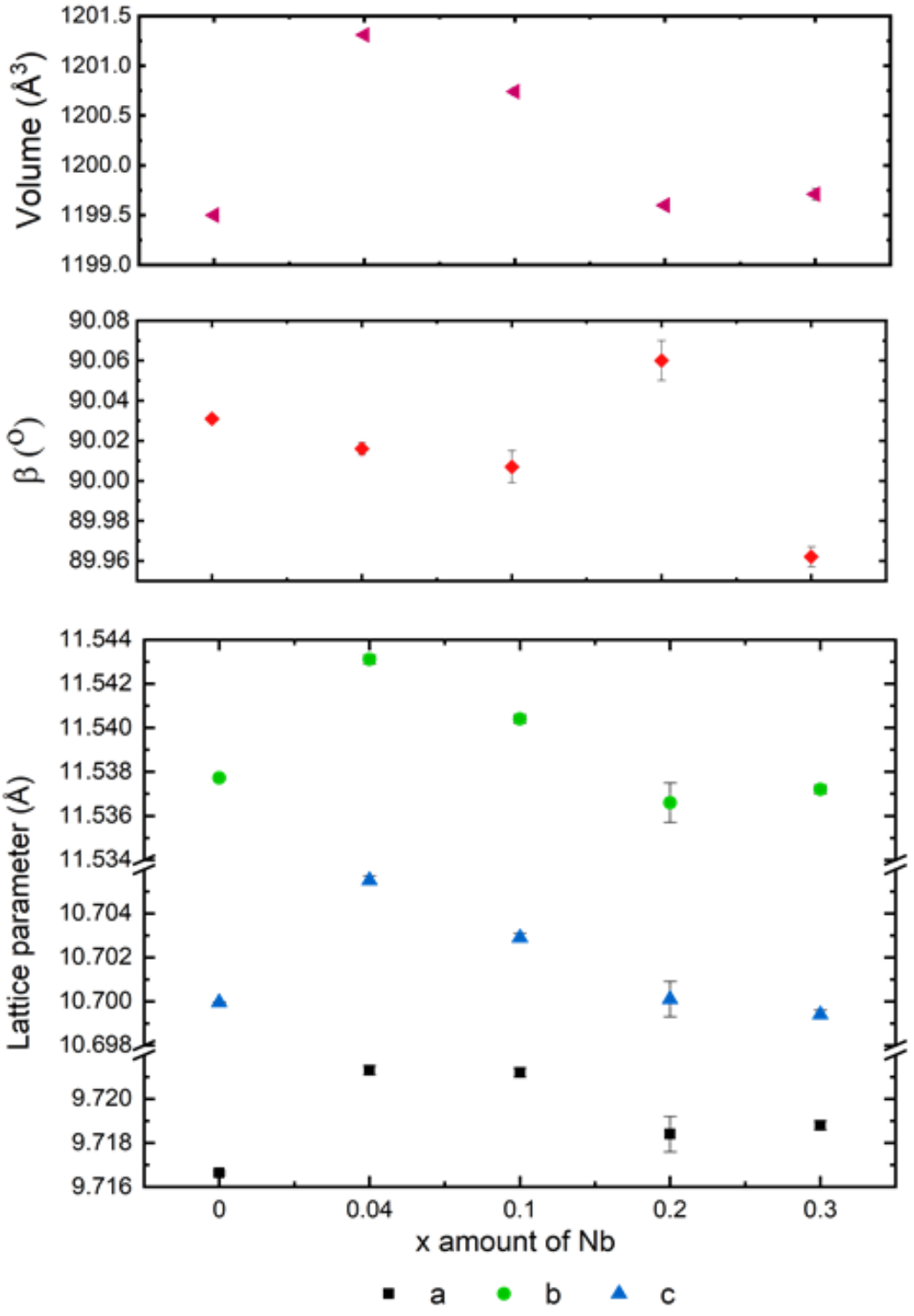

Figure 3.4: Graph showing change in lattice parameters, angle (β) and unit cell volume for $LiTa_{2-x}Nb_xPO_8$.

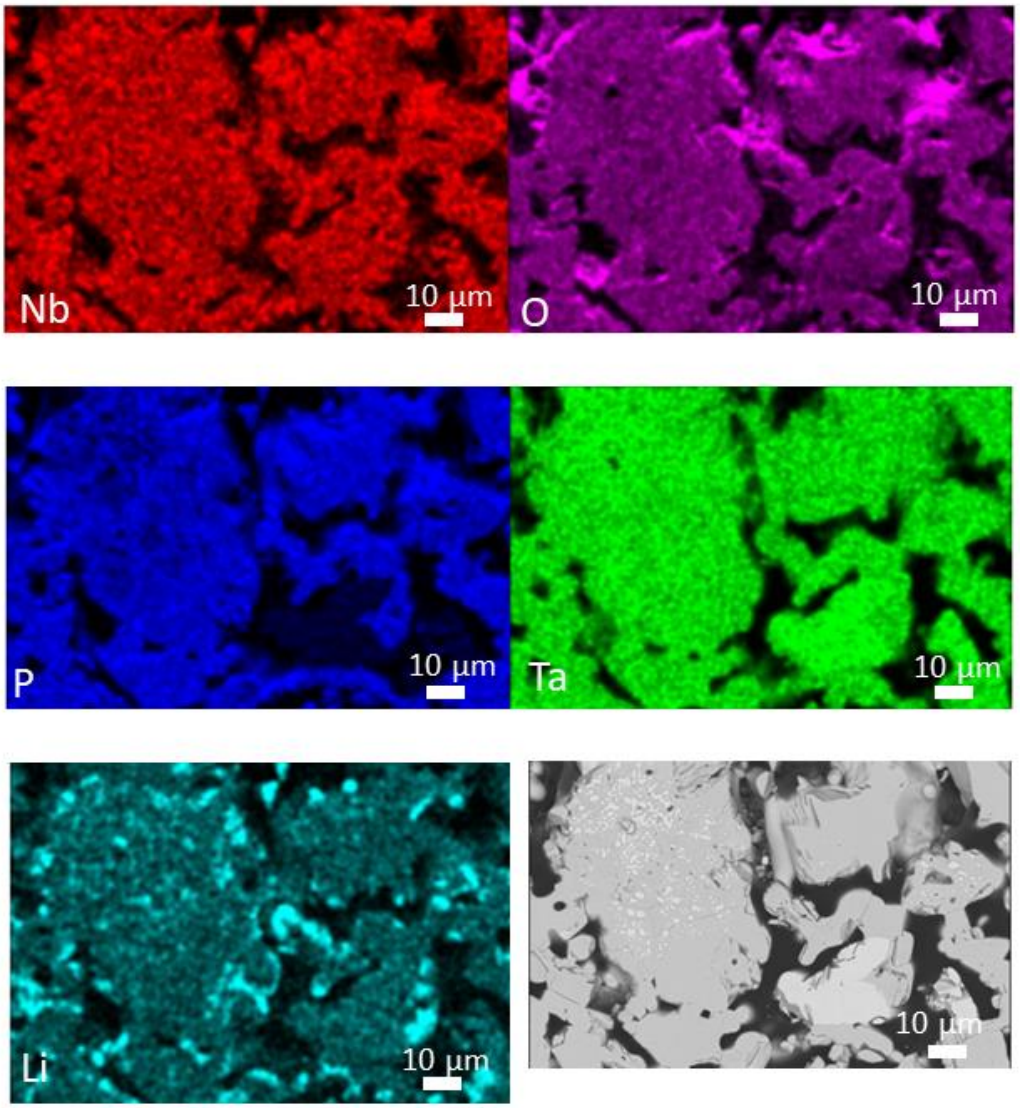

Figure 3.5: SEM image of a $LiTa_{1.96}Nb_{0.04}PO_8$ pellet alongside EDX mapping for Nb, O, P, Ta and Li.

The SEM image shown in **Figure 3.5** shows large voids between the grains for the $LiTa_{1.96}Nb_{0.04}PO_8$ pellet indicating that the pellet used is of similar density to that of the parent $LiTa_2PO_8$ material shown in **Figure 3.2**. The elemental distribution is fairly homogeneous particularly across the pellet, with the exception of a phosphorous deficient area and Li/O rich areas, this could represent the impurities present in this sample, $LiTa_3O_8$ and Ta_2O_5 corresponding to the phosphorous deficient area and $LiOH/Li_2CO_3$ corresponding to the Li/O rich areas which is commonly formed at grain

boundaries in solid electrolyte materials. This homogeneity provides some evidence of Nb incorporation into the $LiTa_2PO_8$ structure.

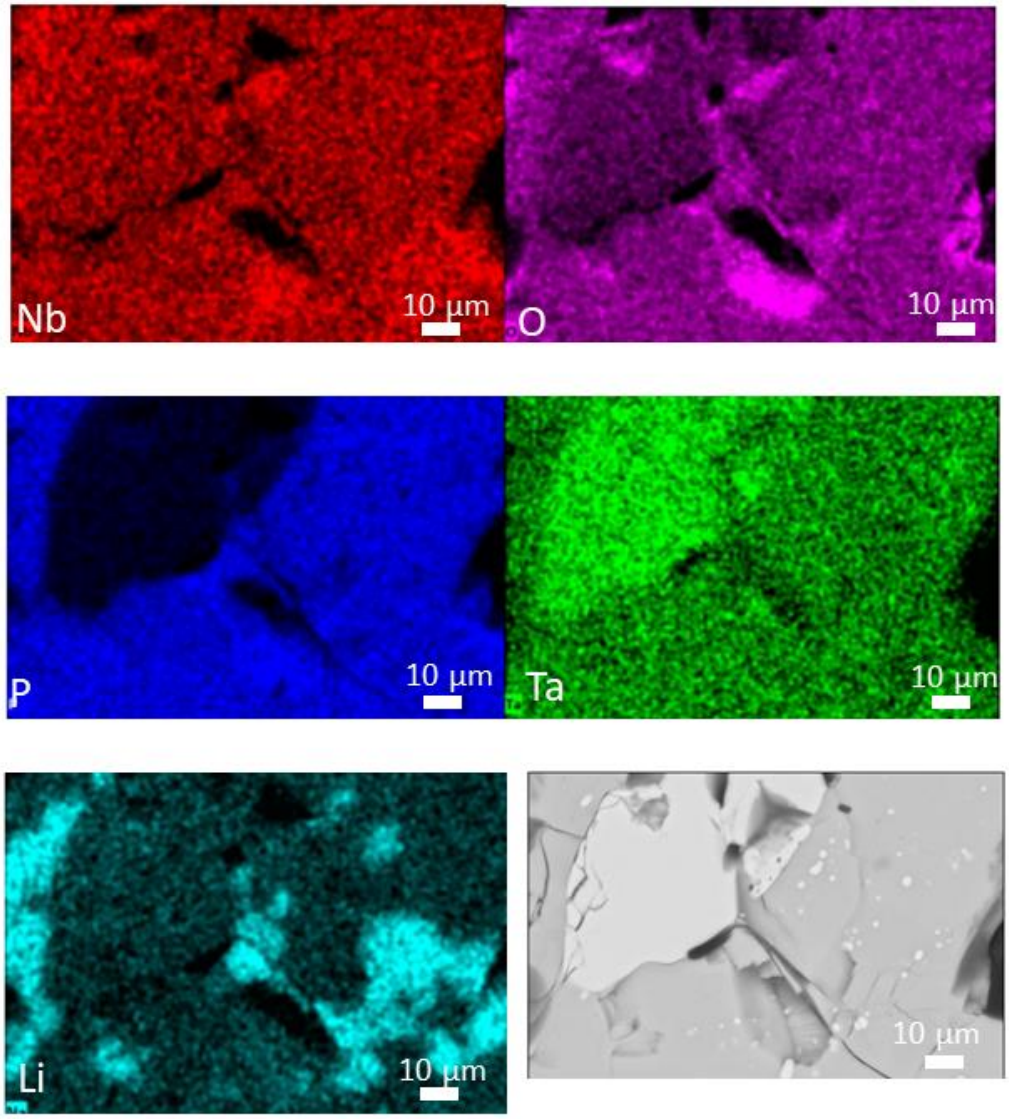

Figure 3.6: SEM image of a $LiTa_{1.90}Nb_{0.1}PO_8$ pellet alongside EDX mapping for Nb, O, P, Ta and Li.

The SEM data for a $LiTa_{1.90}Nb_{0.1}PO_8$ pellet shown in **Figure 3.6,** shows less voids which could indicate better density has been achieved for this sample, however a large void can still be seen to the left of the image. The homogeneity is similar to that of $LiTa_{1.96}Nb_{0.04}PO_8$ pellet and inhomogeneity is likely arising from similar impurities, the exception being small regions of Nb, O and P rich areas which could be attributed to the beginning of the main Nb containing impurity, Nb_9PO_{25}, forming. The majority of

the area measured can be attributed to the parent compound, $LiTa_2PO_8$ with doped Nb incorporated into the lattice structure.

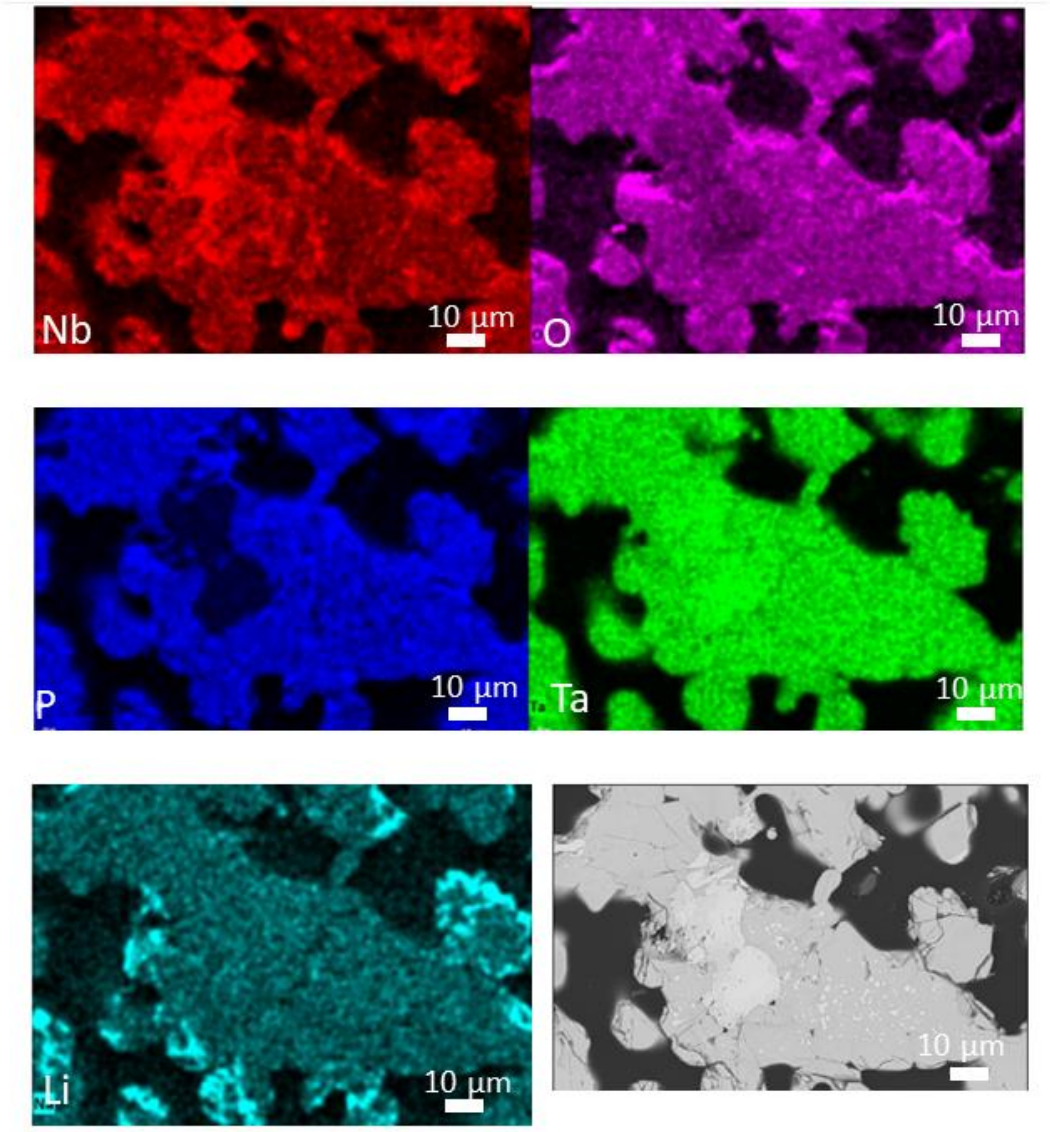

Figure 3.7: SEM image of a $LiTa_{1.8}Nb_{0.2}PO_8$ pellet alongside EDX mapping for Nb, O, P, Ta and Li.

The SEM collected on a $LiTa_{1.8}Nb_{0.2}PO_8$ pellet (**Figure 3.7**) shows larger voids between the grains and hence indicates a lower density of material. The sample is noted as the most heterogeneous of those measured by the SEM instrument scientist, indicating that the total Nb content is unlikely to be fully incorporated within the parent structure and instead is forming impurities within the sample.

The SEM across all doped Nb samples shows large voids between the grains indicating that the pellets used for EIS are low density. The homogeneity of Nb across the grains suggests that Nb can be incorporated into the parent structure however, this limit is reached when x ~0.1. The lack of Nb rich areas in the $LiTa_{1.96}Nb_{0.04}PO_8$ pellet suggests that conductivity measurements performed on this sample would provide the best representation of the conductivity of $LiTa_{2-x}Nb_xPO_8$ for comparison to $LiTa_2PO_8$.

Structural characterisation of $LiTa_{2-x}Sb_xPO_8$: Refinements against data collected for $LiTa_{2-x}Sb_xPO_8$ (**Figure 3.8**) yielded the statistics summarised in **Table 3.2**. When x≥0.2 unindexed peaks begin to form, indicating that the solubility limit of $LiTa_{2-x}Sb_xPO_8$ has been reached, the fitting statistics also increase similar to that obtained for $LiTa_{2-x}Nb_xPO_8$. The change in lattice parameters (**Figure 3.9**) show a decrease with increase in x as expected due to the smaller atomic radii of Sb^{5+} (0.6 Å) in comparison to Ta^{5+} and Nb^{5+} (0.64 Å).[128] At x= 0.2 the lattice parameter change plateaus, this is accompanied by a larger decrease in β resulting in an overall plateau in unit cell volume.

Table 3.2*:* Calculated unit cell parameters and fitting statistics for $LiTa_{2-x}Sb_xPO_8$

x	a/ Å	b/ Å	c/ Å	β/ °	Volume/ Å^3	GOF	R_{wp}
0	9.71664(8)	11.53772(9)	10.69995(1)	90.031(1)	1199.50	5.12	8.841
0.04	9.7086(1)	11.5270(1)	10.6915(1)	90.021(3)	1196.51(2)	3.69	7.012
0.10	9.7048(2)	11.5218(3)	10.6862(2)	90.029(5)	1194.91(6)	6.57	9.561
0.20	9.7035(3)	11.5206(4)	10.6866(3)	89.952(5)	1194.67(9)	8.81	12.889

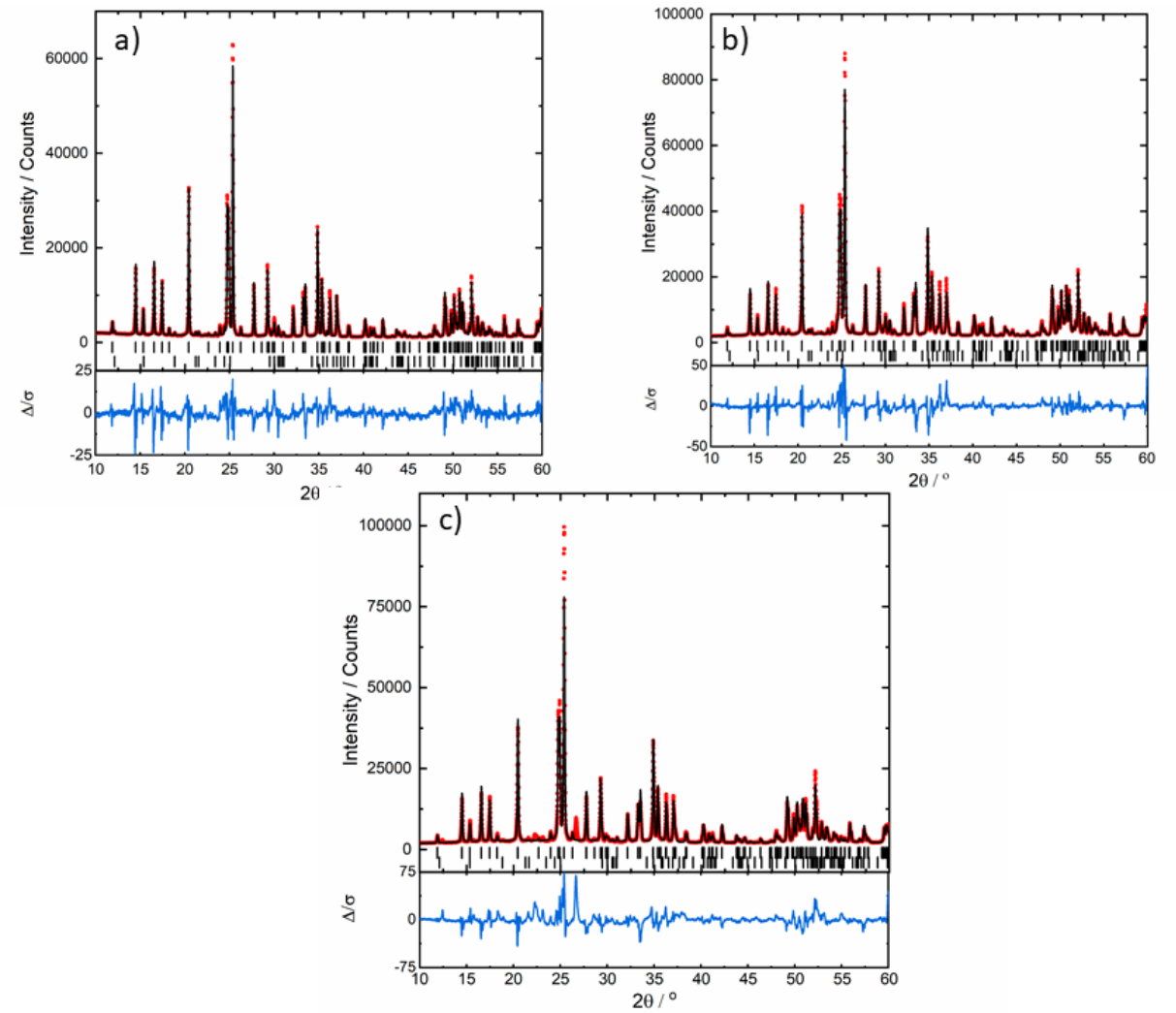

Figure 3.8: Rietveld refinements against room temperature $LiTa_{2-x}Sb_xPO_8$, observed data shown in red circles, calculated in black and Δ/σ in blue. a) Refinement for x=0.04 where allowed Bragg reflections are shown for $LiTa_2PO_8$ (upper) and $LiTa_3O_8$ (Lower) b) Refinement for x=0.1 where allowed Bragg reflections are shown for $LiTa_2PO_8$ (upper) and $LiTa_3O_8$ (Lower) c) Refinement for x=0.2 where allowed Bragg reflections are shown for $LiTa_2PO_8$ (upper) and $LiTa_3O_8$ (Lower).

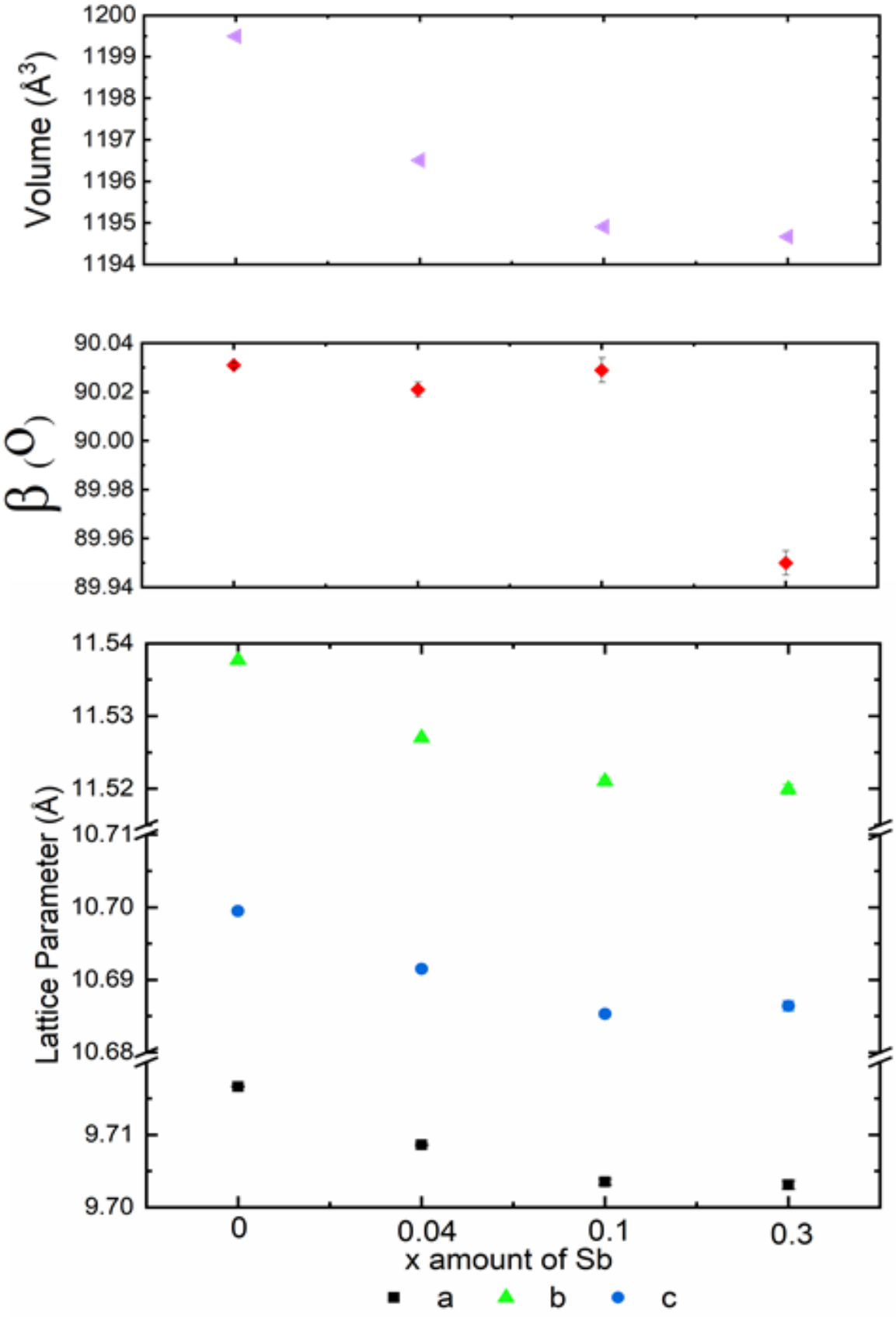

Figure 3.9: Graph showing change in lattice parameters, angle and unit cell volume for $LiTa_{2-x}Sb_xPO_8$.

Refinements against data collected for $Li_{1+x}Ta_{2-x}Zr_xPO_8$ (**Figure 3.10**) yielded the statistics summarised in **Table 3.3**. When x=0.25 Bragg reflections for $LiZr_2(PO_4)_3$ appear, indicating that the solubility limit of $Li_{1+x}Ta_{2-x}Zr_xPO_8$ has been reached. The change in lattice parameters (**Figure 3.11**) shows a small decrease in lattice parameter *b* when x=0.1 with parameters *a* and *c* and unit cell volume remaining almost constant. This is unusual as Zr has a larger ionic radii (0.72 Å) in comparison to Ta^{5+} (0.64 Å).[128] At x= 0.25 the lattice parameters increase accompanied by a decrease in β resulting in an overall increase in unit cell volume. As impurities are also present in the x=0.25 sample, the solubility of $Li_{1+x}Ta_{2-x}Zr_xPO_8$ is reached and the unit cell has increased as expected with the incorporation of the larger Zr^{4+} ion.

Table 3.3: Calculated unit cell parameters and fitting statistics for $Li_{1+x}Ta_{2-x}Zr_xPO_8$.

x	a/ Å	b/ Å	c/ Å	β / °	Volume/ Å^3	GOF	R_{wp}
0	9.71664 (8)	11.53772(9)	10.69995(1)	90.031(1)	1199.50	5.12	8.841
0.1	9.7168(2)	11.5350 (2)	10.6992 (2)	90.069(2)	1199.21 (4)	3.54	7.059
0.25	9.7216(2)	11.5421 (2)	10.7037 (2)	89.932(2)	1201.05 (5)	4.29	7.7

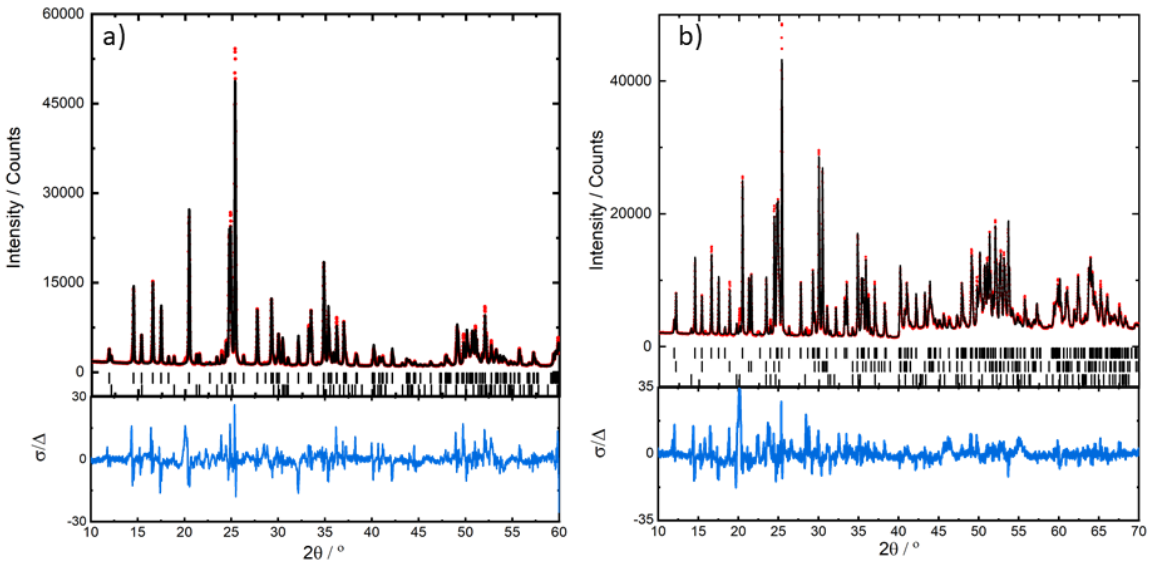

Figure 3.10: Rietveld refinements against room temperature $Li_{1+x}Ta_{2-x}Zr_xPO_8$ observed data shown in red circles, calculated in black and Δ/σ in blue. a) Refinement for x=0.1 where allowed Bragg reflections are shown for $LiTa_2PO_8$ (upper) and $LiTa_3O_8$ (Lower) b) Refinement for x=0.1 where allowed Bragg reflections are shown for $LiTa_2PO_8$ (upper), $LiTa_3O_8$ (middle) and $LiZr_2(PO_4)_3$ (lower)

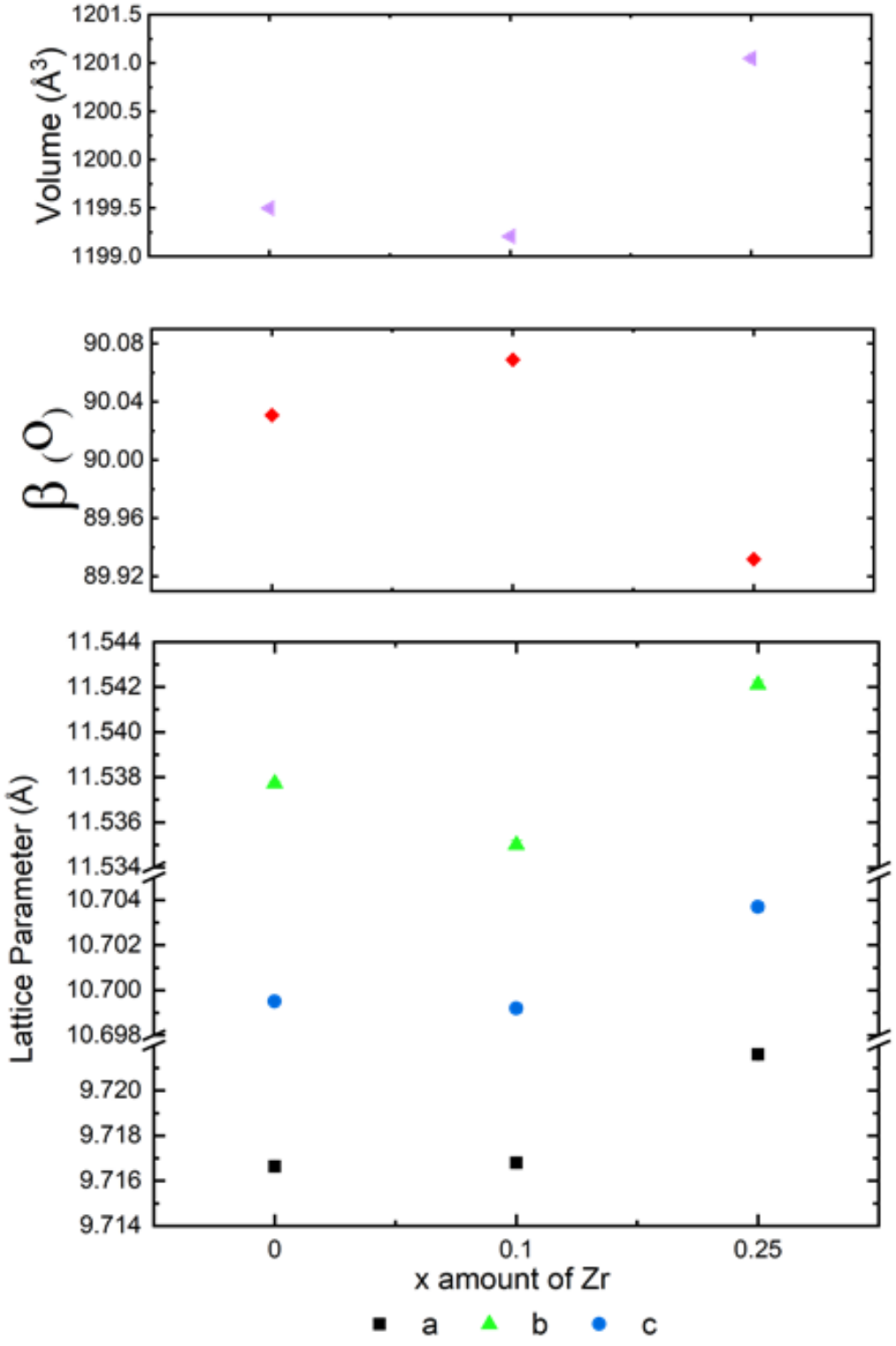

Figure 3.115: Graph showing change in lattice parameters, angle and unit cell volume for $Li_{1+x}Ta_{2-x}Zr_xPO_8$.

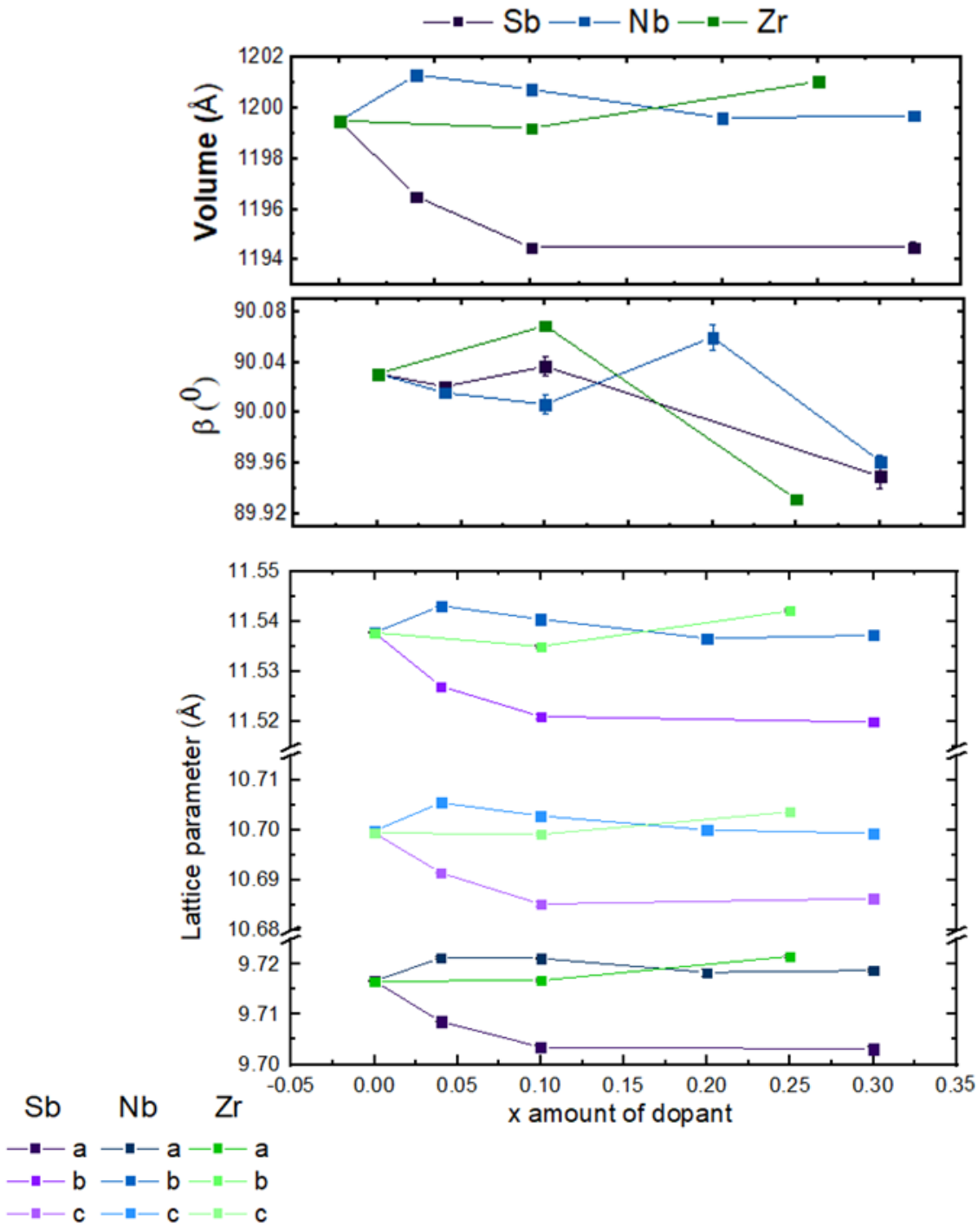

Figure 3.12: Graph showing change in lattice parameters, angle and unit cell volume for $LiTa_{2-x}Sb_xPO_8$ in purple, $LiTa_{2-x}Nb_xPO_8$ in blue and $Li_{1+x}Ta_{2-x}Zr_xPO_8$ in green. Error bars are shown but are smaller than the markers in some cases.

The results for all doped samples (**Figure 3.12**) indicate that the solubility limit for doping is ~ x=0.1, after which impurities begin to form and changes in lattices parameters decrease. Comparing all three doped samples at x=0.1 $LiTa_{2-x}Nb_xPO_8$ increases in volume and size, $LiTa_{2-x}Sb_xPO_8$ decreases in volume and size and $Li_{1+x}Ta_{2-x}Zr_xPO_8$ remains almost constant with respect to pristine $LiTa_2PO_8$. This is unusual due to the difference in atomic radii, with Zr being the largest and Sb being the smallest, the trend observed indicates that the incorporation of dopants must lead to small structural changes occurring within the unit cell.

Electrochemical characterisation of $LiTa_2PO_8$:

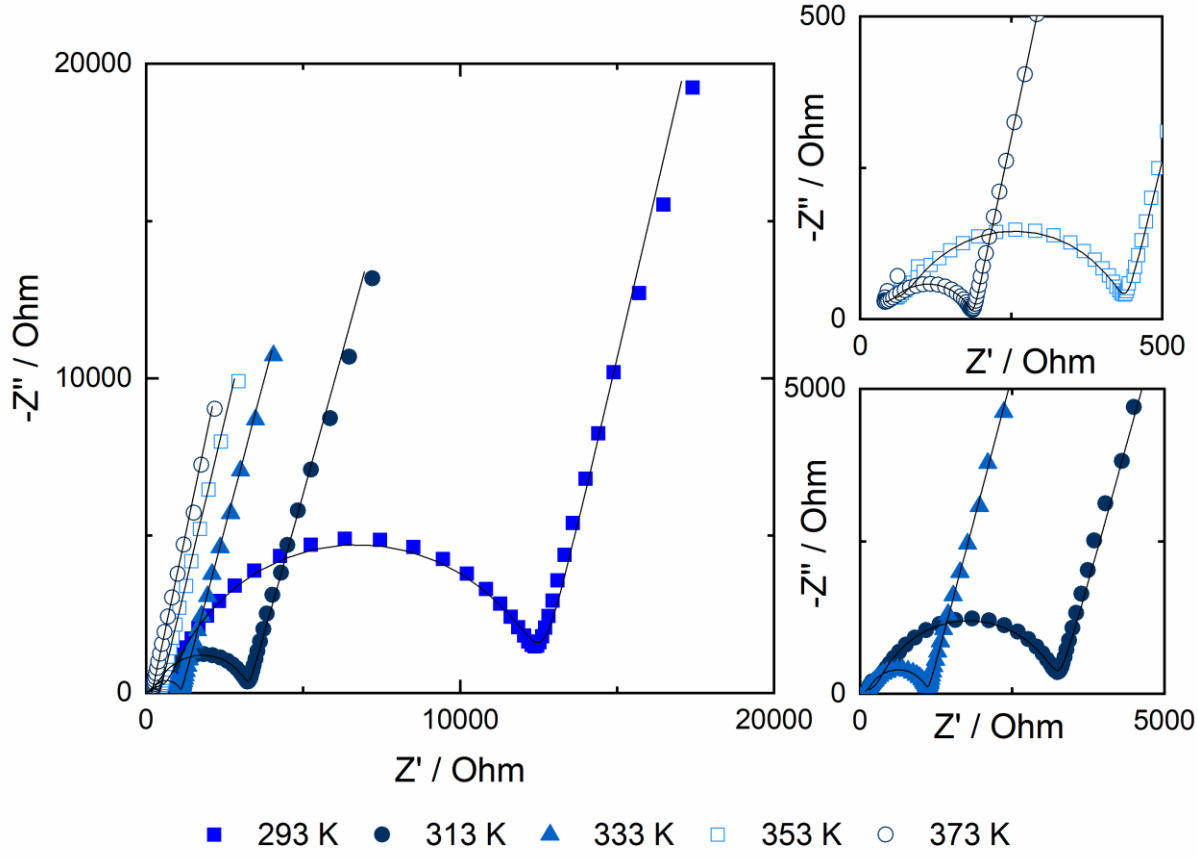

Figure 3.13: Nyquist plots showing impedance data collected from a $LiTa_2PO_8$ pellet in the temperature range 293-373 K, with the fit shown in black. The insets shown are zoomed in on the temperatures shown.

Table 3.4: Summary of the conductivities calculated from the fitted Nyquist plots used to generate Arrhenius plots to calculate the activation energy of Li^+ hopping for $LiTa_2PO_8$.

T/ K	Bulk conductivity/ S cm^{-1}	Grain boundary conductivity/ S cm^{-1}	Total conductivity/ S cm^{-1}
293	1.19(5) x 10-4	6.22(8) x 10-6	5.915(5) x 10-6
313	3.2(1) x 10-4	2.46(2) x 10-5	2.289(2) x 10-5
333	7.0(2) x 10-4	7.39(6) x 10-5	6.686(4) x 10-5
353	1.19(3) x 10-3	2.00(1) x 10-4	1.7109(7) x 10-4
373	2.10(5) x 10-3	4.98(4) x 10-4	4.028(1) x 10-4

The electrochemical impedance spectroscopy data obtained for $LiTa_2PO_8$ (**Figure 3.13**) were fitted with the equivalent circuit [R1CPE1][R2CPE2]CPE3, comparable to that used in the first published investigation.[3] Where R1 is the resistance associated with the bulk and R2 the resistance associated with the grain boundary, the assignments were based on the published model. CPE3 was used to model the low frequency spike attributed to Li^+ blocking at the electrodes. The fitted value of R1 was then used to calculate the bulk ionic conductivity which was found to be 1.19(5) x 10^{-4} S cm^{-1} at 293 K. The grain boundary contribution was calculated using the fitted value of R2 and was found to be 6.22(8) x 10^{-6} S cm^{-1} at 293 K, leading to a total ionic conductivity at 293 K, (R1+R2), of 5.915(5) x 10^{-6} S cm^{-1}. The conductivities calculated in the range 293 – 373 K are listed in **Table 3.4** and used to form Arrhenius plots (**Figure 3.14**) to calculated the activation energy of Li^+ hopping, within the bulk and grain boundary, calculated to be 0.35(1) eV and 0.538(4) eV respectively. This is slightly higher than that proposed in the first published investigation of 0.32 eV and 0.46 eV, respectively.[3] The relative density of the pellet was much lower than that published (sample A 96.6%)[3] and is calculated to be ~63%.

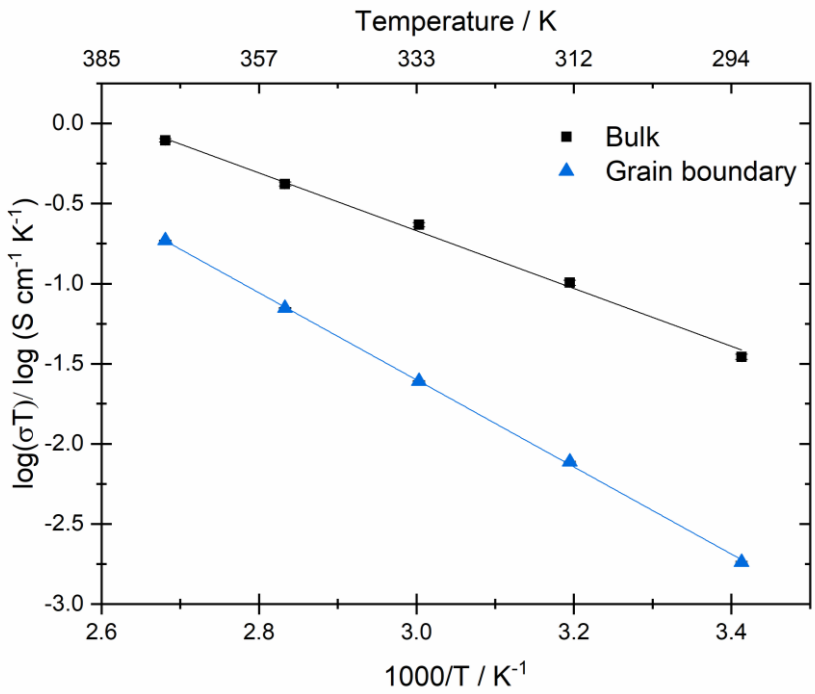

Figure 3.14: Arrhenius plots generated using EIS data used to calculate the activation energy of Li^+ hopping in $LiTa_2PO_8$.

Electrochemical characterisation of $LiTa_{1.96}Nb_{0.04}PO_8$: **Figure 3.15** shows the electrochemical impedance spectroscopy data obtained for $LiTa_{1.96}Nb_{0.04}PO_8$ the data were also fitted with the equivalent circuit [R1CPE1][R2CPE2]CPE3. The fitted value of R1 was then used to calculate the bulk ionic conductivity which was found to be 9.6(4) x 10^{-6} S cm $^{-1}$ at 293 K. The grain boundary contribution was calculated using the fitted value of R2 and was found to be 9.2(1) x 10^{-7} S cm $^{-1}$ at 293 K, leading to a total ionic conductivity at 293 K (R1+R2) of 9.193(8) x 10^{-7} S cm $^{-1}$. The bulk ionic conductivity is ~2 orders of magnitude lower than that of the parent structure $LiTa_2PO_8$, indicating that doping with Nb does not yield an improvement of bulk ionic conductivity. Arrhenius plots (**Figure 3.16**) were assembled using the data in **Table 3.5** and enabled the activation energy of Li^+ hopping to be calculated, with the bulk activation energy calculated to be 0.33(2) eV and the grain boundary calculated to be 0.546(5) eV. The bulk activation energy is lower than that calculated for the parent compound, which could suggest local ease of Li^+ movement, however long-range movement is hindered represented by the lower ionic conductivity.

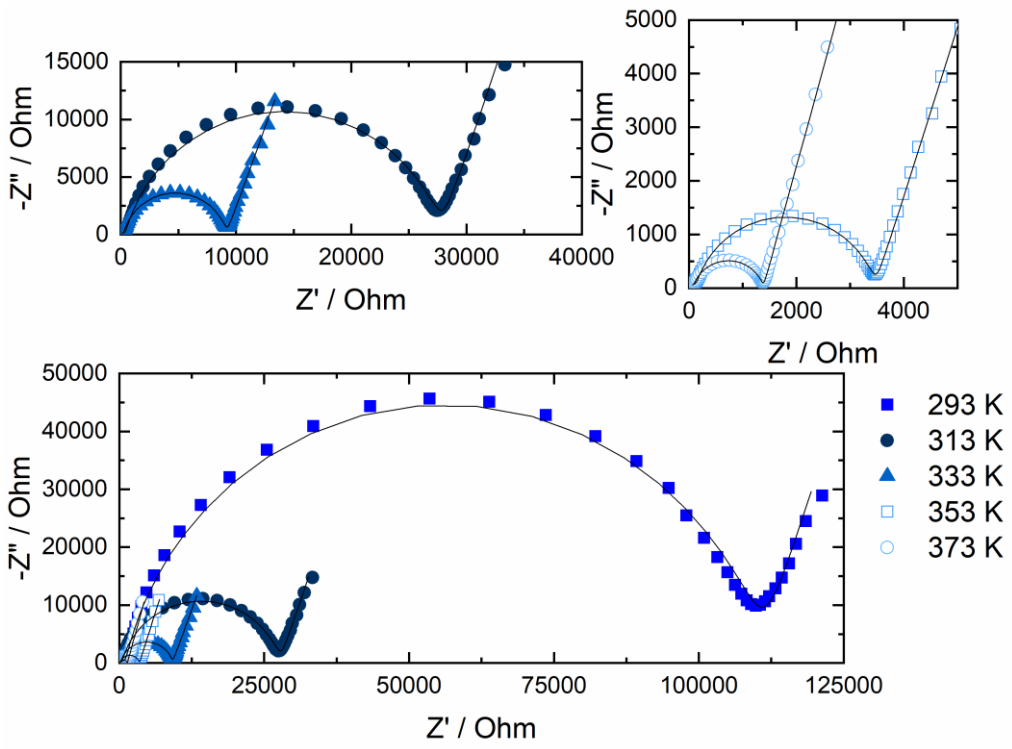

Figure 3.15: Nyquist plots showing impedance data collected from a $LiTa_{1.96}Nb_{0.04}PO_8$ pellet in the temperature range 293-373 K, with the fit shown in black. The insets shown are zoomed in on the temperatures shown.

Table 3.5: Summary of conductivities calculated from fitted data shown in the Nyquist plot used in Arrhenius plots for calculating the activation energy of Li^+ hopping in $LiTa_{1.96}Nb_{0.04}PO_8$.

T/ K	Bulk conductivity/ S cm^{-1}	Grain boundary conductivity/ S cm^{-1}	Total conductivity/ S cm^{-1}
293	9.60.3(4) x 10-5	9.2(2) x 10-7	9.193(8) x 10-7
313	2.75(9) x 10-4	3.72(5) x 10-6	3.667(3) x 10-6
333	4.2(2) x 10-4	1.140(6) x 10-5	1.1098(8) x 10-5
353	8.2(2) x 10-4	3.05(1) x 10-5	2.936(1) x 10-5
373	1.39(3) x 10-3	7.764(3) x 10-5	7.354(2) x 10-5

Figure 3.15 shows the electrochemical impedance spectroscopy data obtained for $LiTa_{1.96}Nb_{0.04}PO_8$ the data were also fitted with the equivalent circuit [R1CPE1][R2CPE2]CPE3. The fitted value of R1 was then used to calculate the bulk ionic conductivity which was found to be 9.6(4) x 10^{-6} S cm^{-1} at 293 K. The grain boundary contribution was calculated using the fitted value of R2 and was found to be

9.2(1) x 10^{-7} S cm $^{-1}$ at 293 K, leading to a total ionic conductivity at 293 K (R1+R2) of 9.193(8) x 10^{-7} S cm $^{-1}$. The bulk ionic conductivity is ~2 orders of magnitude lower than that of the parent structure $LiTa_2PO_8$, indicating that doping with Nb does not yield an improvement of bulk ionic conductivity. Arrhenius plots (**Figure 3.16**) were assembled using the data in **Table 3.5** and enabled the activation energy of Li^+ hopping to be calculated, with the bulk activation energy calculated to be 0.33(2) eV and the grain boundary calculated to be 0.546(5) eV. The bulk activation energy is lower than that calculated for the parent compound, which could suggest local ease of Li^+ movement, however long range movement is hindered represented by the lower ionic conductivity.

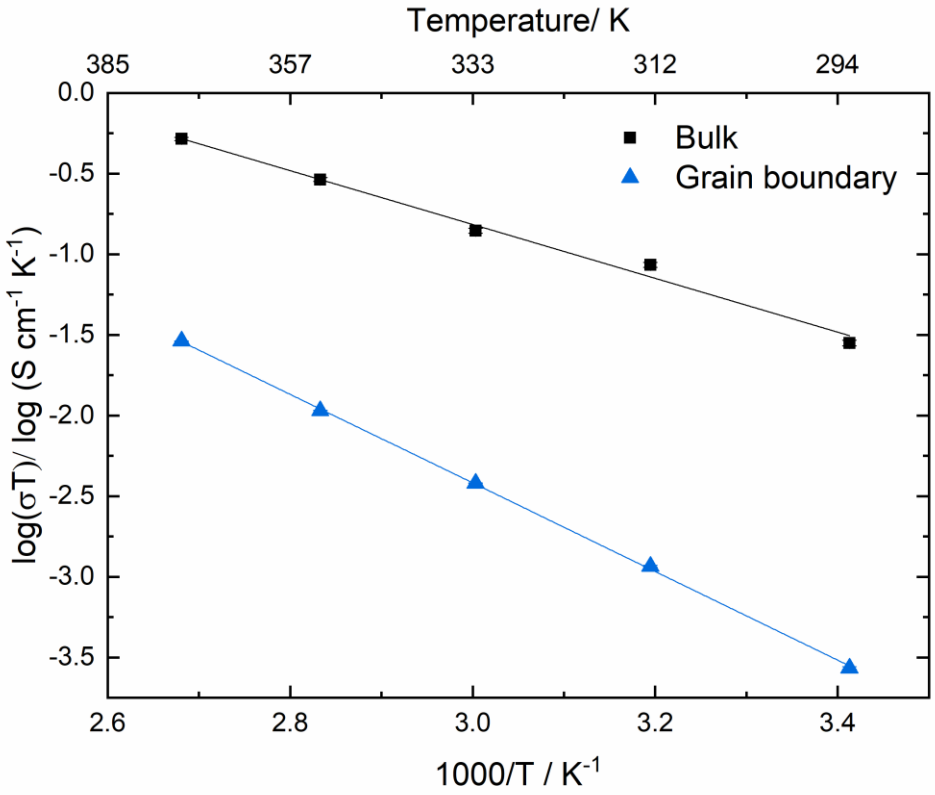

Figure 3.16: Arrhenius plots used to calculate the activation energy of Li^+ hopping in $LiTa_{1.96}Nb_{0.04}PO_8$

Electrochemical characterisation of $LiTa_{1.96}Sb_{0.04}PO_8$: **Figure 3.17** shows the electrochemical impedance spectroscopy data obtained for $LiTa_{1.96}Sb_{0.04}PO_8$ the data were also fitted with the equivalent circuit [R1CPE1][R2CPE2]CPE3. The calculated value of R1 was used to calculate the bulk ionic conductivity which was found to be

1.6(1) x 10^{-4} S cm $^{-1}$ at 293 K. The grain boundary contribution was calculated using the fitted value of R2 and was found to be 4.63(7) x 10^{-6} S cm $^{-1}$ at 293 K, leading to a total ionic conductivity at 293 K (R1+R2) of 3.670(8) x 10^{-6} S cm $^{-1}$. The bulk ionic conductivity is similar to that of the parent structure $LiTa_2PO_8$, indicating that doping with Sb does not yield a significant improvement of the bulk ionic conductivity, however does not hinder the long range movement of Li^+ ions in a way similar to that of Nb doping. **Table 3.6** shows the full conductivities calculated and used to build Arrhenius plots (**Figure 3.18**). The bulk activation energy was calculated to be 0.37(1) eV and the grain boundary calculated to be 0.550(4) eV. The activation energy attributed to Li^+ hopping in the bulk is higher than that calculated for the parent structure and Nb doped structures, indicating local Li^+ hopping is obstructed, yet long range movement can still be accomplished easier than in the case of Nb Doping.

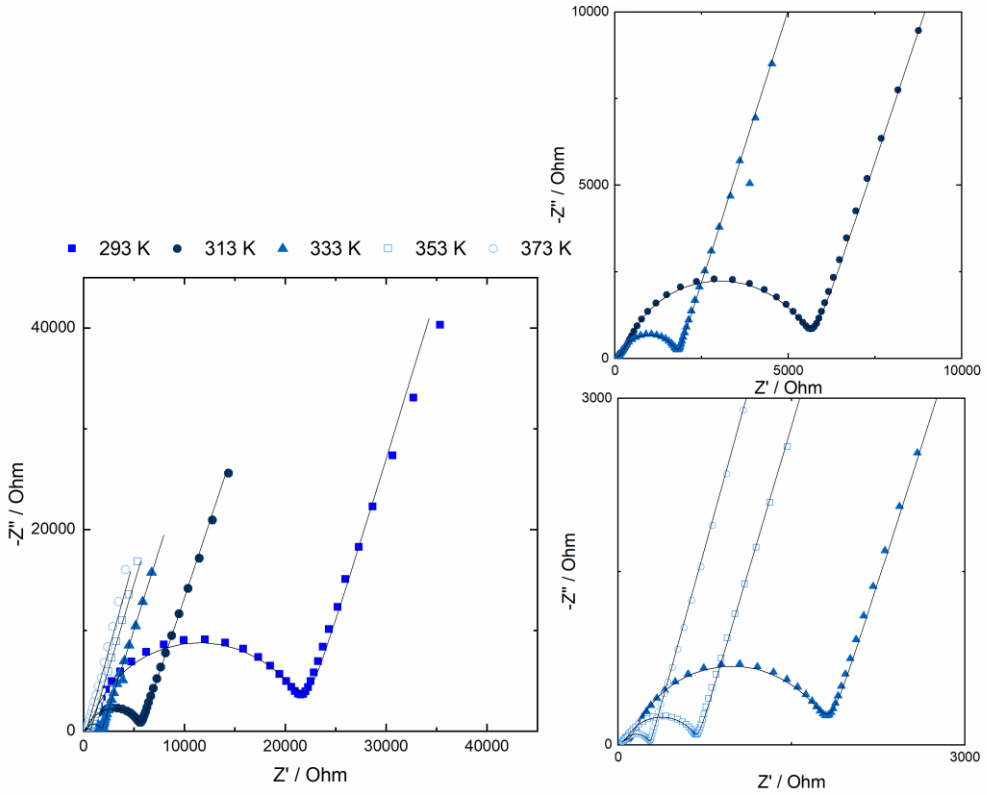

Figure 3.17: Nyquist plots showing impedance data collected from a $LiTa_{1.96}Sb_{0.04}PO_8$ pellet in the temperature range 293-373 K, with the fit shown in black. The insets shown are zoomed in on the temperatures shown.

Table 3.6: Summary of conductivities calculated from fitted data shown in the Nyquist plot used in Arrhenius plots for calculating the activation energy of Li^+ hopping in $LiTa_{1.96}Sb_{0.04}PO_8$.

T/ K	Bulk conductivity/ S cm^{-1}	Grain boundary conductivity/ S cm^{-1}	Total conductivity/ S cm^{-1}
293	1.6(1) x 10-4	4.63(7) x 10-6	3.670(8) x 10-6
313	2.8(4) x 10-4	1.86(3) x 10-5	1.42(1) x 10-5
333	7.4(5) x 10-4	5.86(6) x 10-5	4.43(1) x 10-5
353	1.60(7) x 10-3	1.58(1) x 10-4	1.175(1) x 10-4
373	3.0(1) x 10-3	4.03(3) x 10-4	2.900(2) x 10-4

Figure 3.17 shows the electrochemical impedance spectroscopy data obtained for $LiTa_{1.96}Sb_{0.04}PO_8$ the data were also fitted with the equivalent circuit [R1CPE1][R2CPE2]CPE3. The calculated value of R1 was used to calculate the bulk ionic conductivity which was found to be 1.6(1) x 10^{-4} S cm^{-1} at 293 K. The grain boundary contribution was calculated using the fitted value of R2 and was found to be 4.63(7) x 10^{-6} S cm^{-1} at 293 K, leading to a total ionic conductivity at 293 K (R1+R2) of 3.670(8) x 10^{-6} S cm^{-1}. The bulk ionic conductivity is similar to that of the parent structure $LiTa_2PO_8$, indicating that doping with Sb does not yield a significant improvement of the bulk ionic conductivity, however, does not hinder the long range movement of Li^+ ions in a way similar to that of Nb doping. **Table 3.6** shows the full conductivities calculated and used to build Arrhenius plots (**Figure 3.18**). The bulk activation energy was calculated to be 0.37(1) eV and the grain boundary calculated to be 0.550(4) eV. The activation energy attributed to Li^+ hopping in the bulk is higher than that calculated for the parent structure and Nb doped structures, indicating local Li^+ hopping is obstructed, yet long range movement can still be accomplished easier than in the case of Nb Doping.

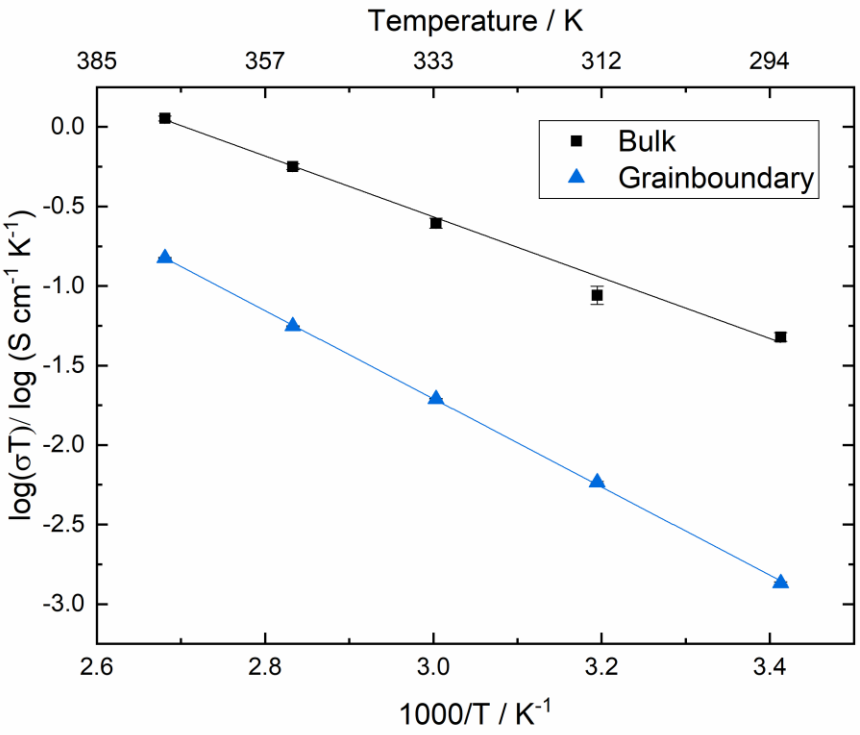

Figure 3.18: Arrhenius plots used to calculate the activation energy of Li^+ hopping in $LiTa_{1.96}Sb_{0.04}PO_8$.

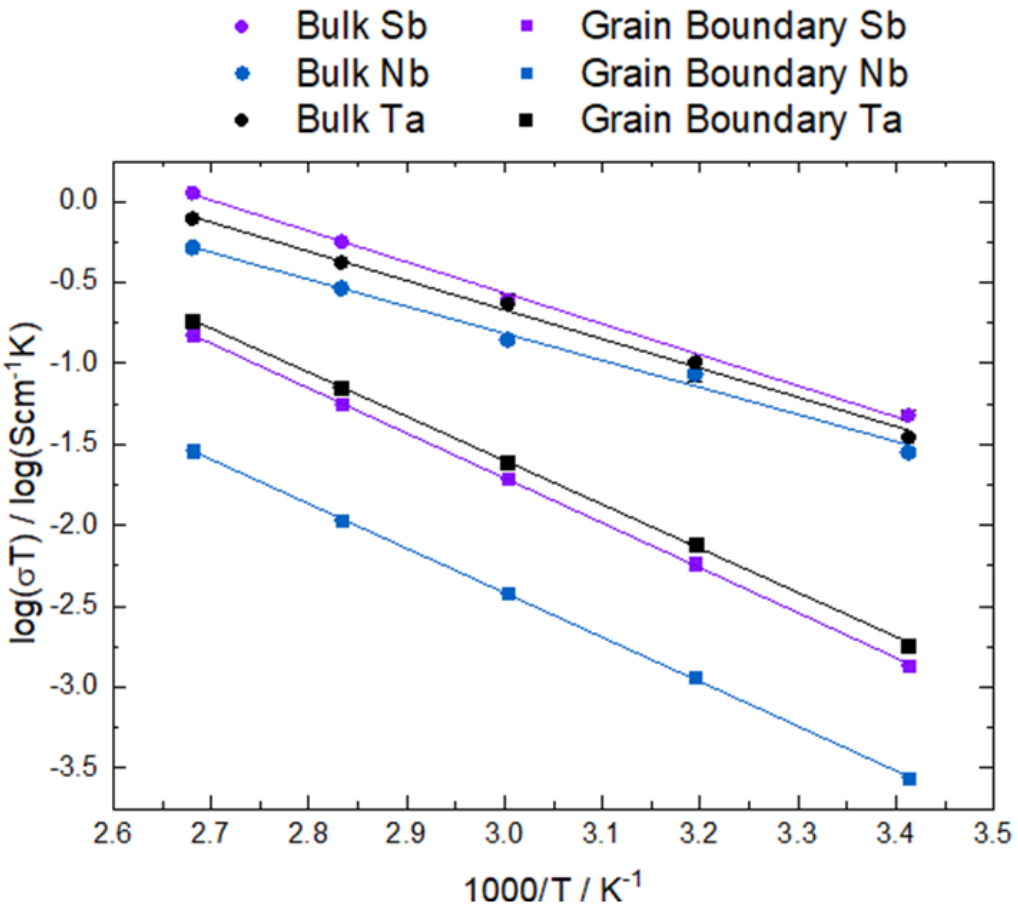

Figure 3.19: Arrhenius plots used to calculate the activation energy of Li^+ hopping in $LiTa_{1.96}Nb_{0.04}PO_8$ in blue, $LiTa_{1.96}Sb_{0.04}PO_8$ in purple and $LiTa_2PO_8$ in black.

Table 3.7: Comparison of Li^+ hopping activation energies from EIS data calculated for $LiTa_{1.96}Sb_{0.04}PO_8$, $LiTa_{1.96}Nb_{0.04}PO_8$, $LiTa_2PO_8$ alongside the published data.

Dopant	**Bulk activation energy (eV)**	**Grain boundary activation energy (eV)**
Ta	0.35(1)	0.538(4)
Nb	0.33(2)	0.546(5)
Sb	0.37(1)	0.550(4)
Published [3]	0.32	0.46

The results shown in **Figure 3.19** shows that the bulk conductivities for all dopants is similar with Sb doping showing a small increase in conductivity overall than those measured, Nb doping results in a decrease in conductivity within the bulk in

comparison to those measured. The grain boundary conductivity for Nb doping is also ~2 orders of magnitude lower than that of Sb doping and the parent compound. This can indicate a large interfacial resistance between the grains or a decrease in density of the pellet. The bulk activation energy for Nb doping is the greatest of those measured and comparable to that of the published parent compound. The grain boundary activation energy for all measured compounds is much greater than that of the parent compound, as the density of the synthesised parent compound is ~63% it Is likely that the density across all measured samples is lower than that of published compound and hence the grain boundary resistance and activation energy is increased.

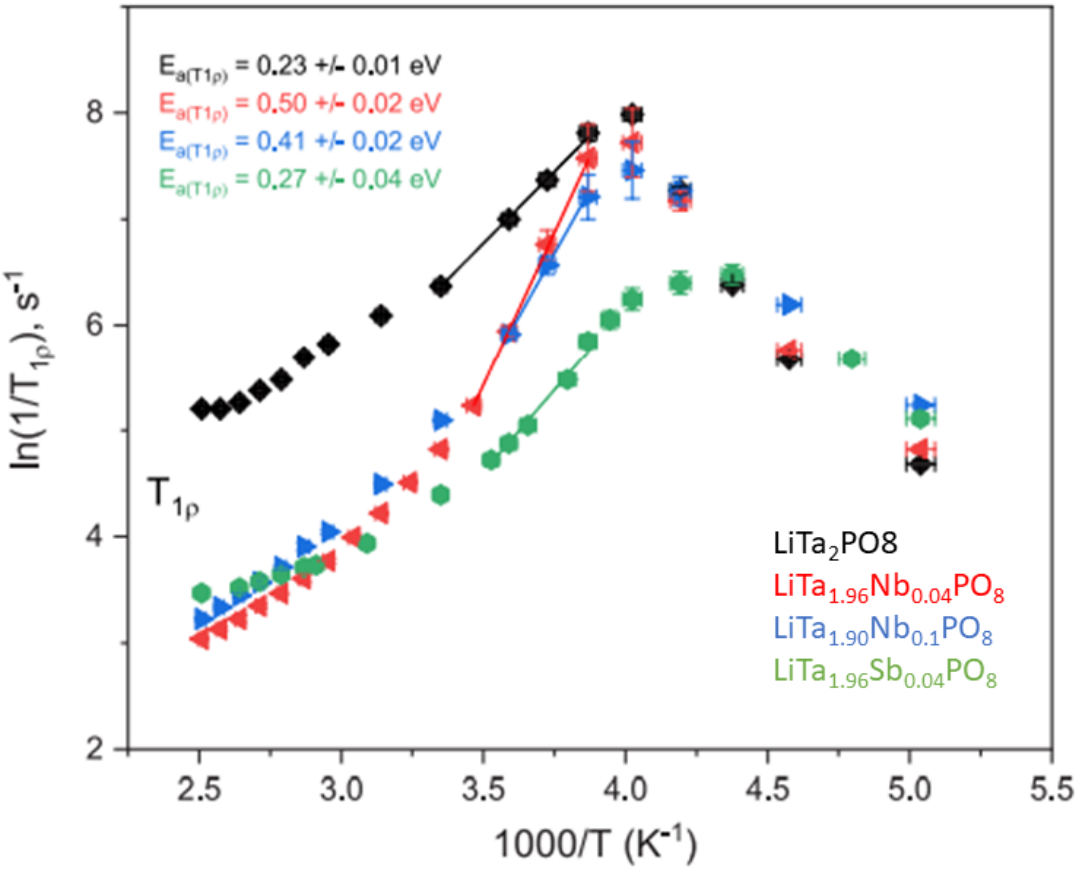

Figure 3.20: The natural logarithm of the inverse of the 7Li spin-lock relaxation rates (T1) plotted against the inverse temperature to estimate an activation energy for lithium motion for the samples shown. $LiTa_2PO_8$ in black, $LiTa_{1.96}Nb_{0.04}PO_8$ in red, $LiTa_{1.90}Nb_{0.1}PO_8$ in blue and $LiTa_{1.96}Sb_{0.04}PO_8$ in green.

The SSNMR data shown in **Figure 3.20** shows the calculated Li^+ hopping activation energies across the measured samples with the parent compound having an intrinsic activation energy of 0.23(1) eV the lowest across the samples. The data also indicates a complicated diffusion mechanism through the materials consistent with more than one lithium diffusion pathway. The calculated intrinsic activation energy of Sb doped material is calculated to be 0.27(4) eV, within error of the SSNMR calculated parent material. The Nb doped samples have a higher intrinsic activation energy, where the comparable 2% doped Nb sample has an activation energy of 0.50(2) eV. The peak in the Sb data occurs at a much lower temperature suggesting fast lithium conduction occurs in this material at a lower temperature to that of the Ta and Nb doped samples. This suggests that Sb doped is the most promising solid electrolyte of those measured. The activation energies calculated using SSNMR data differ to the activation energies calculated via impedance spectroscopy for all samples and suggests the physical properties of the pellet can greatly affect the conductivity of the material. Sb doping shows the greatest improvement in the conductivity shown in both the SSNMR data and EIS data.

3.4 Discussion

Structural changes of $LiTa_2PO_8$ with doping: The structure of $LiTa_2PO_8$ is described in detail in Ref [3] and shown in **Figure 3.21**. The structure consists of corner sharing TaO_6 octahedra and PO_4 tetrahedra with 3 different Li sites forming a 3D pathway capable of Li-ion conduction through the structure. Thus far no research has been performed to generate other family members of the $LiTa_2PO_8$ structural family and attempts to synthesise $LiNb_2PO_8$ and $LiSb_2PO_8$ were unsuccessful, suggesting tantalum is needed in the structure and offers some form of stability.

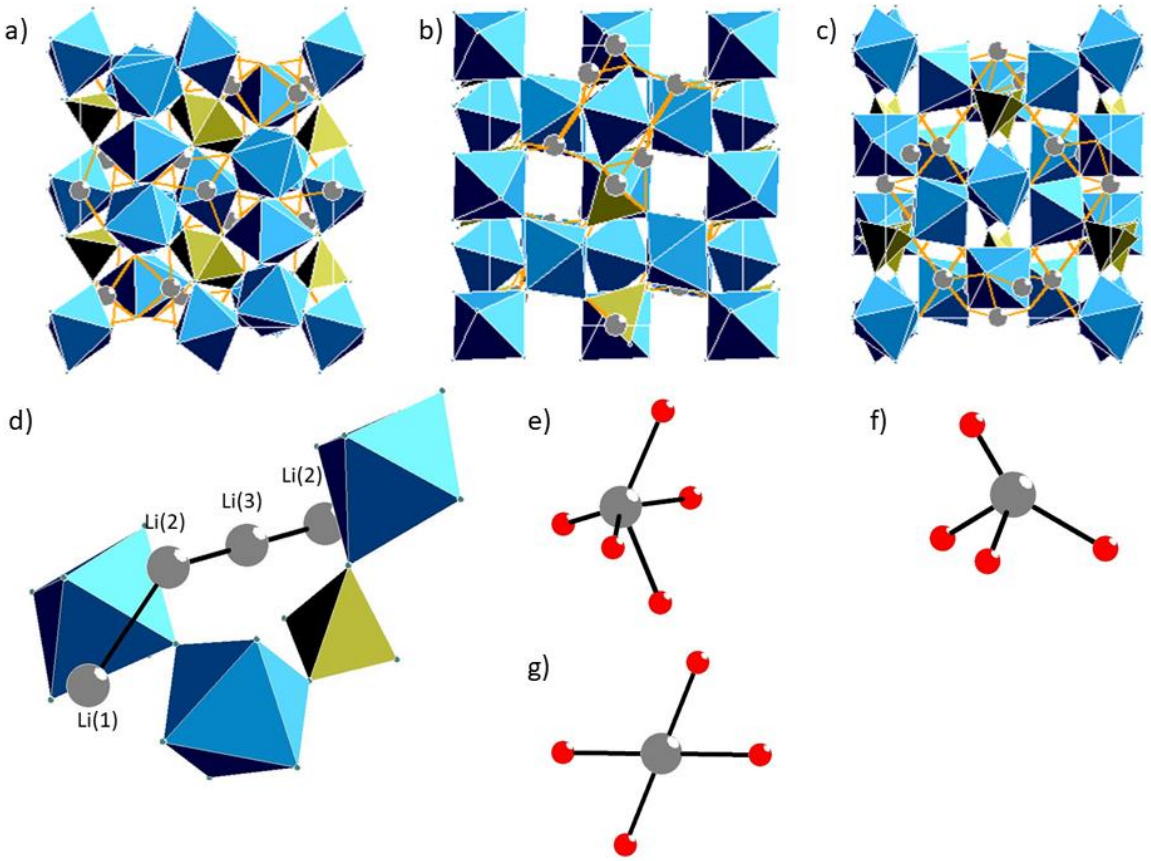

Figure 3.216: Structure of $LiTa_2PO_8$ generated using data obtained via Rietveld refinement against room temperature x-ray diffraction data. a) view along the a-axis, b) view along the b-axis, c) view along the c-axis, d) Partial Li-connectivity e) Li1 site, f) Li2 site, g) Li3 site.

Small amounts of doping is possible and the results for all doped samples indicate that the solubility limit for $LiTa_{2-x}M_xPO_8$ [*M*= Nb, Sb and Zr] doping is ~ x=0.1, after which impurities begin to form and changes in the unit cell parameters cease. Comparing all three doped samples at x=0.1 $LiTa_{2-x}Nb_xPO_8$ increases in volume and size, $LiTa_{2-x}Sb_xPO_8$ decreases in volume and size and $Li_{1+x}Ta_{2-x}Zr_xPO_8$ remains almost constant with respect to pristine $LiTa_2PO_8$. This is unusual due to the difference in atomic radii, with Zr being the largest, Nb being the same and Sb being the smallest, the trend observed indicates that the incorporation of dopants must lead to small structural changes occurring within the unit cell.

SEM images captured of $LiTa_{2-x}M_xPO_8$ [M=Nb, x=0,0.04, 0.1 and 0.2] show large voids between the grains of the pellets indicating a low density for these pellets. The EDX

mapping across all samples shows a homogeneous distribution of elements with inhomogeneity matching impurities of $LiTa_3O_8$ and Ta_2O_5 (phosphorus deficient areas), $LiOH/LiCO_3$ (Na and O rich areas) and Nb_9PO_{25} (Nb rich areas). The inhomogeneity decreases with increasing Nb content with Nb rich areas beginning to show when x=01, this confirms that the likely solubility limit for $LiTa_2PO_8$ doping is x~0.1.

Electrochemical properties of $LiTa_2PO_8$ with doping: The published bulk conductivity of $LiTa_2PO_8$ is reported to be 1.6×10^{-3} S cm^{-1} at 298K which is an order of magnitude higher than the sample synthesised in this study. [3] The relative density of the measured $LiTa_2PO_8$ sample is calculated to be~63%, which is lower than the reported sample indicating the density, hence microstructure of the material, is important to consider for enhanced Li^+ conductivity. SEM also shows large voids between the grains of all samples measured confirming a decrease in density of the pellets used for EIS conductivity measurements. The low density is also highlighted by the increase in activation energy of the parent compound (0.35(1) eV) in comparison to the published activation energy of 0.32 eV. [3] However, the intrinsic activation energy of the material calculated through SSNMR is calculated to be 0.23(1) eV, the lowest of those measured and approaching 0.16 eV, calculated in the literature using AIMD.[119] The conductivity and activation energies calculated for all samples are in the range of newly reported doped-electrolyte structures. [129, 60]

Figure 3.22 shows the impact of doping x=0.04 M^{5+} transition metals into the LiTa2*M*xPO8 structure, a clear difference is observed in the bulk conductivity. The highest bulk conductivity is calculated for $LiTa_{2-x}Sb_xPO_8$ with the lowest reported for $LiTa_{2-x}Nb_xPO_8$, both of which are an order of magnitude lower than that of the published structure. Interestingly, the activation energies calculated via EIS of the doped structures obey the same trend, which is unexpected, as an increase in conductivity is often associated with a lower activation energy for Li^+ hopping. This suggests doping may change the mechanism of local Li^+ hopping which is likely the result of small structural changes occurring within the lattice. This expected trend in conductivity and activation energy is observed for the intrinsic conductivity calculated via SSNMR spectroscopy (**Figure 3.23**) where an increase in activation energy for Nb doping is matched to the lower ionic conductivity observed in the EIS data. The increase in ionic conductivity calculated via EIS of $LiTa_{2-x}Sb_xPO_8$ as well as a

comparable intrinsic activation energy in comparison to $LiTa_2PO_8$ is encouraging, and modifying the microstructure combined with increasing the density of the sample in line with that of the published structure could yield a further increase in ionic conductivity.

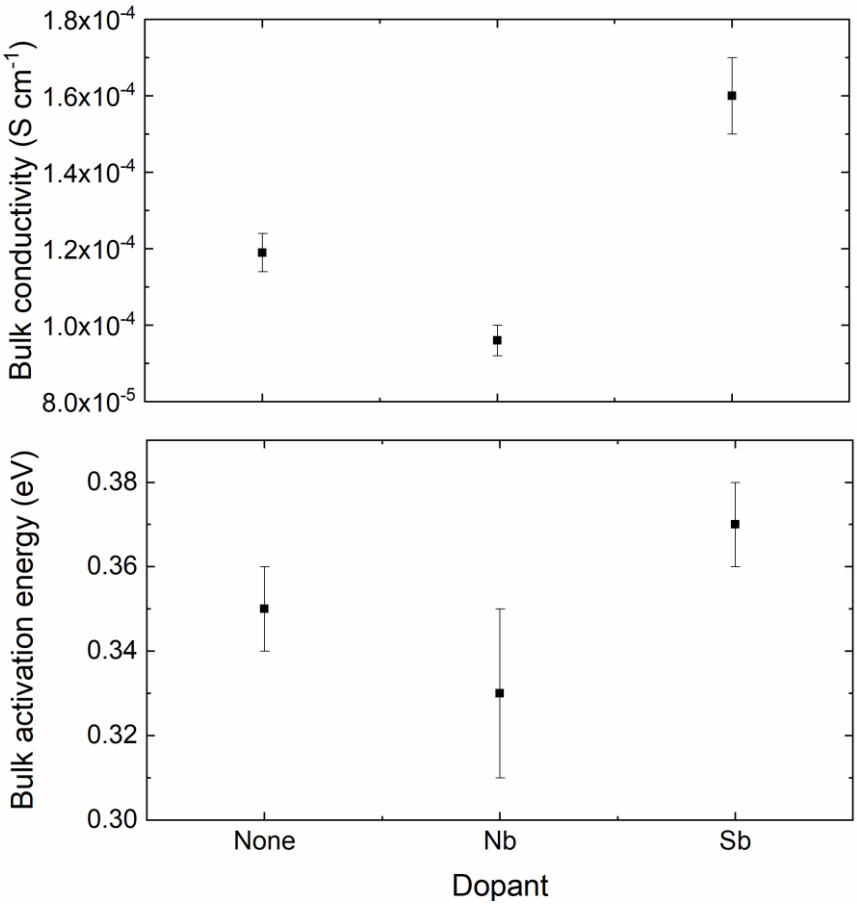

Figure 3.22: Bulk ionic conductivity and activation energy comparison for each dopant (M) at x=0.04 in $LiTa_{2-x}M_xPO_8$ at 293 K.

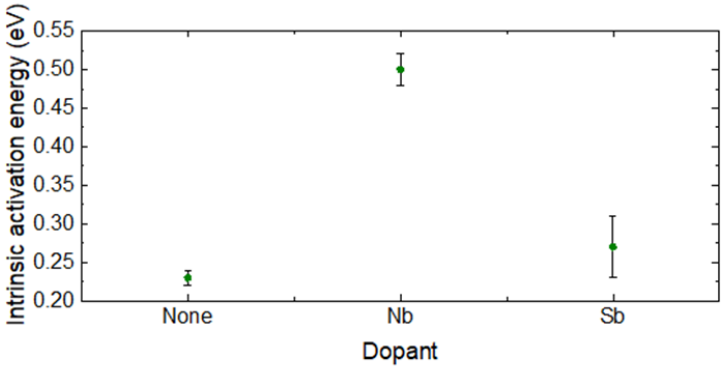

Figure 3.23: SSNMR calculated activation energies for each dopant (M) at x=0.04 in $LiTa_{2-x}M_xPO_8$ at 293 K

3.5 Conclusions

The synthesis procedure for $LiTa_2PO_8$ is easily reproducible and the structure can incorporate small amounts of dopants with the solubility of $LiTa_{2-x}M_xPO_8$ [*M*= Nb, Sb and Zr] being x~0.1, after which impurities begin to form. Attempts to synthesis other family members were not successful suggesting tantalum is required to stabilise the structure. The trend in lattice parameter change with dopant ionic radii is unusual, where lattice parameters for $LiTa_{2-x}Nb_xPO_8$ increase with increasing x and lattice parameters for $LiTa_{2-x}Zr_xPO_8$ remain almost constant. However, the lattice parameters decrease with increasing x for $LiTa_{2-x}Sb_xPO_8$ which is expected due to the smaller size of the ion. The uncommon trend observed for $LiTa_{2-x}M_xPO_8$ [*M*= Nb and Zr] samples is likely due to small structural changes which occur when small amounts of the respective ions are incorporated.

An electrochemical investigation revealed the highest bulk ionic conductivity was observed for the $LiTa_{1.96}Sb_{0.04}PO_8$ sample, calculated to be 1.6(1) x 10^{-4} S cm^{-1}, an order of magnitude lower than that published for $LiTa_2PO_8$, 1.6 x 10^{-3} S cm^{-1}. However, it should be noted that the relative density is likely lower than that of the published parent material and similar to that of the synthesised $LiTa_2PO_8$ sample (~63%). Further research into the densification of the sample and investigation of the microstructure could lead to a further increase in conductivity. Overall, the most promising sample in terms of potential doping and conductivity is that of $LiTa_{2-x}Sb_xPO_8$, the trend in lattice parameters follows what is expected with ionic radii size and the conductivity is improved, this indicates future dopants and family members could be synthesised and investigated for use as a solid electrolyte within a solid state battery.

CHAPTER 4: LI-ION TRANSPORT PROPERTIES IN $LI_3FE(MOO_4)_3$

4.1 Introduction

The NASICON-type structure has the general formula $NaM_2(PO_4)_3$ which can be modified to include Li such as $LiZr_2(PO_4)_3$ [47] (LZP) and Al-doped $LiTi_2(PO_4)_3$ [130] (LATP). These types of structures are considered fast Li-ion conductors and are most commonly used as electrolytes as they show reported high room temperature ionic conductivities of 1 x 10^{-4} S cm^{-1} [48] (LZP) , and for Al-stabilized LATP, ~1 x 10^{-3} S cm^{-}

[1] [131]. Replacing the transition metal ion with a reducible element such as Fe and V, can yield materials which can reversibly insert/extract Li ions for use as a cathode within a cell, whilst potentially maintaining the ionic properties of a fast ionic conductor. Examples include materials such as $Fe_2(MoO_4)_3$, $Fe_2(WO_4)_3$, $Li_3Fe(MoO_4)_3$, $Li_3V(MoO_4)_3$, $Li_3Cr(MoO_4)_3$, $Li_2Ni_2(MoO_4)_3$.[132, 133, 134, 135, 136, 137] The ionic conductivity of redox active NASICON structures is not usually researched in the literature as more attention is paid to solid electrolyte structures, however fully understanding the mechanism of Li-ion transport can aid in the assembly of all solid-state batteries. Utilizing lattice matching across the solid electrolyte/cathode interface, is emerging within the literature and it is theorized that this can aid in reducing the overall interfacial resistance across an ASSB, by reducing the resistance across the electrolyte/ electrode interface. [138, 96]

The molybdate structure, $Li_3M(MoO_4)_3$, crystallizes with space group Pnma (62) and has been studied previously using x-ray diffraction. The structures reportedly consist of MoO_4 tetrahedra and mixed MO_6/LiO_6 polyhedra (where M= Cr, Fe, Mg, V, Ni, Ti, Al). [139, 4, 140, 141, 142, 143] Typically, There are two mixed metal/lithium sites within the structures, M1 and M2, with the M3 sites occupied fully and exclusively by lithium (**Figure 4.1)**. [4, 144, 143, 142] The lithium distribution within these structures has been assumed based on single crystal studies with only one neutron diffraction study performed. [143] $Li_3Fe(MoO_4)_3$ has been reinvestigated for its Li-ion transport properties to aid in the understanding of its ability to perform as a cathode within a ASSB, it is also isostructural with $Li_3Cr(MoO_4)_3$ but replaces Cr with more earth abundant Fe. Understanding the lithium distribution and transport properties within $Li_3Fe(MoO_4)_3$ is key in understanding the electrochemical behavior produced by these molybdate NASICON materials, when used as a cathode within an ASSB.

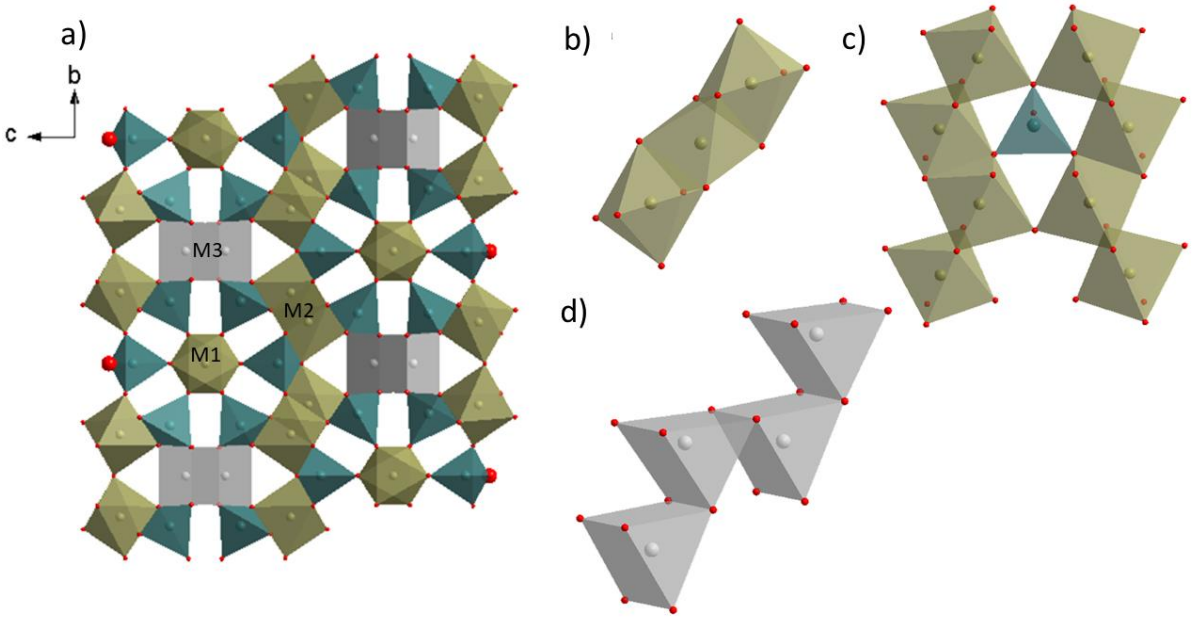

Figure 4.1: Crystal structure of $Li_3M^{3+}(MoO_4)_3$ a) View along the a-axis of the unit cell showing MoO_4 tetrahedra in blue, $Li/M^{3+}O_4$ polyhedra in green, and Li pristmatic sites in grey, b) Connectivity of the M1 sites along the a-axis, c) Connectivity of the M2 sites along the a axis and d) connectivity of the M3 sites along the a-axis.

4.2 Experimental

Synthesis: $Li_3Fe(MoO_4)_3$ is synthesised via a conventional solid-state reaction using Li_2CO_3, $(NH_4)_6Mo_7O_{24}.4H_2O$ and Fe_2O_3 as starting materials. A stoichiometric mixture of the starting materials was ground using a pestle and mortar for 30 minutes, then heated at 550 ^oC for 12 hours in a muffle furnace. The resultant powder was then reground and pressed into a pellet and finally calcined at 600 ^oC for 6 hours. The pellet was then either reground for structural characterisation, or directly used for conductivity measurements.

Structural characterisation: X-ray powder diffraction (XRD) data were collected at room temperature using a Miniflex Rigaku diffractometer in the reflection mode, employing Cu Kα radiation (λ=1.5406 Å). Neutron powder diffraction (NPD) data were collected at 150 K, 300 K and 450 K on the HRPD [145] instrument at the ISIS neutron and muon source. In the NPD experiment, samples were sealed between two vanadium plates and data were corrected for absorption using an in house method.

Rietveld refinement was performed against the powder diffraction data from banks 1 (168.33^{o} 2θ) and 2 (89.58^{o} 2θ) using the GSAS suite of programs, [107] employing a pseudo-Voigt peak shape and a shifted Chebyschev background function.

Electrochemical characterisation: Electrochemical impedance spectroscopy and DC polarization studies were performed on thin pellets of $Li_3Fe(MoO_4)$ (~1.1 mm thick and 10 mm in diameter) using Au electrodes. Au electrodes were sputter coated onto both sides of the pellet using a sputter coater. The sputtering time was 200 s, using 20 mA sputtering current and an Ar pressure of ~0.02 mbar. The pellets were loaded in Swagelok cells in an Ar-filled glovebox, where impedance/DC polarisation data were collected using stainless steel current collectors under Ar atmosphere. Impedance data were recorded in the temperature range 303-373 K using a BioLogic VMP-300 potentiostat in the frequency range of 5 MHz to 1 Hz with an electrical perturbation of 40 mV. DC polarisation tests were conducted at 0.5 V intervals between 1 and 2 V and Ohm's law was used to calculate the resistance.

Computational studies (Performed in collaboration with Liverpool university: Calculations performed by Dr. Elvis Shoko and Dr. Matthew Dyer with the following information given): "The ab initio molecular dynamics (AIMD) simulation was performed in the Vienna ab initio Simulation Package (VASP) [17] employing the projector augmented-wave method.[18] For the exchange-correlation potential, the generalized gradient approximation with the Perdew, Burke, and Ernzerhof functional[19] incorporating the rotationally invariant implementation[20] of the Hubbard-U framework (PBE + U) was adopted, with U = 5.3 eV for Fe. Spin-polarised calculations with antiferromagnetic ordering of the Fe^{3+} ions were used throughout. The employed supercell was first optimized for lattice parameters with total forces per atom converged to ≤ 0.02 eV/Å, using a plane wave energy cut-off of 600 eV and Γ-point sampling. The AIMD simulation was then run at 500 K, employing the simple velocity scaling approximation to the canonical ensemble (NVT) with a plane wave energy cut-off of 600 eV, Γ-point sampling of the Brillouin zone, and a time step of 1 fs. The system was allowed to thermally equilibrate for 3 ps, followed by a production run of 35 ps. The relatively short production run and simple velocity scaling scheme employed for temperature control are expected to accurately model the Li^{+} inter-site hopping, but are not suitable for simulating longer range Li diffusion."

4.3 Results

Phase purity of $Li_3Fe(MoO_4)_3$ was first tested via XRD and a small amount (~5% wt. fraction) of $Li_2(MoO_4)_3$ was found. The sample was then used to perform NPD experiments where the lithium distribution was revealed. Refinement against the room temperature neutron diffraction data showed that the stoichiometry of the compound is actually $Li_{2.775}Fe_{1.075}(MoO_4)_3$, this was accepted as it charge balances the structure with an iron oxidation state of 3^+. This slight enrichment of Fe is consistent with the overall target stoichiometry of the sample. Due to the 5 % wt. fraction of impurity phase, Li_2MoO_4, the molar amount of Mo and Fe in the total product, $Li_{2.775}Fe_{1.075}(MoO_4)_3$, gives an error of 1.73 $x10^{-5}$ and 2.69 $x10^{-4}$ respectively compared to that of the starting materials; within error of the balance used in weighing of the starting materials. Instability in the refinement was discovered when trying to refine the fractional occupancy, thermal isotropic displacement parameter and coordinates of the M2 site, this instability led to a negative Uiso of -0.001(2). To solve this, the Uiso was fixed at a value of 0.0001 and the fractional occupancies and coordinates were refined. The stoichiometry was accepted and then constrained in the low temperature and high temperature data as to ensure a mass balance across all temperatures.

The refinement shown in **Figure 4.2** yielded a GOF value 2.07 and R_w value of 2.296 close the required values of 1 and 0. The calculated lattice parameters are *a*= 5.08986(4) Å, *b*= 10.45048(9) Å and *c*= 17.5266(1) Å with a total unit cell volume of 932.26(2) $Å^3$, slightly smaller than that of the reported structure (*a*= 5.07 Å, *b*= 10.48 Å, *c*= 17.64 Å, V= 937.28 $Å^{-3}$) [4]. The refinement also indicated vacancies on the M1 and M3 sites (**Table 4.1**), leading to a vacancy distribution of 0.117 and 0.07 on the M1 and M3 site respectively. This is not expected as the reported structure shows fully occupied lithium and iron sites.

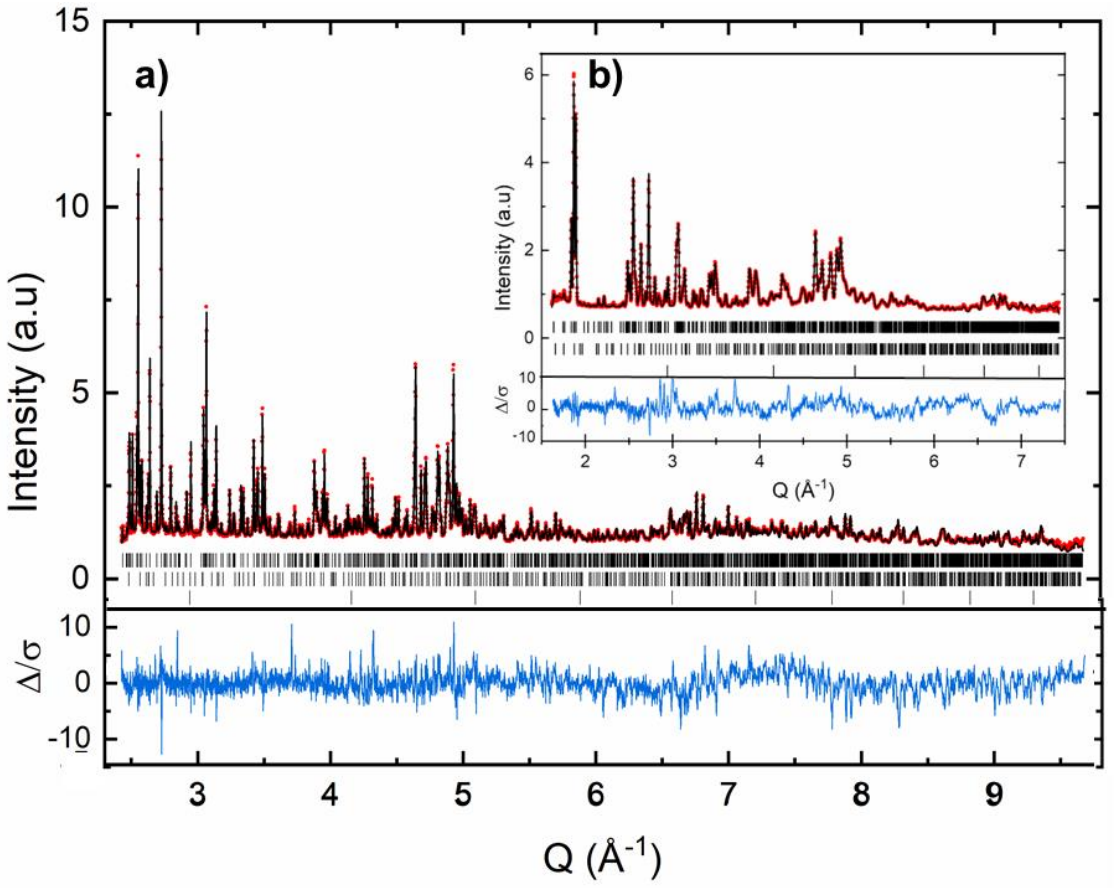

Figure 4.2: Neutron diffraction data (detector bank 1) collected at 300 K for $Li_{2.775}Fe_{1.075}(MoO_4)_3$ (inset shows detector bank 2). Observed data shown with red circles, calculated data in black and Δ/σ in blue. Vertical tick marks are shown below for allowed Bragg reflections for $Li_3Fe(MoO_4)_3$ (upper), Li_2MoO_4 (middle) and V (lower).

Table 4.5: Calculated atomic position parameters for $Li_{2.775}Fe_{1.075}(MoO_4)_3$ at 300 K, calculated using neutron diffraction data bank 1 and bank 2.

Atom	Type	Site	X	Y	Z	Fractional occupancy	Uiso ($Å^2$)
Mo(1)	Mo6+	8 d	0.27837(23)	0.52555(10)	0.15622(8)	1	0.0008(3)
Mo(2)	Mo6+	4 c	0.7765(3)	0.25	0.05712(9)	1	0.0006(4)
Fe/Li(1)	Fe3+	4 c	0.1099(7)	0.25	0.25006(24)	0.434(2)/ 0.449(9)	0.0117(14)
Fe/Li(2)	Fe3+	8 d	0.7574(11)	0.5660(5)	0.0229(3)	0.3186(9)/ 0.689(4)	0.0001

Li(3)	Li1+	4 c	0.2450(12)	0.75	0.3032(3)	0.93(22)	0.0088(24)
O(1)	O2-	4 c	0.8617(4)	0.25	0.15588(13)	1	0.0072(5)
O(2)	O2-	4 c	0.0574(4)	0.25	-0.00613(13)	1	0.0129(6)
O(3)	O2-	8 d	0.5806(3)	0.11590(16)	0.03736(10)	1	0.0092(4)
O(4)	O2-	8 d	0.08062(30)	0.48864(15)	0.07499(9)	1	0.0089(4)
O(5)	O2-	8 d	0.08070(31)	0.62253(14)	0.21316(10)	1	0.0118(4)
O(6)	O2-	8 d	0.35572(27)	0.38054(15)	0.20552(10)	1	0.0060(4)
O(7)	O2-	8 d	0.5602(3)	0.61217(15)	0.12565(10)	1	0.0118(4)

A similar instability occurred in the low temperature data where the two Mo sites refined with negative Uiso's of -0.002(3) and -0.002(5) respectively, these were then fixed at 0.001. A similar process was done with the Li in the M3 site with a calculated Uiso of -0.0013(20) it was fixed at 0.001. A good fit was achieved (**Figure 4.3**), the refinement yielded a GOF value of 2.69 and R_w value of 3.019 which is slightly higher than that of the room temperature data, however, the low temperature data has fewer degrees of freedom due to the charge balancing of the structure. The refined lattice parameters of *a*=5.07677(5) Å, *b*=10.438(1) Å and *c*=17.4938(2) Å with a unit cell volume of 926.39(2) $Å^3$, are smaller than that calculated for the room temperature data indicating that the unit cell has decreased in size ($\Delta a \sim 8.7 \times 10^{-5}\ K^{-1}$, $\Delta b \sim 8.3 \times 10^{-5}\ K^{-1}$ and $\Delta c \sim 2.2 \times 10^{-5}\ K^{-1}$) with respect to the room temperature data as expected, due to a lower temperature. The lithium distribution has also changed with temperature shown in **Table 4.2**; the M1 site increasing in vacancies to 0.146 and M3 site vacancies decreasing to 0.02.

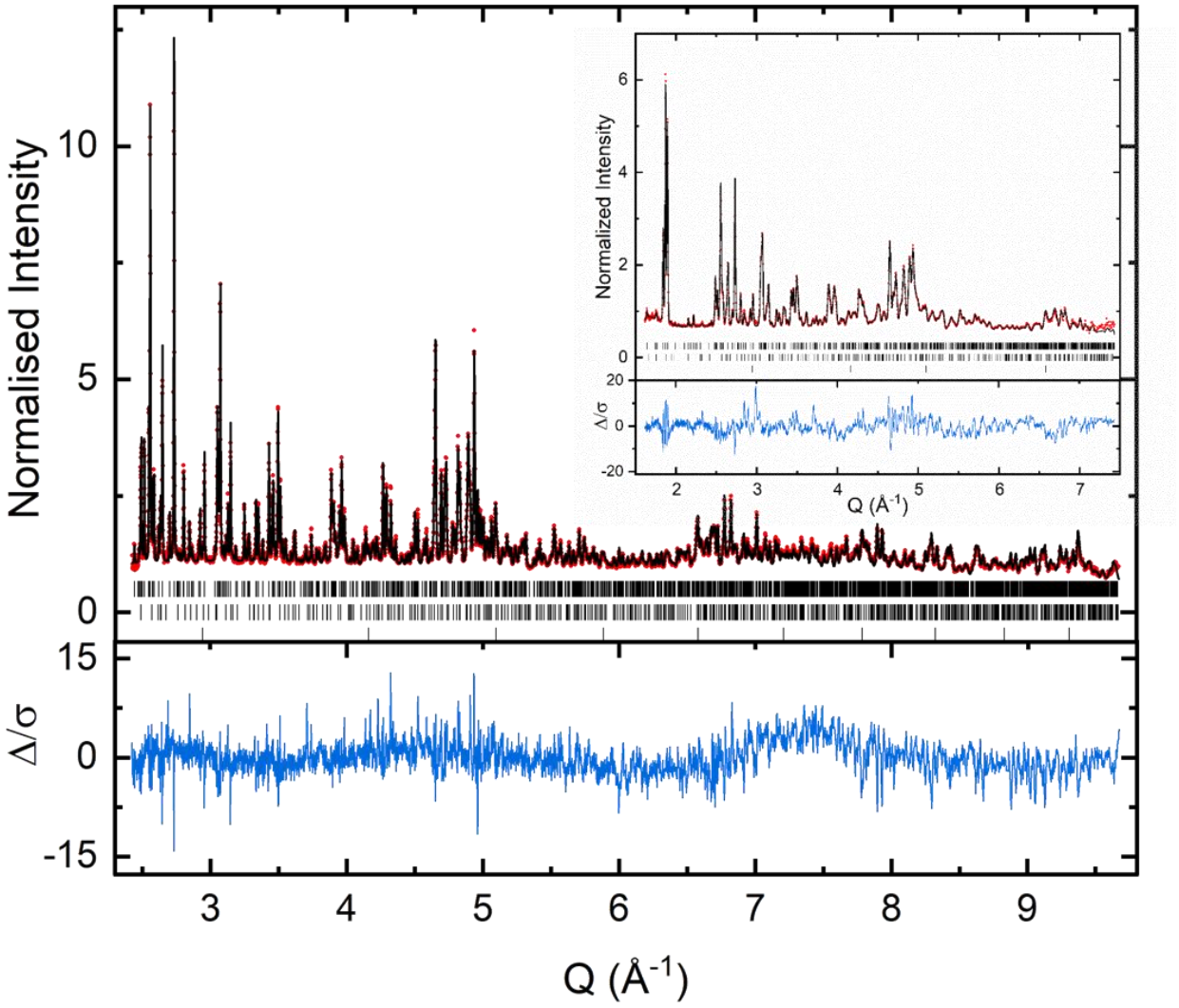

Figure 4.3: Neutron diffraction data (detector bank 1) collected at 150 K for $Li_{2.775}Fe_{1.075}(MoO_4)_3$ (inset shows detector bank 2). Observed data shown with red circles, calculated data in black and Δ/σ in blue. Vertical tick marks are shown below for allowed Bragg reflections for $Li_3Fe(MoO_4)_3$ (upper), Li_2MoO_4 (middle) and V (lower).

Table 4.6: Calculated atomic position parameters for Low temperature (150 K) $Li_{2.775}Fe_{1.075}(MoO_4)_3$, calculated using neutron diffraction data bank 1 and bank 2.

Atom	Type	Site	X	Y	Z	Fractional occupancy	Uiso ($Å^2$)
Mo(1)	Mo6+	8 d	0.27792(28)	0.52569(12)	0.15605(9)	1	0.001
Mo(2)	Mo6+	4 c	0.7775(4)	0.25	0.05682(12)	1	0.001
Fe/Li(1)	Fe3+	4 c	0.1107(9)	0.25	0.25006(28)	0.434(2)/ 0.42(1)	0.0118(15)
Fe/Li(2)	Fe3+	8 d	0.7571(14)	0.5665(6)	0.0225(4)	0.320(1)/0.684(6)	0.0055(18)
Li(3)	Li1+	4 c	0.2448(13)	0.75	0.3032(3)	0.98(1)	0.001
O(1)	O2-	4 c	0.8632(5)	0.25	0.15595(15)	1	0.0044(6)
O(2)	O2-	4 c	0.0591(5)	0.25	-0.00656(15)	1	0.0069(6)
O(3)	O2-	8 d	0.5800(4)	0.11571(19)	0.03712(11)	1	0.0050(4)
O(4)	O2-	8 d	0.0783(3)	0.48793(16)	0.07468(11)	1	0.0026(4)
O(5)	O2-	8 d	0.0791(4)	0.62219(16)	0.21340(11)	1	0.0047(4)
O(6)	O2-	8 d	0.35754(31)	0.38076(17)	0.20548(12)	1	0.0022(4)
O(7)	O2-	8 d	0.5605(4)	0.61260(17)	0.12569(12)	1	0.0074(4)

The high temperature refinement produced no instabilities in the displacement parameters likely due to the fact atoms now have more thermal energy due to the higher temperature and hence give rise to a more clearly defined scattering volume, hence all atoms were free to move. The refinement shown in **Figure 4.4** yielded a GOF value of 1.34 and R_w value of 2.648. The calculated lattice parameters were found to be *a*=5.10756(7) Å, *b*=10.4804(1) Å and *c*= 17.5772(2) Å with a unit cell volume of 940.90(3) $Å^3$, as expected the unit cell has increased in size ($\Delta a \sim 1.2 \times 10^{-4}$

K^{-1}, Δ*b*~ 2.0 x 10^{-4} K^{-1} and Δ*c*~ 3.4 x 10^{-4} K^{-1}) with temperature. The lithium distribution, shown in **Table 4.3** also differed to that of the low and room temperature data with the M1 site decreasing in vacancies to 0.08 and the M3 site vacancies increasing to 0.09, with respect to the room temperature data.

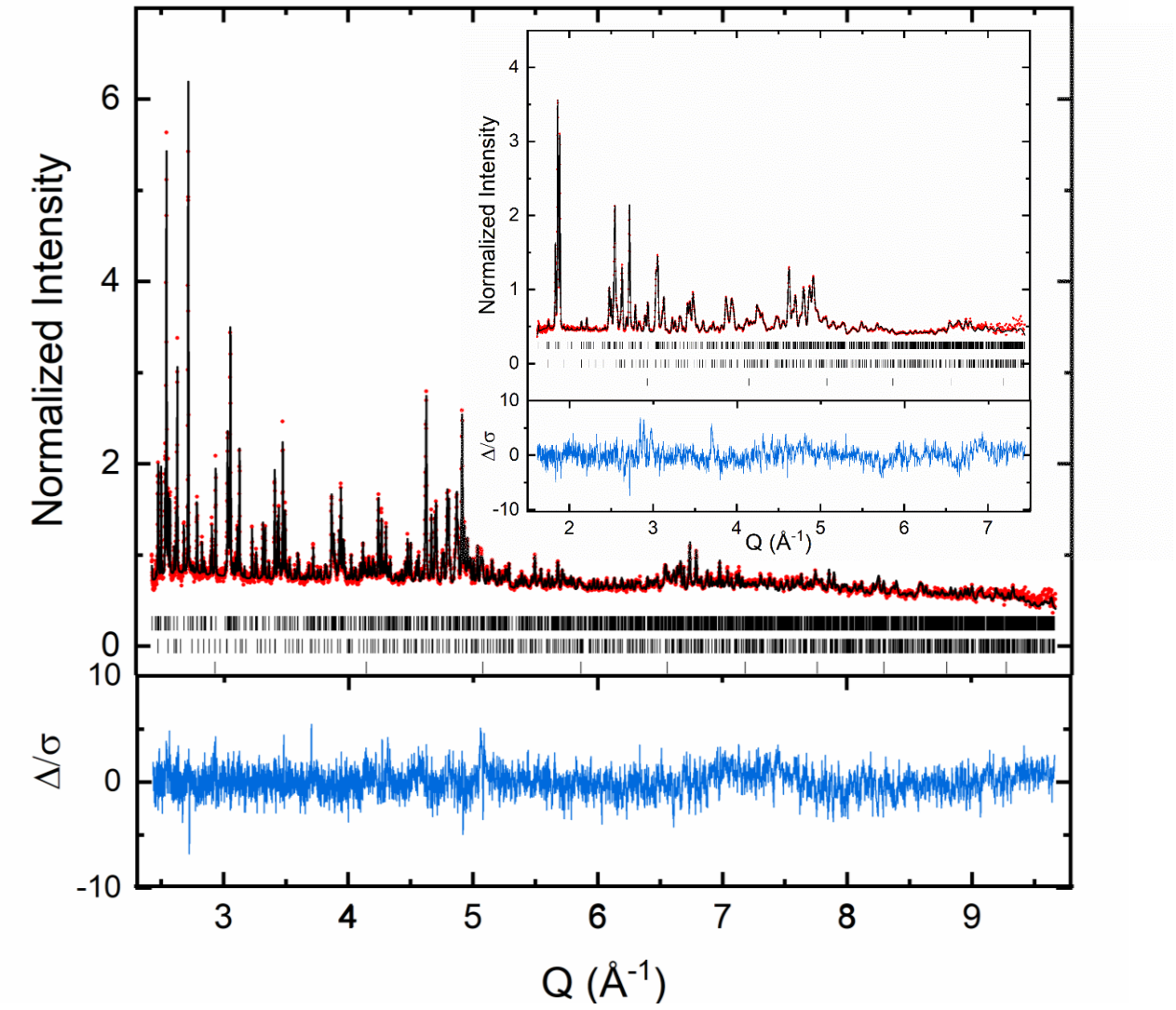

Figure 4.4: Neutron diffraction data (detector bank 1) collected at 450 K for $Li_{2.775}Fe_{1.075}(MoO_4)_3$ (inset shows detector bank 2). Observed data shown with red circles, calculated data in black and Δ/σ in blue. Vertical tick marks are shown below for allowed Bragg reflections for $Li_3Fe(MoO_4)_3$ (upper), Li_2MoO_4 (middle) and V (lower).

Table 4.7: Calculated atomic position parameters for High temperature (450 K) $Li_{2.775}Fe_{1.075}(MoO_4)_3$, calculated using neutron diffraction data bank 1 and bank 2.

Atom	Type	Site	x	y	Z	Fractional occupancy	Uiso ($Å^2$)
Mo(1)	Mo6+	8 d	0.2775(3)	0.52576(15)	0.15529(11)	1	0.0048(5)
Mo(2)	Mo6+	4 c	0.7758(4)	0.25	0.05719(13)	1	0.0052(6)
Fe/Li(1)	Fe3+	4 c	0.1089(10)	0.25	0.25068(31)	0.417(2)/ 0.52(1)	0.0080(19)
Fe/Li(2)	Fe3+	8 d	0.7629(14)	0.5660(6)	0.0215(5)	0.329(1)/ 0.67(1)	0.0248(23)
Li(3)	Li1+	4 c	0.2420(18)	0.75	0.3022(5)	0.91(3)	0.001(3)
O(1)	O2-	4 c	0.8572(6)	0.25	0.15513(18)	1	0.0145(8)
O(2)	O2-	4 c	0.0548(6)	0.25	-0.00599(17)	1	0.0155(9)
O(3)	O2-	8 d	0.5811(5)	0.11578(22)	0.03719(13)	1	0.0118(6)
O(4)	O2-	8 d	0.0809(4)	0.48937(21)	0.07415(13)	1	0.0143(6)
O(5)	O2-	8 d	0.0814(4)	0.62396(20)	0.21241(13)	1	0.0187(6)
O(6)	O2-	8 d	0.3537(4)	0.38076(21)	0.20528(15)	1	0.0141(6)
O(7)	O2-	8 d	0.5591(5)	0.61104(21)	0.12566(15)	1	0.0189(6)

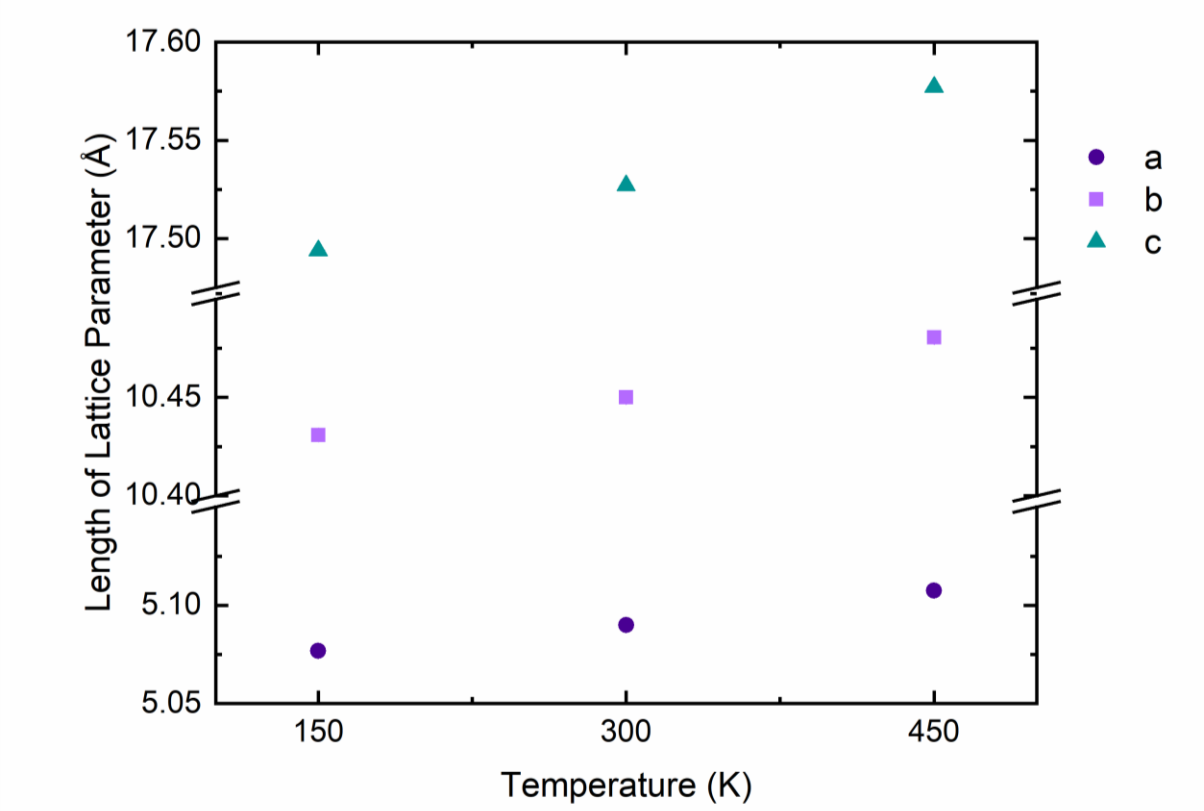

Figure 4.5: Lattice parameter changes for $Li_{2.775}Fe_{1.075}(MoO_4)_3$ with increasing temperature calculated from Rietveld refinements against neutron diffraction data. Errors are shown but are smaller than the marker.

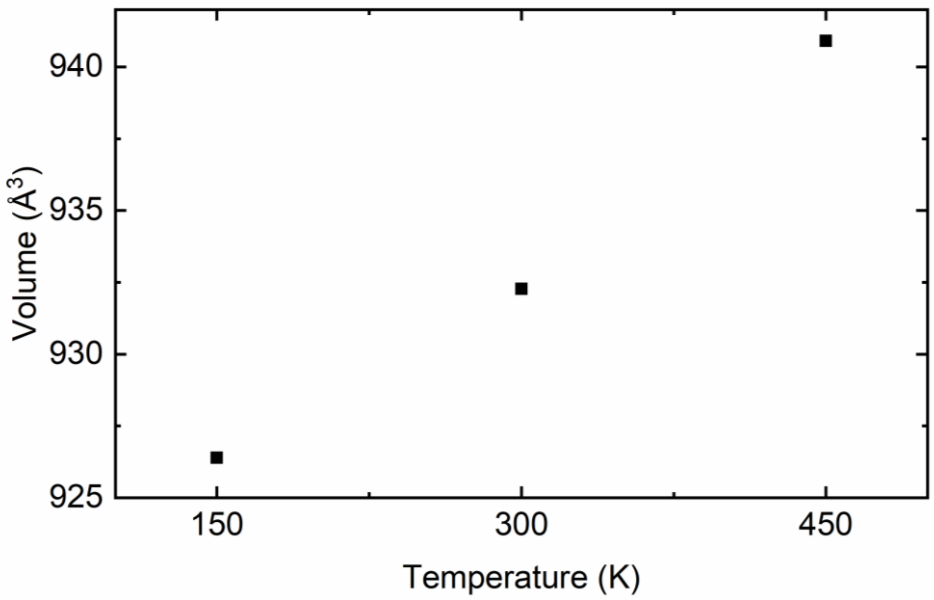

Figure 4.6: Graph showing the unit cell volume change upon increasing temperature calculated from neutron diffraction refinement for $Li_{2.775}Fe_{1.075}(MoO_4)_3$. Errors are shown but are smaller than the marker.

The lattice parameters and unit cell volume increase linearly with temperature, shown in **Figure 4.5** and **Figure 4.6**, which is expected for thermal expansion of the crystal lattice and indicates no clear structural changes occur over the temperature range measured.

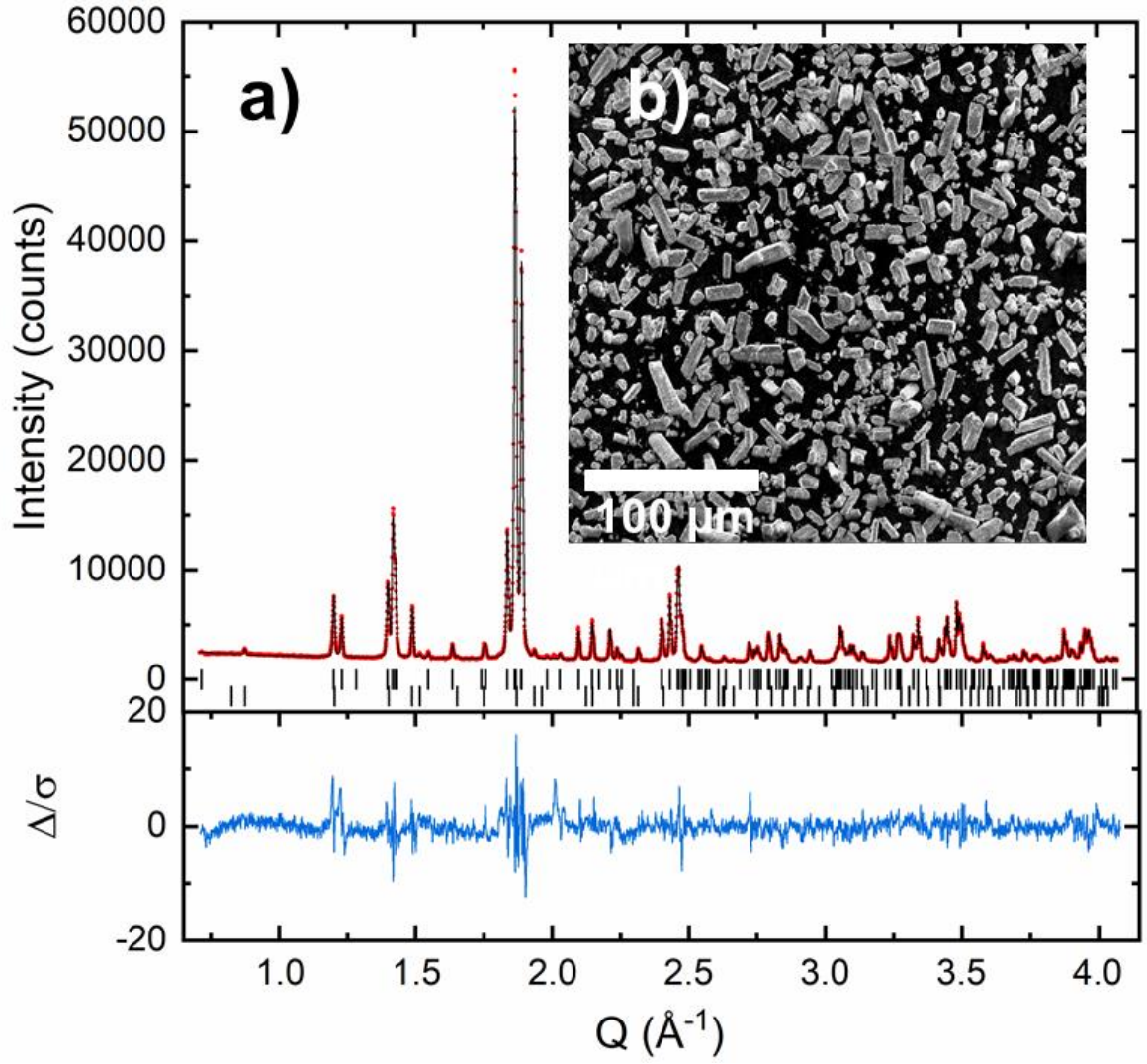

Figure 4.7: a) Rietveld refinement against powder x-ray data collected of $Li_{2.775}Fe_{1.075}(MoO_4)_3$ at room temperature. Observed data shown in red, calculated in black and Δ/σ in blue. Ticks show allowed Bragg reflections for $Li_3Fe(MoO_4)_3$ (upper) and Li_2MoO_4 (lower). B) Scanning electron microscopy image of powdered $Li_{2.775}Fe_{1.075}(MoO_4)_3$.

A refinement against the x-ray diffraction data using the published fractional occupancies [4] yielded a R_w value of 3.20 and GOF of 1.70, this was reduced to 3.18

and 1.67 respectively when including fractional occupancies calculated from the room temperature neutron diffraction refinement. The final x-ray powder diffraction refinement is shown in **Figure 4.7 a**). Instability occurred on the M3 site which produced a Uiso value of -0.03(1), this was then constrained to be 0.01. The SEM image taken of powdered $Li_{2.775}Fe_{1.075}(MoO_4)_3$ **(Figure 4.7 b))** shows the powder is made up of predominantly long particles of various sizes, and the largest ~50 μm.

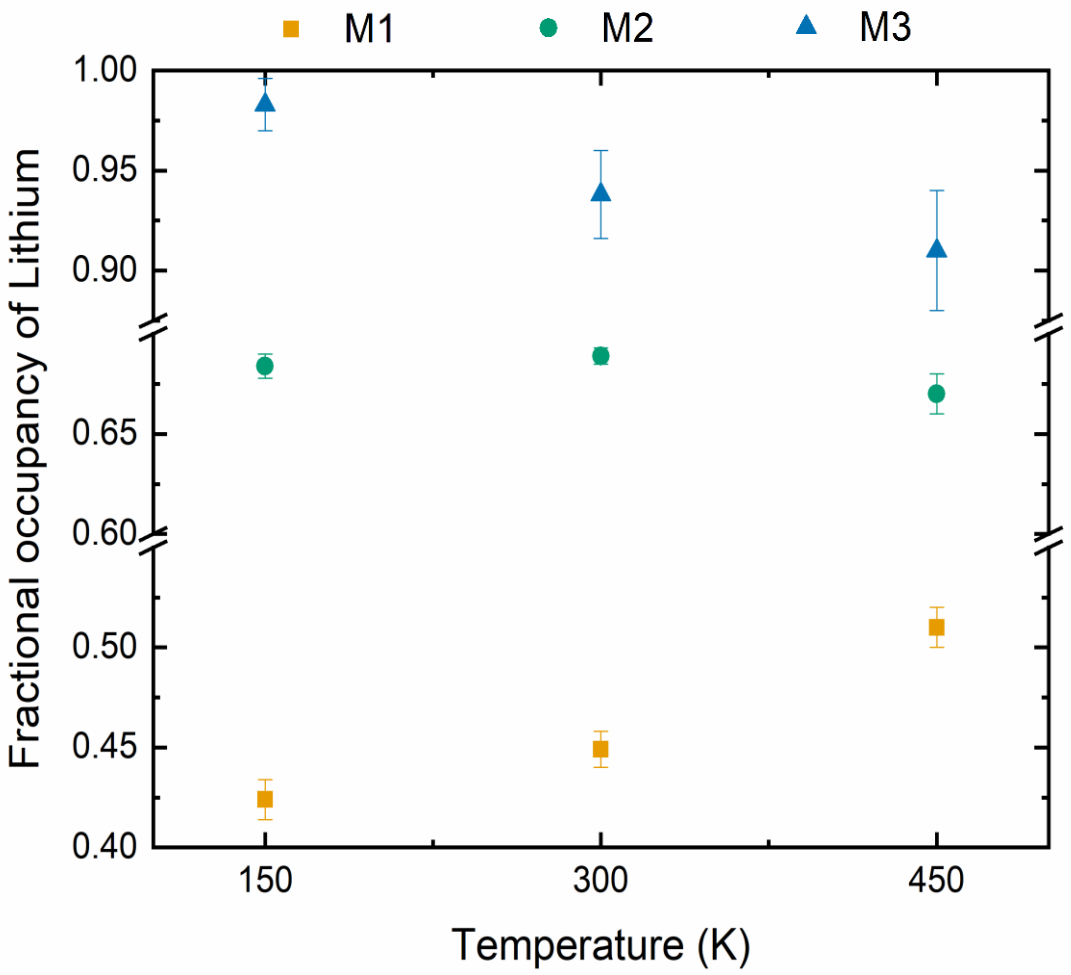

Figure 4.8: Graph showing the change in fractional occupancy of lithium with temperature on the M1, M2 and M3 sites for $Li_{2.775}Fe_{1.075}(MoO_4)_3$. calculated using neutron diffraction refinement data.

The Lithium occupancies of the M1, M2 and M3 sites varies with temperature (**Figure 4.8**). The Fe content on the M1 and M2 site at all temperatures remains constant, within error, so the vacancy distribution can be related to the variance in Li

occupancies across the sites. The M2 site shows no change in Li occupancy, within error, whereas the Li occupancy increases with temperature on the M1 site and decrease on the M3 site.

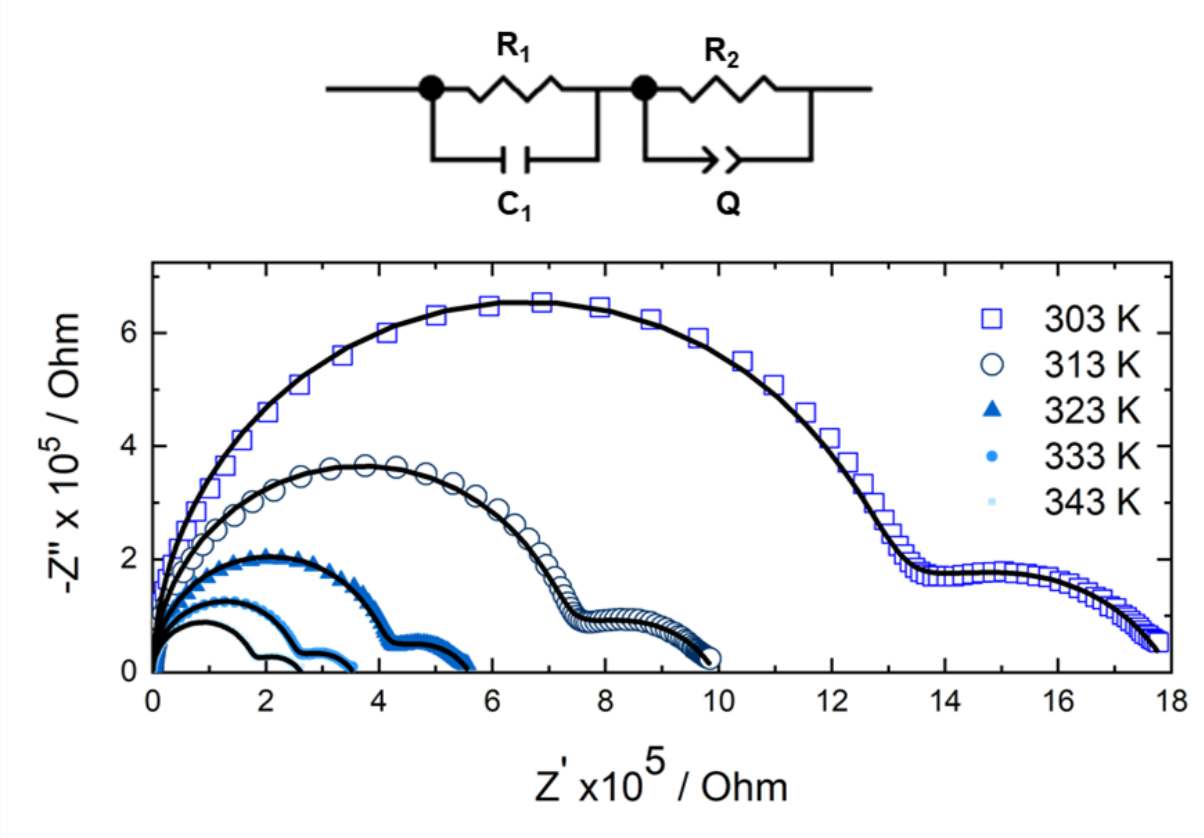

Figure 4.9: Nyquist plots showing impedance data collected from $Li_{2.775}Fe_{1.075}(MoO_4)_3$ at different temperatures, with the fit shown in black; the inset shows the equivalent circuit used to fit the impedance data.

Figure 4.9 shows the electrochemical impedance spectroscopy data obtained for $Li_{2.775}Fe_{1.075}(MoO_4)_3$ and shows two semi circles which were fitted with the equivalent circuit [R1C1][R2Q]. The first semicircle is attributed to the total response due to the calculated capacitance of ~4.3 x 10^{-11} F, typical of a bulk/grain boundary response. [150] The second semicircle, with a calculated capacitance of ~4.7 x 10^{-8} F, was assigned to the electrode (Au) interface. The first semicircle was fitted using a resistor and capacitor (R1 and C1 respectively), where R1 is the total resistance of the material, and C1 is the double layer capacitance of the material. The calculated value of R1 was then used to calculate the total ionic conductivity which was found to be 1.10(4) x 10^{-7} S cm $^{-1}$ at 303 K. The electrode interface conductivity contribution, attributed to the

second semicircle and fitted using a resistor (R2), was calculated to be 2.66(4) x 10^{-7} S cm^{-1} with a constant phase element, Q, use to model the inhomogeneity across the interface. The Li^+ transport activation energy calculated using the Arrhenius plot shown in **Figure 4.10** is 0.49(2) eV in the range 303 K- 343 K.

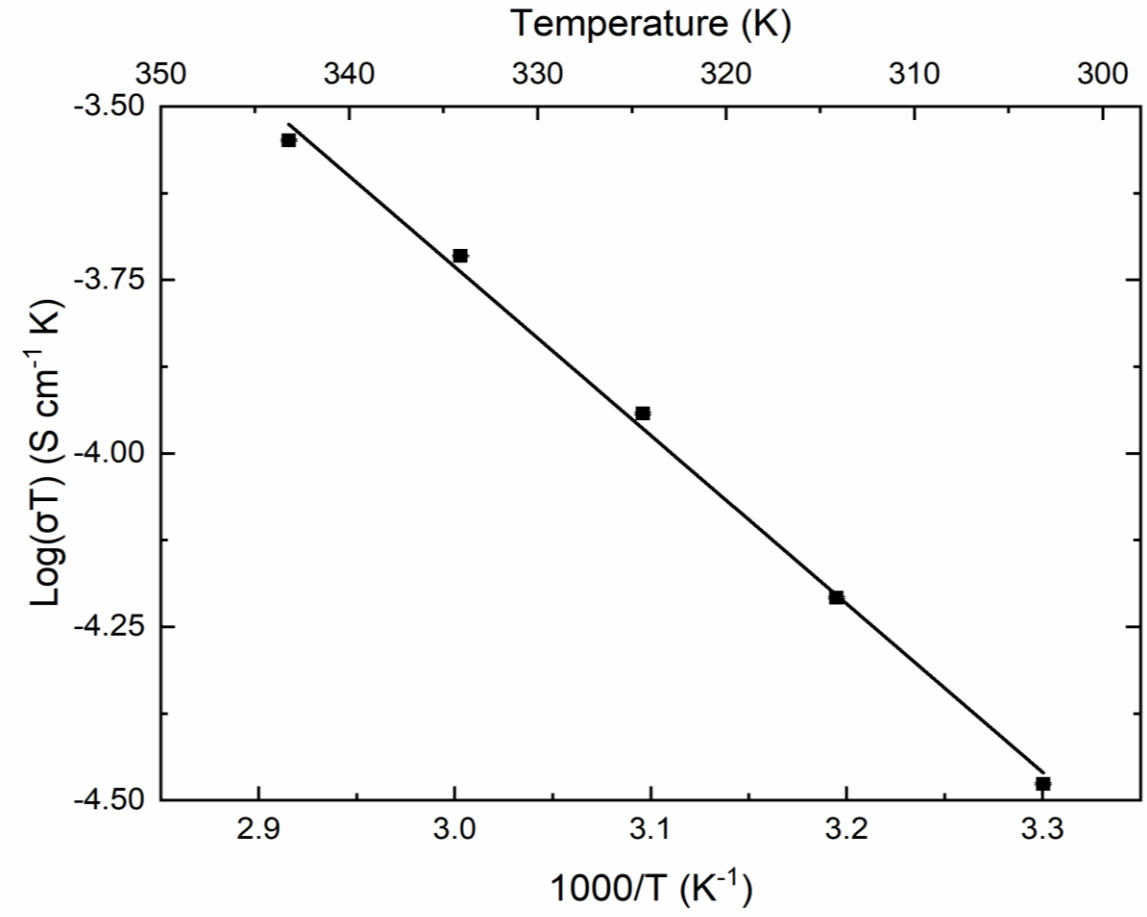

Figure 4.10: Arrhenius plot used to calculate the activation energy of Li^+ transport on $Li_{2.775}Fe_{1.075}(MoO_4)_3$ pellet. Errors are shown but are smaller than the marker.

DC polarization was used to estimate the electronic conductivity of the material **(Figure 4.11**) using Ohms law with a voltage of 1.5 V and a current of 4.60(3) x 10^5 mA, an electronic conductivity of 3.52(5) × 10^{-8} S cm^{-1} was calculated with Li transference number of 0.74. This result is consistent with recent studies,[151] confirming that $Li_3Fe(MoO_4)_3$ is a mixed ionic-electronic conductor. As the DC polarisation was repeated over multiple voltage steps the plateaued current begins to include a peak,

this peak in the data increases with each voltage suggesting the material is structurally unstable during lithium extraction and insertion.

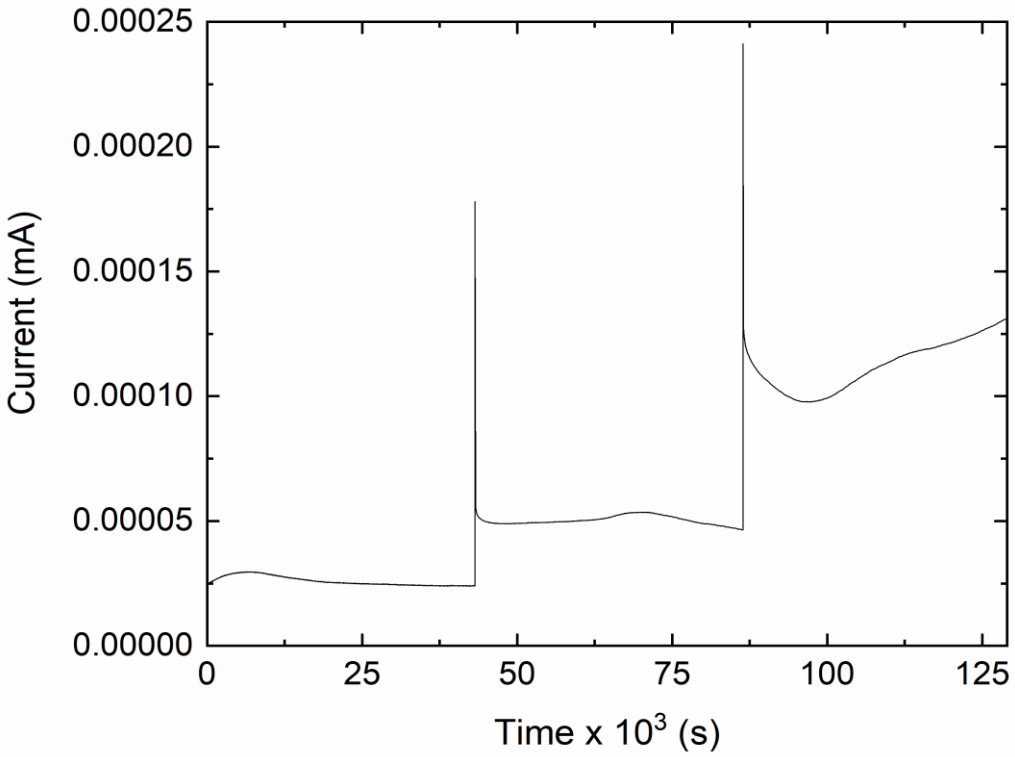

Figure 4.11: DC polarisation data collected at room temperature on a $Li_{2.775}Fe_{1.075}(MoO_4)_3$ pellet.

In order to further confirm Li-ion pathways in $Li_{2.775}Fe_{1.075}(MoO_4)_3$ AIMD simulations were performed over 35 ps at 500 K. **Figure 4.12 a-c** show the Li atom trajectories viewed along all three axes of the supercell. The trajectory traces show evidence of Li inter-site hopping; there are more and denser inter-site traces in both the ac and ab planes compared to the bc plane. The motion is predominantly within the M3 chains and along the a-axis, **Figure 4.12 a,b**. However, some occasional inter-site hopping events between M3 and M2 sites are observed, **Figure 4.12 c**, suggesting that inter-chain Li hopping also contributes to Li^+ ion motion. Local inter-site hopping occurs along the chain of M1 atoms, **Figure 4.12 a**, however the presence of Fe blocking Li^+ ion motion in these 1-dimensional pathways will prevent long-range transport along them. From the density plots of the root mean square displacements (RMSD) of the Li

atoms, **Figure 4.12 d**, significant density around 3.2 Å is observed for two Li atoms in the M3 chain. The Li atoms have neighbouring sites located around 3.15 Å in the crystal structure, suggesting that each of these atoms hops into the region of its neighbouring vacancy.

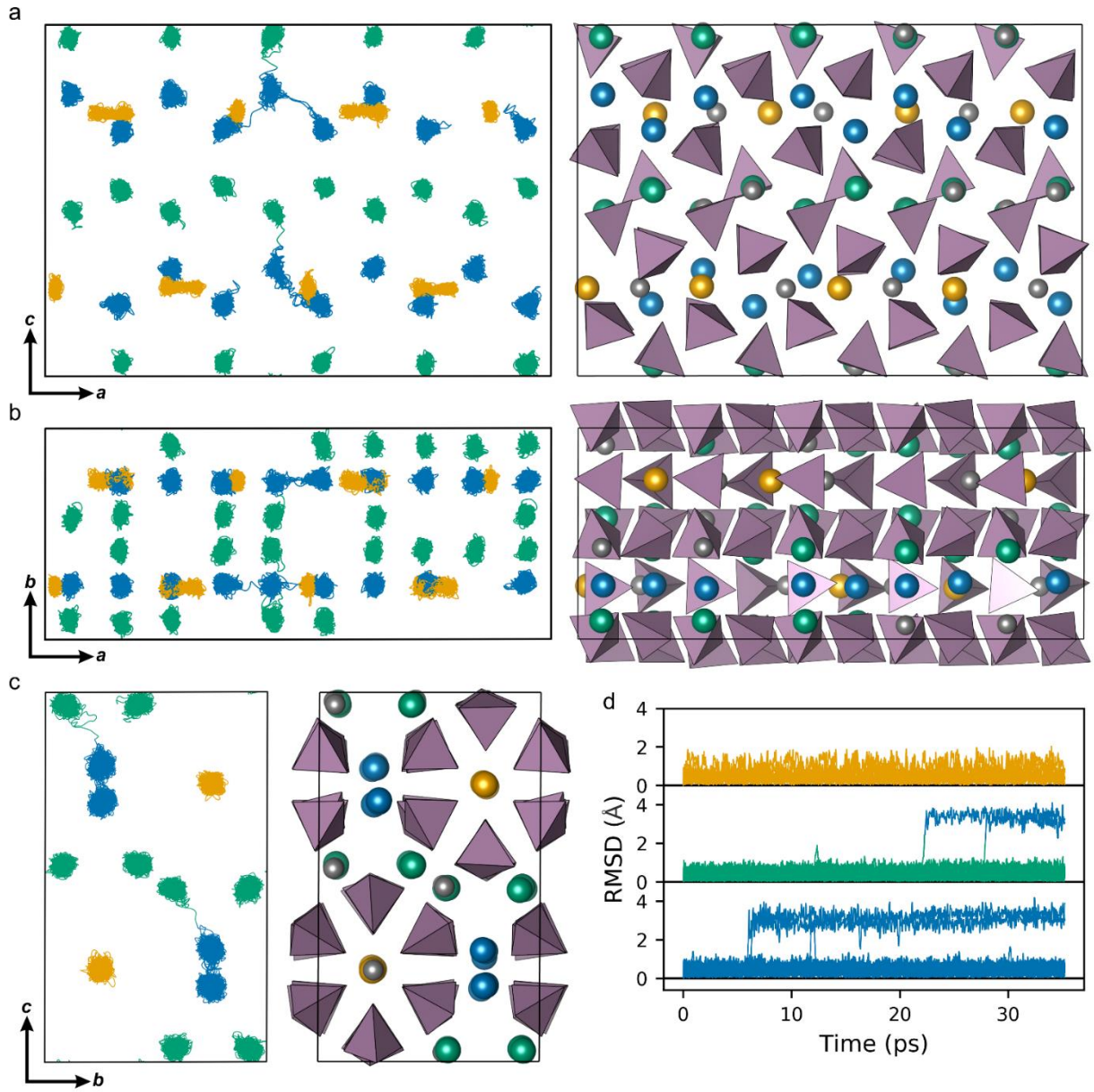

Figure 4.12: Generated by E. Shoko and M. Dyer (a-c) The trajectory of Li atom positions for the 35 ps AIMD run is plotted and viewed along the different supercell axes. In each case, the corresponding view of the full structure at the start of the production run is shown to the right, plotted with VESTA. (d) The root mean-square displacements (RMSD) of all the Li atoms in the simulation cell from their initial

positions plotted as a function of time. MoO_4 tetrahedra are plotted in purple, Fe atoms in grey, M1 site Li in gold, M2 site Li in green and M3 site Li in blue.

4.4 Discussion

Structure of $Li_{2.775}Fe_{1.075}(MoO_4)_3$: The structure of $Li_{2.775}Fe_{1.075}(MoO_4)_3$ consists of MoO_4 tetrahedra which connect chains Li/FeO6 octahedra and trigonal prismatic lithium sites. The connectivity of each site is shown in **Figure 4.1**, and the structure is largely invariant at the measured temperatures with only the lithium occupancy changing. The M1 sites are connected via face sharing octahedra to form chains surrounded by MoO_4 tetrahedra. The M2 sites form edge sharing distorted octahedra along the a-axis and each chain is connected via a corner sharing MoO_4 tetrahedra. The M3 lithium prismatic sites form chains of edge sharing prisms along the a-axis and can connect to M2 chains via a shared corner. The M1 and M3 chains are parallel to each other and separated by MoO_4 tetrahedra. The structure of $Li_{2.775}Fe_{1.075}(MoO_4)_3$ calculated using neutron powder diffraction at various temperatures does not change and resembles isostructural compositions in the literature. [139, 4, 141, 142, 143] However, these reports all suggest that the structures contain no vacancies and that the M3 site is occupied solely and fully by lithium.

Refinements against the neutron diffraction data shows the calculated lithium distribution to be different to that proposed by the published. [4] The M1 site is occupied with a Fe:Li ratio of 0.434:0.424 (**Table 4.2**) at 150 K and the lithium distribution increases with increasing temperature to 0.517 at 450 K shown in **Figure 4.8**. The M3 site lithium distribution is also only partly occupied; at 150 K ~0.98 (**Table 4.2**) and this decreases with increasing temperature to 0.91 at 450 K **Figure 4.8**. Therefore, the M1 and M3 sites both contain vacancies and these vary with increasing temperature. As the temperature is increased, the M1 site vacancies decrease from 0.146 to 0.08 at 150 K and 450 K respectively. Alternatively, the M3 site vacancies increase from 0.02 to 0.09 at 150 K and 450 K respectively, indicating Li^+ movement through the M3 site. On the contrary, the M2 sites remain fully occupied with a consistent Fe:Li ratio of ~ 0.32:0.68 at all temperatures.

Electrochemical performance: The room temperature total ionic conductivity of 1.10(4) x 10^{-7} S cm $^{-1}$ calculated for $Li_{2.775}Fe_{1.075}(MoO_4)_3$ is too low for use as a solid electrolyte [54], nevertheless, the total ionic conductivity at 343 K reached 8.2(2) x 10^{-7} S cm^{-1}, almost an order of magnitude higher showing a marginal improvement with temperature. The activation energy calculated 0.49(2) eV is in good agreement with activation energies calculated for other solid Li ion conductors reported in the literature [152, 138, 51] and suggests Li^+ ions can move with relative ease through the structure. The lack of a low frequency tail, indicative of Li^+ blocking at the electrode, in the Nyquist plot (**Figure 4.9**) indicate that the material is not a solid electrolyte. Furthermore, the low frequency semicircle, attributed to the Au electrode interface, suggests the contact of the $Li_{2.775}Fe_{1.075}(MoO_4)_3$ grains with the Au electrode allows some electronic conductivity to pass through likely due to the Fe^{3+}/Fe^{2+} redox couple. The electronic conductivity of the material was confirmed using DC polarization which resulted in an electronic conductivity of 3.52(5) × 10^{-8} S cm^{-1} at room temperature.

Lithium Conduction pathway: The lithium distribution of $Li_{2.775}Fe_{1.075}(MoO_4)_3$ calculated via neutron diffraction shows that the M1 and M3 site both contain vacancies; it is therefore likely that Li^+ conduction occurs via chains along the a-axis generated by these sites. As the M1 site vacancy concentration decreases with increasing temperature and the M3 site vacancy concentration increases with increasing temperature, the likely pathway is the M3 site chains. Furthermore, the M3 site is occupied solely by lithium and hence movement will not be hindered by iron within the chain as is the case with the M1 conduction pathway. The connectivity of the prismatic sites (**Figure 4.1**) provides a larger "tunnels" for lithium to move through with a diameter of approximately 2.5 Å, this is almost 4 times larger than the ionic radii of Li^+, 0.74 Å [128]. This is supported by the AIMD simulations where Li^+ movement is predominantly observed between M3 sites. The RMSD data (**Figure 4.12 d**) also shows two Li^+ ions moving a distance of 3.2 Å, consistent with the M3-M3 distance, calculated via NPD, of 3.15 Å. While the M3 partial occupancy of 0.75 in the MD simulations is lower than that calculated via NPD, 0.93(2), the hopping events observed in the AIMD simulations are only to neighbouring vacancy sites and is used to indicate where the Li-ion migration pathway is within the structure.

4.5 Conclusions

$Li_3Fe(MoO_4)_3$ has been synthesized using a solid state method with a temperature as low as 600 ^oC, and structurally characterized using x-ray diffraction and neutron diffraction to reveal a stoichiometry of $Li_{2.775}Fe_{1.075}(MoO_4)_3$, which is slightly richer in Fe than the published structure. The structure crystallizes in space group Pmna (62) with room temperature lattice parameters *a*= 5.08986(4) Å, *b*= 10.45048(9) Å and *c*= 17.5266(1) Å calculated via room temperature neutron diffraction. The Li ion transport has been fully characterized using EIS, DC polarization and AIMD. The total room temperature conductivity was calculated to be 1.10(4) x 10^{-7} S cm $^{-1}$ with an electronic conductivity contribution of 3.52(5) × 10^{-8} S cm^{-1}. AIMD revealed Li^+ hopping occurs predominantly through the M3 chains where the lithium migration is aided by large "tunnels" and unhindered by Fe ions within the chain. The study of the Li^+ transport within $Li_{2.775}Fe_{1.075}(MoO_4)_3$ will aid in understanding the materials behaviour as a potential cathode in an ASSB and can be used to generate and understand other $Li_3M^{3+}(MoO_4)_3$ structures.

CHAPTER 5: UNDERSTANDING THE STRUCTURAL CHANGES OF $LI_3FE(MOO_4)_3$ WHEN USED AS A CATHODE MATERIAL

5.1 Introduction

Polyanion cathode materials utilizing (XO_4) tetrahedra units [Where X= P, W, Mo, Si, S] connecting MO_x polyhedra [Where M is a transition metal], have been researched due to their increased thermal stability in comparison to conventional layered transition-metal materials.[153] $LiFePO_4$ was the first polyanion cathode reported by Goodenough [154] with a capacity of 100-110 mA h g^{-1}, and research has continued in this field with capacities now approaching ~140 mA h g^{-1} for Li_2FeSiO_4 and $LiFeSO_4F$.[155, 156] NASICON type structures, discussed in Chapter 4, such as $LiTi_2(PO_4)_3$ can also be classed as polyanion type cathode materials when a reducible transition metal element is used.This has led to research focussed on lattice matching structures within an ASSB in an attempt to decrease interfacial resistance within a battery.[96] Finding other materials which share this lattice matching behaviour will benefit the manufacturing of commercial ASSB's.

NASICON molybdate structures $Li_3M^{3+}(MoO4)3$ and $Li_2M^{2+}{}_2(MoO4)_3$, described in Chapter 4, can be synthesised containing a vast amount of transition metals and could, depending on the redox potential of the transition metal element, potentially utilize this lattice matching behaviour across the electrolyte/cathode interface.[157] Recently, a report of $Li_3Cr(MoO_4)_3$ as a cathode material with a specific capacity of 200 mA h g^{-1} has prompted research into molybdate materials for use as a cathode within a Li-ion battery.[136] Isostructural materials reported previously, $Li_2Ni_2(MoO_4)_3$ and $Li_3V(MoO_4)_3$, produce stable cycling capacities of ~115 mA h g^{-1} and ~130 mA h g^{-1} and can reversibly insert and extract Li ions in wide voltages windows of up to 1.5 V- 5 V.[137, 135] The higher than expected capacities of these molybdate materials has been attributed to the reduction of Mo^{6+}, and if true, could yield a possible route for increased capacity within an ASSB.[136, 137, 135, 134]

$Li_3Fe(MoO_4)_3$ has been widely researched in the literature for its use as a cathode material and can produce a stable cycling capacity of ~150 mA h g^{-1},[134] however a consensus on the structural changes which occur within the charge/discharge curves has not be reached. A structural study performed on a powdered material indicates that three phases are present during the first discharge.[158] Further research shows that, including $Li_4Fe(MoO_4)_3$, the final two phases include a rock-salt type Fe-O phase and amorphous phase $Li_{3+5}Fe(MoO_4)_3$, [134] however full structural characterisation of the phases present and the effect on the cycling has not been performed. As this behaviour is not seen in isostructural materials, [136, 137, 135] investigating the unusual structural changes which occur during galvanostatic cycling of $Li_3Fe(MoO_4)_3$ will yield a better understanding of its performance as a cathode.

5.2 Experimental

Synthesis: Synthesis of powdered $Li_3Fe(MoO_4)_3$ was performed as stated in section 4.2. The powdered sample was then used to conduct further measurements.

Electrochemical measurements: $Li_3Fe(MoO_4)_3$ electrodes were prepared by hand grinding as-prepared $Li_3Fe(MoO_4)_3$, carbon black and ploytetraflouroethylene (PTFE) in the ratio 60:30:10 wt % using a pestle and mortar, followed by pressing the mixture in the form of a 10 mm thin pellet. Charge/discharge tests were performed in Swagelok cells, sealed in an Ar atmosphere, using 1 M LiPF6 in EC/DMC (1:1) as the electrolyte

and lithium foil as the counter and reference electrodes. Cycling tests were performed using a BioLogic VMP-300 potentiostat in the voltage range 1.5- 4.2 V and 1.7 V- 4.2 V using a C/20 and C/10 discharge rate respectively. Cyclic voltammetry was performed between 1.5 V and 4.2 V with a scan rate of 1 mV s^{-1}.

EXAFS measurements: Two $Li_3Fe(MoO_4)_3$ electrodes and a standard of Li_2MoO_4 were prepared as stated above and the $Li_3Fe(MoO_4)_3$ samples discharged on a BioLogic VMP-300 potentiostat down to 2.0 V and 1.5 V. The cells were then disassembled in an Ar filled glovebox and the cathode removed the current collector and left in a sample jar to dry. The samples were then pressed in 10 mm pellets and attached to a rack with kapton tape. The rack was then sealed in an aluminium bag for transport for measurements conducted by Alan Chadwick (Diamond light source reward of beam time as part of BAG SP14239) and colleagues on the Mo K Edge of the samples. Normalisation of the data and alignment was then conducted using the Athena program as part of the Demeter computer package. [159]

Structural characterisation: Two $Li_3Fe(MoO_4)_3$ electrodes were prepared as stated above and discharged on a BioLogic VMP-300 potentiostat to 2.0 V and 1.5 V. The cells were then disassembled in an Ar filled glovebox and the cathode removed from the current collector and left in a sample jar to dry. The samples were then reground and mounted within an air sensitive x-ray diffraction sample holder and measured at room temperature on a Rigaku miniflex benchtop x-ray diffractometer employing Cu Kα radiation (λ=1.5406 Å) over a 10-60^o 2θ range, with a scan rate of 0.8 ^{o} min^{-1}. Rietveld refinement was performed against the powder diffraction data using the GSAS suite of programs [107], employing a pseudo-Voigt peak shape and a shifted Chebyschev background function. Starting structures of $Li_3Fe(MoO_4)_3$ [4] and the reported structure of $Li_4Fe(MoO_4)_3$ in Ref [158] were used to perform the refinements.

5.3 Results

Galvanostatic cycling data (**Figure 5.1**) of a $Li_3Fe(MoO_4)_3$ composite cathode within a liquid cell indicates that the cell can achieve a stable cycling capacity of ~150 mA h g^{-1} comparable to that in the literature. However, the first discharge curve is distinctly different to that of subsequent cycles with two plateaus shown i) at ~2.4 V and ii) at ~1.7 V. In previous reports the first plateau is attributed the Fe^{3+}/Fe^{2+}redox couple and

the second plateau to the reduction of Mo^{6+}.[134, 158] The subsequent Dq/DV data (**Figure 5.2**) shows an enormous, irreversible, capacity loss at ~ 1.7 V which corresponds to the long plateau in the same region within the galvanostatic cycling data. The following cycles shows capacity loss occurring at ~2.3 V and a small loss occurring at ~3 V. The capacity is then recovered in the same regions upon charge. This indicates that the cell shows suitable Li reversibility after the first discharge. The CV (**Figure 5.3**) collected over the same voltage range shows similar capacity changes, reduction occurring at ~2.0V and 3.5 V and oxidation occurring at 2.5 V and 3.7 V, however no reduction peak at 1.7 V during the first cycle. It is therefore unlikely that the capacity loss observed at 1.7 V is that of a redox couple.

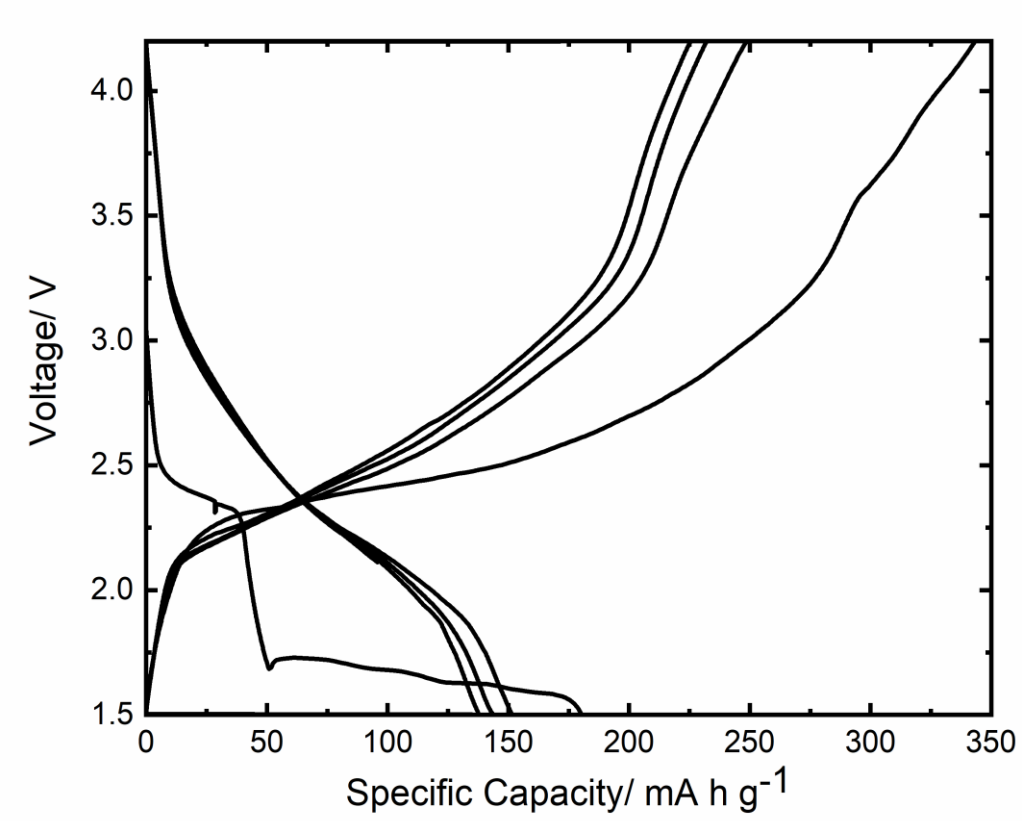

Figure 5.1: Galvanostatic cycling of a liquid cell with a $Li_3Fe(MOO_4)_3$ composite cathode using 0.69 mg active material at a rate of C/20 and constant current of 0.166 mA.

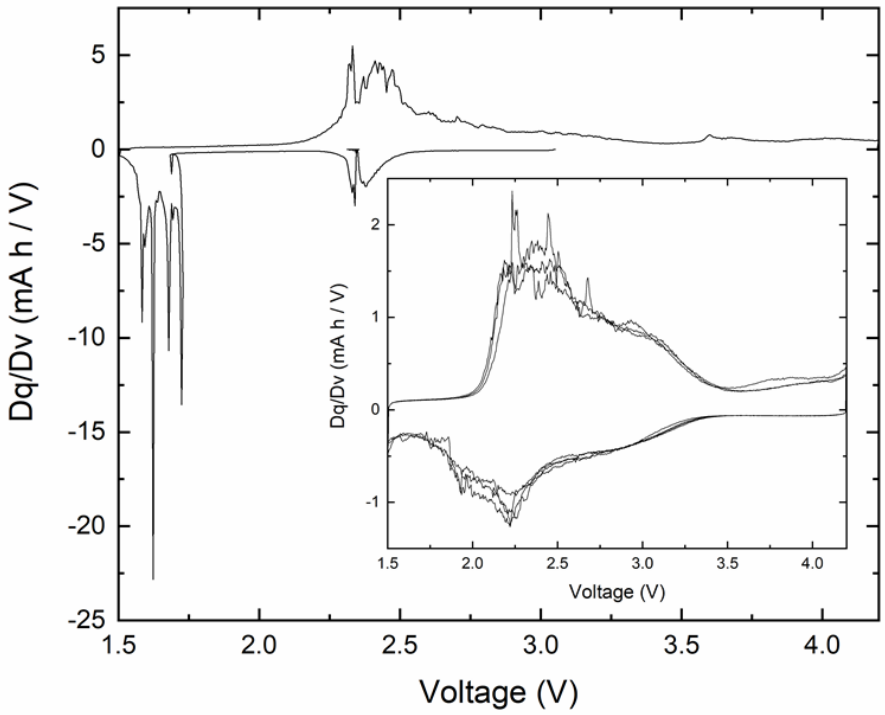

Figure 5.2: dQ/dV data calculated from galvanostatic data collected on a $Li_3Fe(MoO_4)_3$ cell.

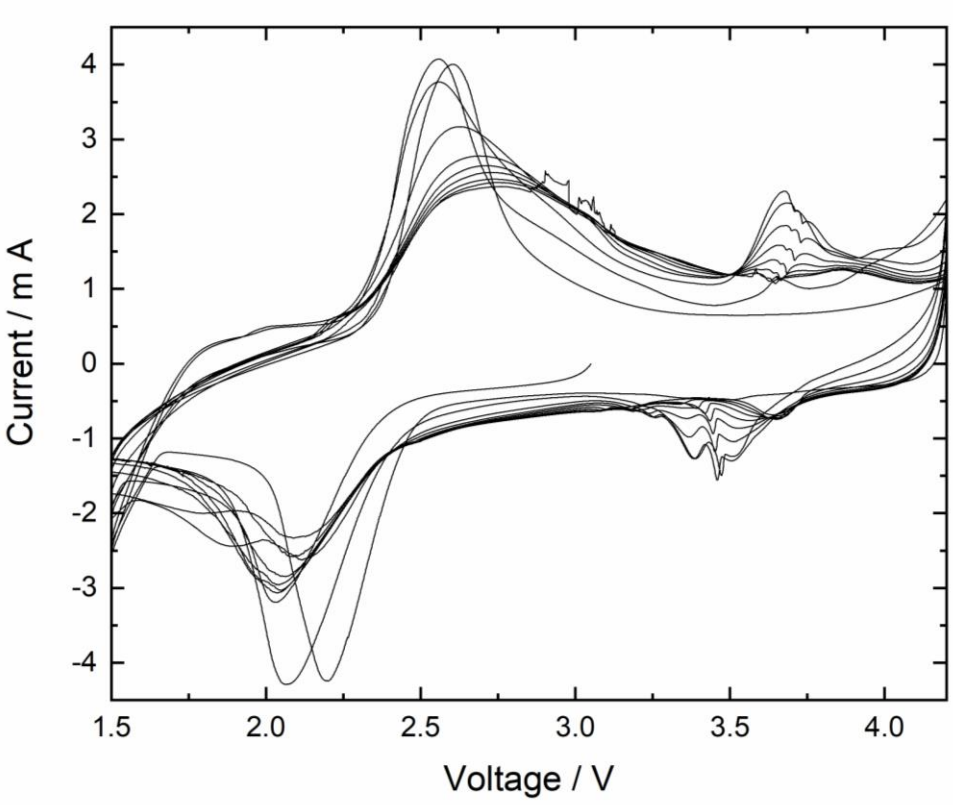

Figure 5.3: Cyclic voltagram for data collected between 1.5 and 4.2 V on a $Li_3Fe(MoO_4)_3$ cell with a scan rate of 1 mV s^{-1}.

To fully investigate the unusual cycling data observed by this material XANES data was collected on ex-situ samples (**Figure 5.4**). The data shows that Mo likely remains in the 6^+ oxidation state with the XANES data for the sample discharged to 1.5 V displaying a similar edge jump and pre edge feature associated with the standard Li_2MoO_4. This suggests that the long plateau and unusual capacity loss occurring at ~1.7 V is not due to the reduction of Mo^{6+}.

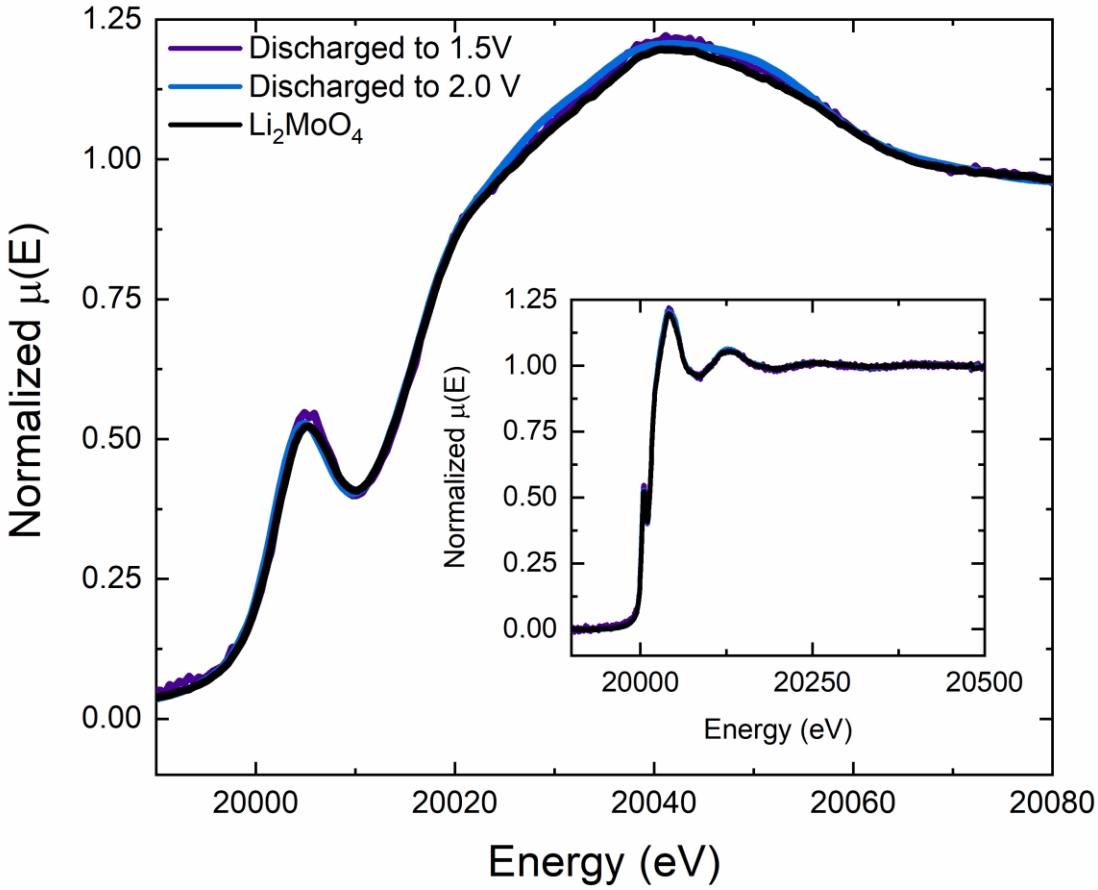

Figure 5.4: XANES data collected on two discharged samples of $Li_3Fe(MoO_4)_3$ i) a sample discharged to 1.5 V shown in purple, ii) a sample discharged down to 2 V and a standard sample of Li_2MO_4 shown in black. The inset shows the full EXAFS data**.**

Ex-situ samples of cycled material were then examined by air sensitive XRD (**Figure 5.5)** to investigate the possible structural changes occurring during discharge which could explain the capacity loss occurring at 1.7 V.The pristine sample shows allowed

Bragg reflections for $Li_3Fe(MoO_4)$, however the intensity of these peaks decreases slightly when discharged down to 2 V (After the first plateau in the cycling data **Figure 5.1)**. Indicating the structure is unaffected down to 2 V. Once the sample has been discharged down to 1.5V almost all of the allowed Bragg reflections for $Li_3Fe(MoO_4)$, have diminished and an increase in the low angle background is observed as well as two clear peaks at ~ 37º and 44º 2θ (shown with an asterisk on **Figure 5.5**. These peaks can be characterised as those belonging to a disordered rock salt type phase, likely that of $Li_3Fe_5O_8$ or $LiFe_5O_8$ [160, 161] This implies that the long plateau at 1.7 V is likely caused by the decomposition of the $Li_3Fe(MoO_4)_3$ structure and the following cycles involve the resultant structure(s). The higher background at low angles can indicate an amorphous phase has been formed during discharge.

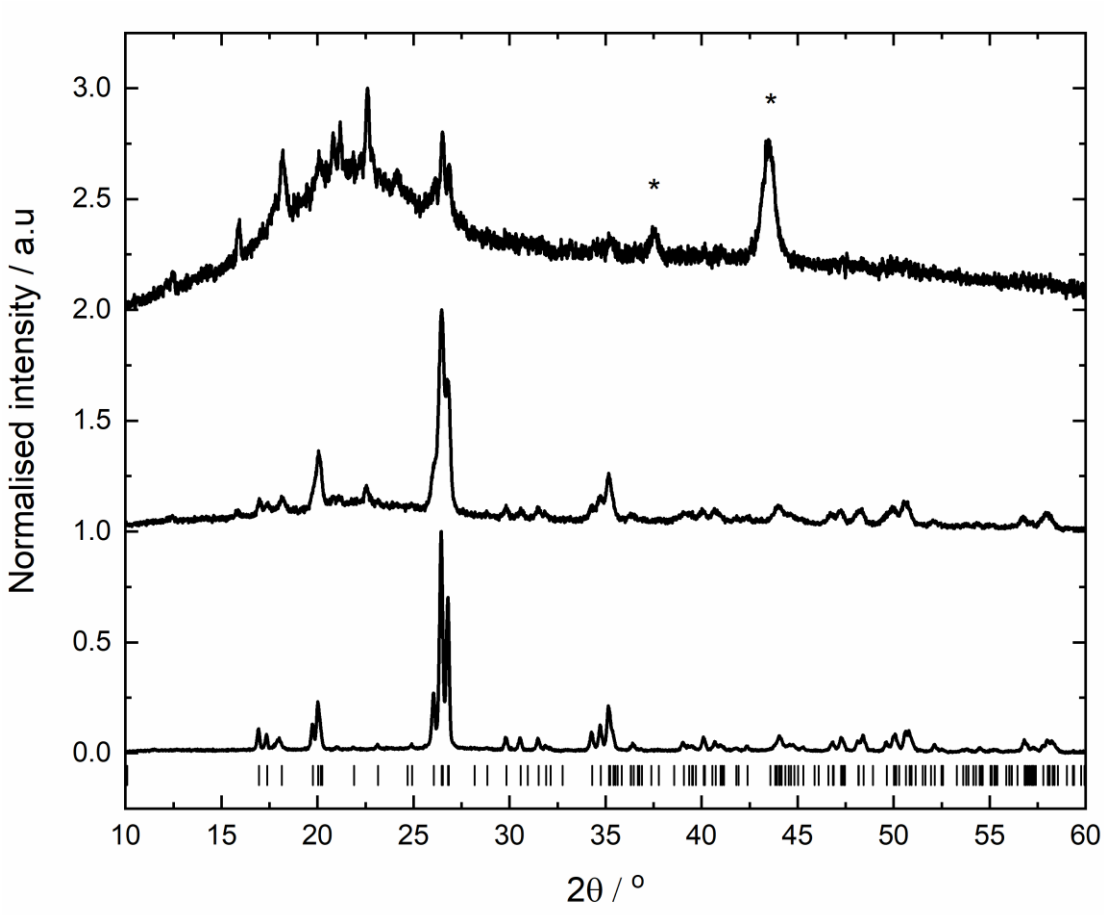

Figure 5.5: Normalised x-ray diffraction data of $Li_3Fe(MoO_4)_3$ (bottom), sample discharged to 1.5 V (middle), sample discharged to 2 V (top). Allowed Bragg reflections for $Li_3Fe(MoO_4)_3$ are shown by dashes below with asterisks showing uncharacterised peaks.

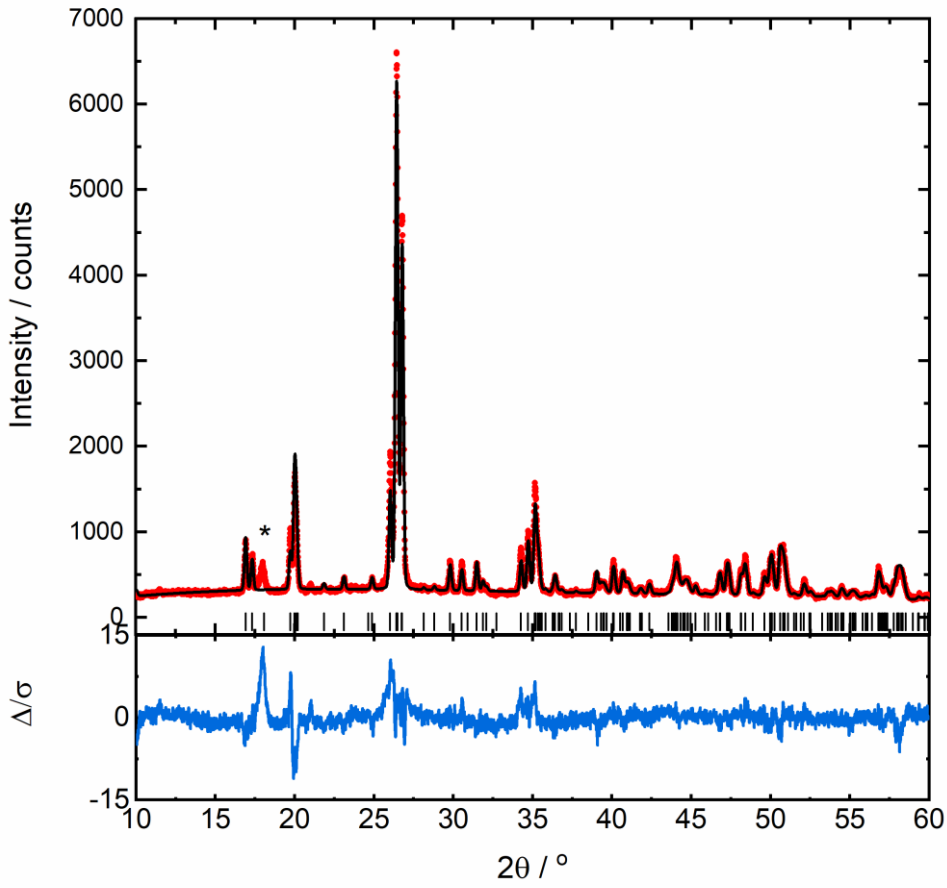

Figure 5.6: Rietveld refinement against powder x-ray data collected on a $Li_3Fe(MoO_4)3$ + C + PTFE composite cathode at room temperature. Observed data shown in red, calculated in black and Δ/σ in blue. Ticks show allowed Bragg reflections for $Li_3Fe(MoO_4)_3$ with Bragg reflections for PTFE shown with an asterisk.

A refinement against room temperature data on a pristine composite cathode of $Li_3Fe(MoO_4)_3$ produced a GOF of 1.85 and Rw of 9.114 (**Figure 5.6**). The calculated lattice parameters were found to be *a*=5.0896(3) Å, *b*=10.4451(5) Å and *c*= 17.527(1) Å with a unit cell volume of 931.7(1) $Å^3$, similar to that calculated via neutron diffraction (*a*= 5.08986(4) Å, *b*= 10.45048(9) Å and *c*= 17.5266(1) Å with a total unit cell volume of 932.26(2) $Å^3$).

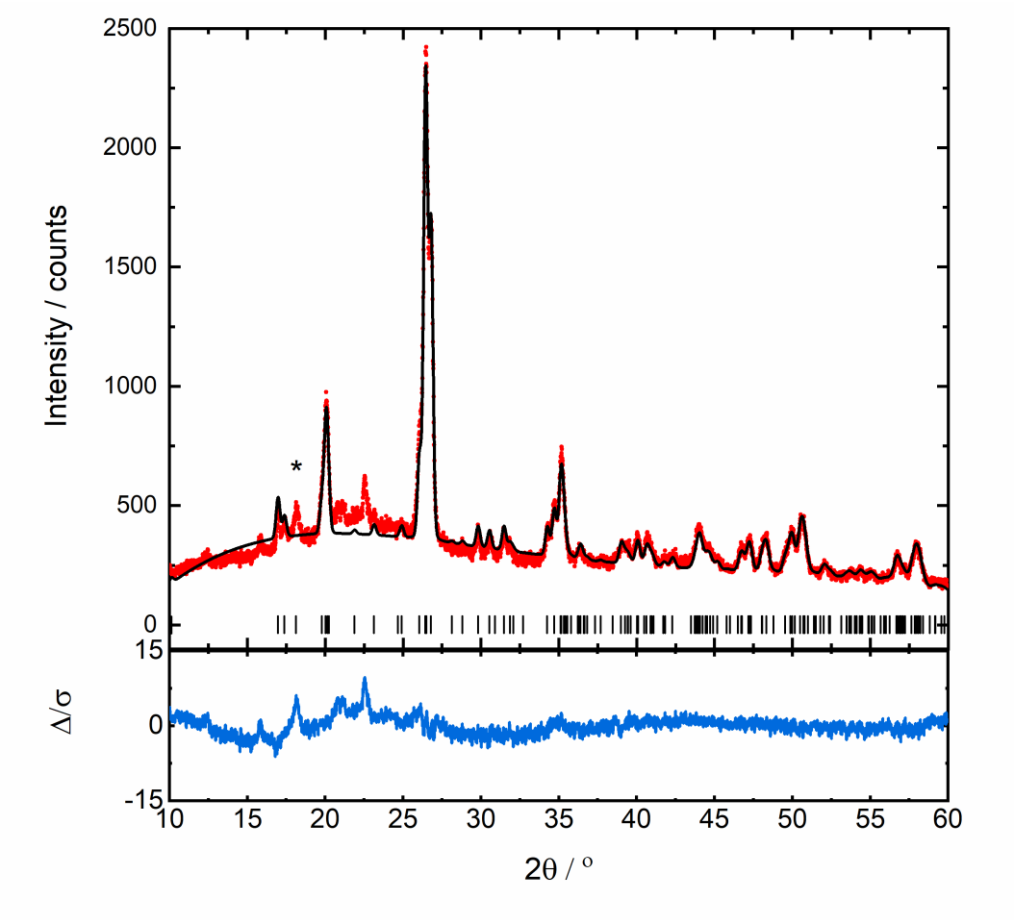

Figure 5.7: Rietveld refinement against powder x-ray data collected of a $Li_3Fe(MoO_4)_3$ + C + PTFE composite cathode discharged down to 2 V at room temperature. Observed data shown in red, calculated in black and Δ/σ in blue. Ticks show allowed Bragg reflections for $Li_4Fe(MoO_4)_3$ Bragg reflections for PTFE are highlighted with an asterisk.

Table 5.1: Atomic position parameters for room temperature $Li_4Fe(MoO_4)_3$

Atom	Type	x	y	Z	SOF	Uiso	Multiplicity
Mo1	Mo6+	0.2784	0.52619	0.1562	1	0.009	8
Mo2	Mo6+	0.7795	0.25	0.05712	1	0.007	4
Fe1	Fe2+	0.1066	0.25	0.2513	0.333	0.009	4
Li1	Li1+	0.1066	0.25	0.2513	0.667	0.009	4
Fe2	Fe2+	0.7548	0.5713	0.0265	0.333	0.008	8
Li2	Li1+	0.7548	0.5713	0.0265	0.667	0.008	8
Li	Li1+	0.34	0.75	0.388	1	0.01	4
Li3	Li1+	0.247	0.75	0.3	1	0.025	4
O1	O2-	0.865	0.25	0.1549	1	0.01	4
O2	O2-	0.055	0.25	-0.0053	1	0.011	4
O3	O2-	0.58	0.1148	0.0368	1	0.008	8
O4	O2-	0.082	0.49	0.0739	1	0.006	8
O5	O2-	0.078	0.6255	0.2118	1	0.013	8
O6	O2-	0.358	0.381	0.207	1	0.009	8
O7	O2-	0.561	0.612	0.1271	1	0.013	8

The Rietveld refinement against room temperature data on an ex-situ sample discharged down to 2 V produced a GOF of 1.77 and Rw of 9.554 (**Figure 5.7**). The calculated lattice parameters were found to be *a*=5.112(1) Å, *b*=10.486(2) Å and *c*= 17.595(3) Å with a unit cell volume of 943.2(5) $Å^3$, larger than the pristine cathode. This increase is expected due to the insertion of 1 Li^+ atom (**Table 5.1**) as well as the increase in ionic radii of Fe^{2+}. It should also be noted that the low angle background has slightly increased in comparison to that of the pristine cathode indicating an amorphous phase could be forming.

In an attempt to avoid the structural changes, which occur at 1.7 V, galvanostatic measurements were taken over a smaller voltage window 1.7 V- 4.2 V. **Figure 5.8** shows that the first discharge results in a specific capacity of ~48 mA h g^{-1} comparable to that of the theoretical capacity of $Li_3Fe(MoO_4)_3$ (48.15 mA h g^{-1}). However, a similar problem to that occurring at 1.7 V is observed upon charge where 3 long plateaus are produced, i) at ~3.5 V ii) ~3.7 V and ii) 4.1 V. Further cycling shows the capacity greatly reducing to ~20 m A h g^{-1} and no strong plateaus occurring in either the charge or discharge.

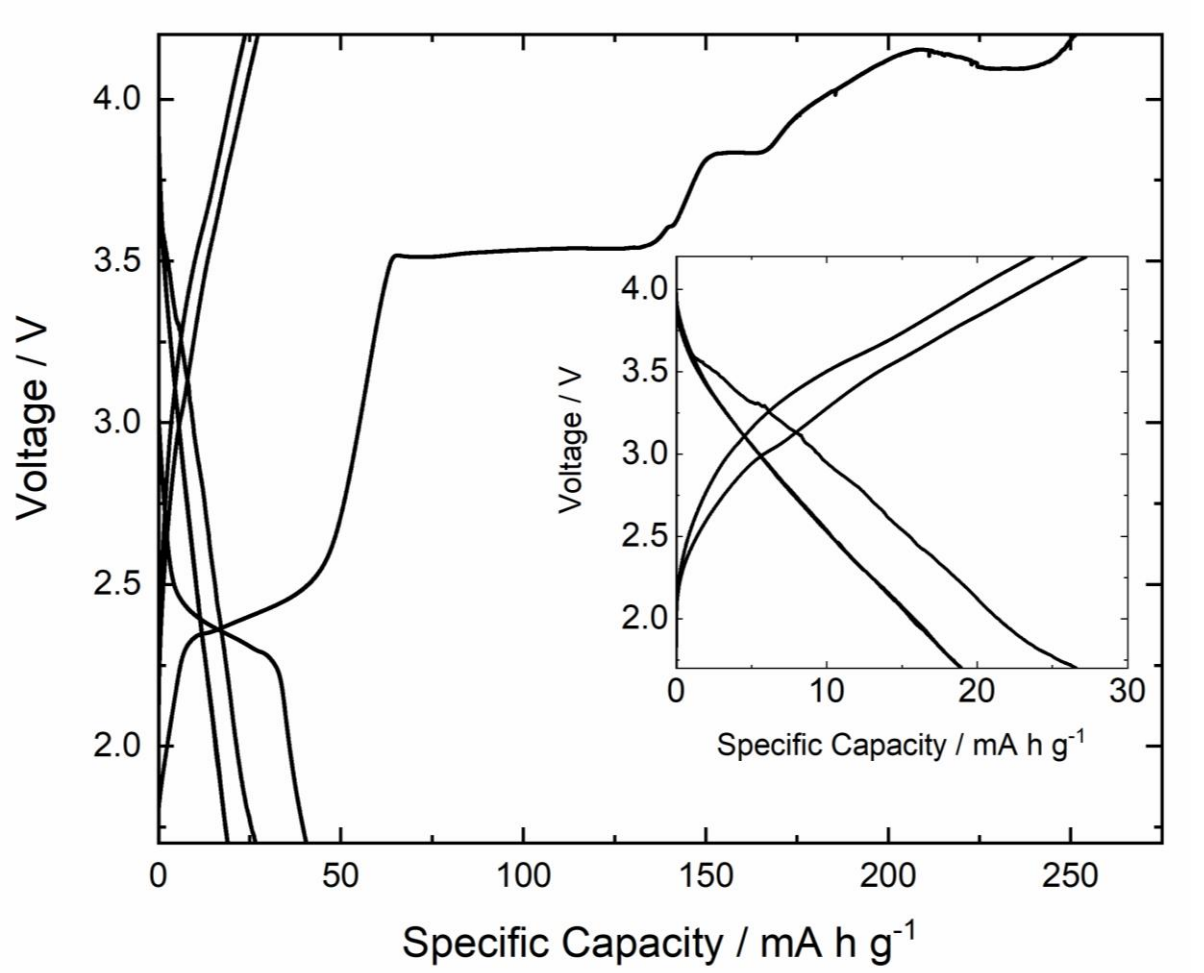

Figure 5.8: Galvanostatic cycling of a liquid cell and $Li_3Fe(MoO_4)_3$ composite cathode between 1.7 V and 4.2 V Using 0.15 mg active material at a rate of C/10 and constant current of 0.076 mA. The inset shows the 2nd and 3rd cycles.

5.4 Discussion

Electrochemical behaviour: When used as a cathode in a liquid cell $Li_3Fe(MoO_4)_3$ behaves unusually, particularly due to the fact the cell is discharged first, it also differs electrochemically to that of isostructural materials. [136] [137] [135] The first discharge curve produces a higher capacity than that of subsequent cycles of ~175 m A h g^{-1} and involves a long plateau occurring at ~1.7 V. This also corresponds to an irreversible capacity loss observed in the dQ/dV data in the same region (**Figure 5.2**), however, not observed in the same region in the cyclic voltamogram (**Figure 5.3**). This indicated that the capacity loss observed here is not due to the reduction of Mo^{6+} as suggested in previous reports on the material and isostructural materials.[136] [137] [135] [134] The

charging behaviour is also strange as the charging capacity is much higher than that produced during discharge ~350 m A h g^{-1} with smaller plateaus occurring at ~ 3.0 V and 3.7 V (**Figure 5.1**). The plateau at ~ 3.7 V matches that to the oxidation peak in the cyclic voltagram (**Figure 5.3**) indicating that this is likely caused by a Fe redox couple. It is suggested in the literature that $LiFeO_2$, when used as a cathode forms Fe^{4+} during the initial charge, however due to its instability the reversible redox couple Fe^{3+}/Fe^{2+} provides the majority of the capacity likely causing the peaks at 2.0 and 2.5 V.[161] The peaks occurring at ~3 V and 3.7 V diminish with increasing cycles and could indicate a small amount of Fe^{4+} forming, leading to an increase in capacity.[162, 163]

The unusual behaviour observed in this material was further investigated using x-ray absorption spectroscopy performed on three samples shown in **Figure 5.4**. The two discharged samples show a clear resemblance to the standard Li_2MoO_4, where Mo is in the 6+ oxidation state and tetrahedral coordination, suggesting that at least in this material, the extra capacity observed during the 1st charge is not due the reduction of Mo^{6+}. As XANES measurements were not performed, conclusions cannot be made on the extra capacity in subsequent cycles. The extra capacity expected during the first charge as detected in isostructural materials was further investigated by decreasing the voltage window to 4.2 V – 1.7V, **Figure 5.8** illustrates the first discharge capacity to be ~48 mA h g^{-1}, similar to the theoretical capacity of the material (48.15 mA h g^{-1}). The curious behaviour is then seen during the first charge where plateaus are detected: i) at ~3.5 V ii) ~3.7 V and ii) 4.1 V, further cycles show the irreversibility of the changes occurring, with capacity fading much quicker than that of the cell operated within a wider electrochemical window.

Structural changes: The Rietveld refinement performed on the pristine cathode sample can be fitted well using the published structural data for $Li_3Fe(MoO_4)_3$ **Figure 5.6**, once the cell has been discharged down to 2 V (after the initial plateau in the cycling data shown in **Figure 5.1**). Rietveld refinement can be performed using published data on $Li_4Fe(MoO_4)_3$ **Figure 5.7**.[158] The increase in cell parameters and specific capacity at this point ~50 m A h g^{-1} substantiates the insertion of 1 Li^+ into the lattice producing $Li_4Fe(MoO_4)_3$, where Fe has reduced to Fe^{2+}. **Figure 5.5** shows the intensity of the allowed Bragg reflections for the $LiFe_3(MoO_4)_3$ decrease, in contrast to that observed in the pristine sample, and become broader suggesting the amount and crystallinity of the structure has decreased. Extra reflections then begin to form at ~ 16 ^{o}, 21 ^{o} and

22 º 2θ, suggesting a new phase is forming, these peaks are also present in the XRD data obtained for the sample discharged down to 1.5 V with the addition of much broader peaks at ~ 37 º and 43 º 2θ (shown on **Figure 5.5**). The low angle background begins to rise in the data obtained at 2 V and becomes obvious in data measured on the sample discharged down to 1.5 V. The peaks can be indexed as those belonging to an lithium iron oxide, which can be found in various phases.[160]

$LiFeO_2$ is a structure reported to have many polymorphs, and has been widely researched as a cathode.[164, 165] During cycling lithium can be easily inserted and extracted to form other lithium iron oxide structures, the peaks present at ~37 º and 43 º 2θ in the x-ray diffraction data on the sample discharged down to 1.5 V are likely that of $LiFe_5O_8$ which is a spinel type structure, this has been observed previously although the perfect spinel is unlikely to form during cycling.[166] There is also an orthorhombic $LiFeO_2$ structure which contains Fe in the 4+ oxidation state, due to the instability of this oxidation state research has showed this to become an amorphous phase which can take part in the lithium insertion extraction, this explains the high background present in the XRD discharged down to 1.5 V.[167] The destruction of the parent $Li_3Fe(MoO_4)_3$ structure at 2.0 V in the first discharge results in the formation of various $LiFeO_2$ polymorphs, the lithium insertion occurring during the long plateau at 1.5 V likely forms the spinel and orthorhombic phases. These resulting structures are then producing the extra capacity seen thereafter of ~150 mA h g^{-1}.

The investigation into the smaller electrochemical window of 4.2 V to 1.7 V (**Figure 5.8**) also shows various long plateaus above 3 V, these correspond to plateaus seen during cycling of Li_5FeO_4 cathode materials which produces plateaus at 3.5 V and 4.0 V.[168] The plateau at 3 V is likely due to the decomposition of the parent phase to the iron oxide structure. However, this phase is not as stable as those formed during the discharge process at 1.5 V in the wider window cell as the capacity greatly reduces in subsequent cycles of the smaller window cell.

5.5 Conclusions

$Li_3Fe(MoO_4)_3$ shows unusual cycling behaviour in the voltage window 4.2 to 1.5 V, previously this was attributed to the reduction of Mo^{6+}. The XAS data collected on samples discharged to 2.0 V and 1.5 V indicates that this is not the case, and further

experiment shows that structural changes occur during the long plateau at 1.5 V in the galvanostatic cycling data. During the first discharge of the cell, the parent material first undergoes lithium insertion to become isostructural $Li_4Fe(MoO_4)_3$, with a capacity of ~50 m A g^{-1}, this material then decomposes to produce various polymorphs of $LiFeO_2$, with the final structures at 1.5 V being spinel $LiFe_5O_8$ and orthorhombic $LiFeO_2$ which becomes amorphous due to the unstable Fe4+ oxidation. These structures then produce the increased capacity of 150 m A g^{-1} thereafter. Decreasing the voltage window to reduce the decomposition occurring at 1.5 V results in the polymorph Li_5FeO_4 forming during the first charge, this is unstable during subsequent cycles and the capacity is greatly reduced. Based on the cycling data on the two cells cycled, the electrochemical voltage window of $Li_3Fe(MoO_4)_3$ is smaller than isostructural materials and likely in the range 3 – 1.8 V.

CHAPTER 6: FUTURE WORK AND CONCLUSIONS

6.1 Doping of $LiTa_2PO_8$

Attempts to synthesis other family members containing Nb, Sb and Zr were unsuccessful, however not all possibilities were attempted, the fact that small amounts of dopants could be introduced in the structure is promising for the potential of other family members to be found. The work on this compound did not yield any improvement on conductivity due to the difficulty in the densification of the material. Research has already moved to this area, Zhang et al discusses the use of additives such as Li_2O to increase the grain boundary conductivity as well as research on processing the material to increase the density as reported by Huang et al via hot pressing the material.[169, 120] Further work focussing on reliably generating dense materials as well as doping the compound could produce structures which have an improved conductivity for use as a solid electrolyte.

Due to the recent discovery of this material, full solid state cell testing has not been performed and so a true understanding of how this material behaves in contact with solid state cathodes is also needed. Recent research has indicated the structures ability to increase the performance of some cells when used as an additive, indicating the materials full potential has not been uncovered.[170, 171] Due to the reported high

conductivity of the material, research on using the material as an additive should be pursued further in order to fully investigate the structures ability to enhance solid state battery performance, especially due to the simplicity of synthesis and the structures stability in air, both are beneficial for the commercialisation of all-solid state batteries.

A promising start has been made on fully understanding and researching this structures ability to be used as a solid electrolyte, however no reports have been made on other family members or on the doping of this compound. The work shown within this thesis clearly shows an increase in conductivity, relative to the $LiTa_2PO_8$ structure synthesised in this work, when the structure is doped with Sb. The activation energy calculated through SSNMR confirms that Sb doping changes the structure to increase the materials performance as a conductor. Full structural information is required to fully understand how the doping changes the intrinsic properties of the structure. Due to the light elements present in the sample, P, O and Li, neutron diffraction on the structure is definitely needed to fully understand the distribution of dopant within the structure and if the lithium distribution is changed upon introduction of dopants, particularly when Sb is introduced. An electrochemical study on the Zr doped sample is also required, as the introduction of a 4^+ transition metal ion should lead to an increase in Li^+ ions hence an increase in conductivity could be possible due to the increase in charge carrier concentration. The work on dopants should be performed after a clear densification procedure is uncovered this is to allow the best comparison to its use as a solid electrolyte within a battery.

6.2 Li ion transport properties in $Li_3Fe(MoO_4)_3$

It is clear that the Li hopping events occur via the M3 sites within the structure as previously theorised, a full understanding of the Li-ion conduction pathway can now release the potential for other isostructural materials to be considered for use in a battery. [88] The research also indicates that $Li_3Fe(MoO_4)_3$, contains vacancies on the Li containing sites and this can be extended to include other $Li_3M^{3+}(MoO_4)_3$ structures. Varying this stoichiometry could produce materials with a greater ionic conductivity than that reported for $Li_3Fe(MoO_4)_3$, combined with a transition metal ion which is stable in the 3^+ oxidation state could provide a solid electrolyte with a similar lattice, hence lattice matching could occur across the cathode/electrolyte interface.

The research on understanding these molybdate structures within a battery is fairly recent, with an increased amount of research ongoing for their use as a cathode, however little has been performed in understanding the transport properties through the structure.[136, 135, 143] Fully characterising the reported structures is needed to fully understand the potential battery materials within the molybdate family, and this could lead to further structures being discovered capable of enhanced battery performance. This work could also aid in the research of other $(MO_4)_x$ containing structures such as $(WO_4)_x$ structures, which are also being considered for their use as electrodes within a cell. [172, 173]

6.3 Structural changes within $Li_3Fe(MoO_4)_3$ when used as a cathode

Unlike isostructural materials, $Li_3Fe(MoO_4)_3$ produces a higher than expected capacity with a long plateau occurring in the first galvanostatic discharge curve. The theory in the case of these molybdates is that the increased capacity is due to the reduction of Mo^{6+}, however XAS on discharged $Li_3Fe(MoO_4)_3$ samples suggests this is not the case. [135, 136] The unusual behaviour observed in the galvanostatic discharge data is not consistent with isostructural materials therefore, further research is needed in order to extend the lack of Mo^{6+} reduction to these materials. Further XAS measurements should be taken, alongside molybdenum standards to fully understand the oxidation changes occurring within the structure. Performing XAS on the Fe K-edge would alleviate the Fe oxidation state changes occurring over the discharge curve and performing a measurement on pristine $Li_3Fe(MoO_4)_3$, both Mo and Fe edges, would help understand the materials starting state. Full EXAFS fitting would also reveal local structural changes occurring over cycling, which could help in the full understanding of the structures produced at 1.5 V.

Alongside XAS measurements, structural data on $LiFeO_2$ polymorphs should be gathered when cycled in different electrochemical windows, this would aid in understanding which polymorphs are present at 1.5 V and why this aids the cycling of the material over the wider electrochemical window. It may also resolve the issue of Mo and what happens to this during cycling. Discovering how $LiFeO_2$ polymorphs, produced via the decomposition of $Li_3Fe(MoO_4)_3$, cycle in comparison to as synthesised will provide insight into the increased capacity observed. Further to this, a smaller electrochemical window should be used when cycling $Li_3Fe(MoO_4)_3$, if the

structure is to be maintained, as suggested this is likely in the window 3- 1.8 V but cycling data should be used to confirm this.

6.4 Overall Conclusions

It is evident that doping of solid electrolytes yields an increase in conductivity and this is evident in the case of $LiTa_2PO_8$, where Sb-doping increases the bulk conductivity of the material, relative to the $LiTa_2PO_8$ sample synthesised in this work. The synthesis of the sample was reproducible and performed in air, this is encouraging for the commercial use of this material in all-solid state batteries. The structure of the pristine sample has been well characterised in the literature, however research is required to synthesise other family members and further investigate the role of tantalum in the structures stability. The method of sintering in order to densify the material prior to use as a solid electrolyte also requires further investigation particularly to the role of the materials microstructure in the electrochemical behaviour of the material. The work in this thesis has generated an excellent starting point, in terms of materials discovery, for the production of other family members as well as the structures solubility limit of doping which is ~x=0.1 in $LiTa_{2-x}M_xPO_8$ [*M*=Nb and Sb].

The cathode structure $Li_3Fe(MoO_4)_3$ has been fully characterised using neutron diffraction to investigate the lithium distribution within the structure. This has provided great insight into the vacancy distribution within the structure and how this leads to Li-ion transport through the material. This can be widely applied to other $Li_3M^{3+}(MoO_4)_3$ structures particularly that of the off stoichiometric Li and *M,* producing vacancies within the structure. This investigation benefits future research into these molybdate structures and generating structures with increased vacancies on the M3 site could yield materials with enhanced Li-ion transport capabilities. Synthesising and investigating the structure with a stable M^{3+} transition metal could also offer the ability to lattice match two molybdate structures over the cathode electrolyte interface minimising interfacial resistance within an all-solid-state battery.

Investigating the structural changes occurring within $Li_3Fe(MoO_4)_3$, produced an understanding of the structures present after the initial discharge. This allows future research to focus on cycling the molybdate structure within a smaller electrochemical window, 1.8-3 V, where the material likely produces a capacity of ~48 mA h g^{-1} ~100%

of its theoretical capacity. Alternatively, research can focus on $LiFeO_2$ structures and how a mixture of these materials in a cathode can produce a capacity of ~150 mA h g^{-1}, this could be further increased if the Mo, which is unlikely to be reduced during cycling, is removed. Although, the investigation into the use of $Li_3Fe(MoO_4)_3$ as a cathode cannot provide insight in the role of Mo^{6+} reduction in isostructural materials, it has provided alternative research avenues for $Li_3Fe(MoO_4)_3$.

Overall, this thesis has shown that understanding the fundamental structure of battery materials and then investigating the electrochemical performance of materials can yield a better overall understanding of generating next generation batteries. A broader knowledge of both cathodes and electrolytes is needed to build the best next generation batteries and investigating cathodes with structures similar to electrolytes can lead to a better insight into the Li hopping mechanism through a cell. This work can be applied to future electrolyte and cathode materials where the focus is to lattice match these structures in a battery to aid in minimising the interfacial resistances present across the electrode/electrolyte boundary.

REFERENCES

1. Diouf, B. & Pode, R. Potential of lithium-ion batteries in renewable energy. *Renew. Energy* **76**, 375–380 (2015).
2. Schnell, J. *et al.* All-solid-state lithium-ion and lithium metal batteries – paving the way to large-scale production. *J. Power Sources* **382**, 160–175 (2018).
3. Kim, J., Kim, J., Avdeev, M., Yun, H. & Kim, S.-J. LiTa2PO8: a fast lithium-ion conductor with new framework structure. *J. Mater. Chem. A* **6**, 22478–22482 (2018).
4. Klevtsova, R. F. & Magarill, S. A. Crystal structure of lithium-ferriferrous molybdates Li3Fe(MoO4)3 and Li2Fe2(MoO4)3. *Krist. SSSR* **15**, 710–715 (1970).
5. Liu, C., Neale, Z. G. & Cao, G. Understanding electrochemical potentials of cathode materials in rechargeable batteries. *Mater. Today* **19**, 109–123 (2016).
6. Weber, A. Z. *et al.* Redox flow batteries: a review. *J. Appl. Electrochem.* **41**, 1137 (2011).
7. Dunn, B., Kamath, H. & Tarascon, J.-M. Electrical Energy Storage for the Grid: A Battery of Choices. *Science* **334**, 928–935 (2011).
8. Lu, Y. & B. Goodenough, J. Rechargeable alkali-ion cathode-flow battery. *J. Mater. Chem.* **21**, 10113–10117 (2011).
9. Winter, M. & Brodd, R. J. What are batteries, fuel cells, and supercapacitors? *Chem. Rev.* **104**, 4245–4269 (2004).
10. Nishi, Y. Lithium ion secondary batteries; past 10 years and the future. *J. Power Sources* **100**, 101–106 (2001).

11. Armand, M. & Tarascon, J.-M. Building better batteries. *Nature* **451**, 652–657 (2008).
12. Chen, S. *et al.* Challenges and Perspectives for NASICON-Type Electrode Materials for Advanced Sodium-Ion Batteries. *Adv. Mater.* **29**, 1700431 (2017).
13. Helbig, C., Bradshaw, A. M., Wietschel, L., Thorenz, A. & Tuma, A. Supply risks associated with lithium-ion battery materials. *J. Clean. Prod.* **172**, 274–286 (2018).
14. Bhatt, M. D. & Lee, J. Y. High capacity conversion anodes in Li-ion batteries: A review. *Int. J. Hydrog. Energy* **44**, 10852–10905 (2019).
15. Verma, P., Maire, P. & Novák, P. A review of the features and analyses of the solid electrolyte interphase in Li-ion batteries. *Electrochimica Acta* **55**, 6332–6341 (2010).
16. Thackeray, M. M., Wolverton, C. & Isaacs, E. D. Electrical energy storage for transportation—approaching the limits of, and going beyond, lithium-ion batteries. *Energy Environ. Sci.* **5**, 7854–7863 (2012).
17. Zhang, Z. (John), Fang, W. & Ma, R. Brief review of batteries for XEV applications. *eTransportation* **2**, 100032 (2019).
18. Zhou, D., Shanmukaraj, D., Tkacheva, A., Armand, M. & Wang, G. Polymer Electrolytes for Lithium-Based Batteries: Advances and Prospects. *Chem* **5**, 2326–2352 (2019).
19. Takada, K. Progress and prospective of solid-state lithium batteries. *Acta Mater.* **61**, 759–770 (2013).
20. Manthiram, A., Fu, Y. & Su, Y.-S. Challenges and Prospects of Lithium–Sulfur Batteries. *Acc. Chem. Res.* **46**, 1125–1134 (2013).
21. Rahman, Md. A., Wang, X. & Wen, C. A review of high energy density lithium–air battery technology. *J. Appl. Electrochem.* **44**, 5–22 (2014).
22. Alias, N. & Mohamad, A. A. Advances of aqueous rechargeable lithium-ion battery: A review. *J. Power Sources* **274**, 237–251 (2015).
23. Bubulinca, C. *et al.* Development of All-Solid-State Li-Ion Batteries: From Key Technical Areas to Commercial Use. *Batteries* **9**, 157 (2023).
24. Owens, B. B. & Skarstad, P. M. Ambient temperature solid state batteries. *Solid State Ion.* **53–56**, 665–672 (1992).
25. Liang, C. C. & Bro, P. A High-Voltage, Solid-State Battery System I . Design Considerations. *J. Electrochem. Soc.* **116**, 1322–1323 (1969).
26. Yao, X. *et al.* All-solid-state lithium batteries with inorganic solid electrolytes: Review of fundamental science. *Chin. Phys. B* **25**, 018802 (2016).
27. Yamamoto, K. *et al.* Dynamic Visualization of the Electric Potential in an All-Solid-State Rechargeable Lithium Battery. *Angew. Chem. Int. Ed.* **49**, 4414–4417 (2010).
28. Wang, P. *et al.* Electro–Chemo–Mechanical Issues at the Interfaces in Solid-State Lithium Metal Batteries. *Adv. Funct. Mater.* **29**, 1900950 (2019).
29. Bates, J. B., Dudney, N. J., Neudecker, B., Ueda, A. & Evans, C. D. Thin-film lithium and lithium-ion batteries. *Solid State Ion.* **135**, 33–45 (2000).
30. Sun, C., Liu, J., Gong, Y., Wilkinson, D. P. & Zhang, J. Recent advances in all-solid-state rechargeable lithium batteries. *Nano Energy* **33**, 363–386 (2017).
31. Janek, J. & Zeier, W. G. A solid future for battery development. *Nat. Energy* **1**, 1–4 (2016).
32. Cao, D. *et al.* Lithium Dendrite in All-Solid-State Batteries: Growth Mechanisms, Suppression Strategies, and Characterizations. *Matter* **3**, 57–94 (2020).

33. Lou, S. *et al.* Interface Issues and Challenges in All-Solid-State Batteries: Lithium, Sodium, and Beyond. *Adv. Mater.* **33**, 2000721 (2021).
34. Abakumov, A. M., Fedotov, S. S., Antipov, E. V. & Tarascon, J.-M. Solid state chemistry for developing better metal-ion batteries. *Nat. Commun.* **11**, 4976 (2020).
35. Liu, W., Placke, T. & Chau, K. T. Overview of batteries and battery management for electric vehicles. *Energy Rep.* **8**, 4058–4084 (2022).
36. Holt, A. & Kofstad, P. Electrical conductivity and defect structure of Cr2O3. II. Reduced temperatures (<~1000°C). *Solid State Ion.* **69**, 137–143 (1994).
37. Shi, T., Chen, Y. & Guo, X. Defect chemistry of alkaline earth metal (Sr/Ba) titanates. *Prog. Mater. Sci.* **80**, 77–132 (2016).
38. Hui, S. (Rob) *et al.* A brief review of the ionic conductivity enhancement for selected oxide electrolytes. *J. Power Sources* **172**, 493–502 (2007).
39. Minh, N. Q. Ceramic Fuel Cells. *J. Am. Ceram. Soc.* **76**, 563–588 (1993).
40. Kumar, P. P. & Yashonath, S. Ionic conduction in the solid state. *J. Chem. Sci.* **118**, 135–154 (2006).
41. Hu, Y.-S. Batteries: Getting solid. *Nat. Energy* **1**, 16042 (2016).
42. Manthiram, A., Yu, X. & Wang, S. Lithium battery chemistries enabled by solid-state electrolytes. *Nat. Rev. Mater.* **2**, 16103 (2017).
43. Mcgeehin, P. & Hooper, A. Fast ion conduction materials. *J. Mater. Sci.* **12**, 1–27 (1977).
44. Zheng, F., Kotobuki, M., Song, S., Lai, M. O. & Lu, L. Review on solid electrolytes for all-solid-state lithium-ion batteries. *J. Power Sources* **389**, 198–213 (2018).
45. Hong, H. Y.-P. Crystal structure and ionic conductivity of Li14Zn(GeO4)4 and other new Li+ superionic conductors. *Mater. Res. Bull.* **13**, 117–124 (1978).
46. Kuwano, J. & West, A. R. New Li+ ion conductors in the system, Li4GeO4-Li3VO4. *Mater. Res. Bull.* **15**, 1661–1667 (1980).
47. Petit, D., Colomban, Ph., Collin, G. & Boilot, J. P. Fast ion transport in LiZr2(PO4)3: Structure and conductivity. *Mater. Res. Bull.* **21**, 365–371 (1986).
48. El-Shinawi, H., Greaves, C. & Janek, J. Sol–gel synthesis and room-temperature properties of α-LiZr 2 (PO 4) 3. *RSC Adv.* **5**, 17054–17059 (2015).
49. Aono, H., Imanaka, N. & Adachi, G. High Li+ Conducting Ceramics. *Acc. Chem. Res.* **27**, 265–270 (1994).
50. Yoon, Y., Kim, J., Park, C. & Shin, D. The relationship of structural and electrochemical properties of NASICON structure Li1.3Al0.3Ti1.7 (PO4)(3) electrolytes by a sol-gel method | Request PDF. *J. Ceram. Process. Res.* **14**, 563–566 (2013).
51. Hartmann, P. *et al.* Degradation of NASICON-Type Materials in Contact with Lithium Metal: Formation of Mixed Conducting Interphases (MCI) on Solid Electrolytes. *J. Phys. Chem. C* **117**, 21064–21074 (2013).
52. Bonanos, N., Knight, K. S. & Ellis, B. Perovskite solid electrolytes: Structure, transport properties and fuel cell applications. *Solid State Ion.* **79**, 161–170 (1995).
53. Inada, R., Kimura, K., Kusakabe, K., Tojo, T. & Sakurai, Y. Synthesis and lithium-ion conductivity for perovskite-type Li3/8Sr7/16Ta3/4Zr1/4O3 solid electrolyte by powder-bed sintering. *Solid State Ion.* **261**, 95–99 (2014).
54. Chen, C. H. *et al.* Stable lithium-ion conducting perovskite lithium–strontium–tantalum–zirconium–oxide system. *Solid State Ion.* **167**, 263–272 (2004).

55. Phraewphiphat, T. *et al.* Syntheses, structures, and ionic conductivities of perovskite-structured lithium–strontium–aluminum/gallium–tantalum-oxides. *J. Solid State Chem.* **225**, 431–437 (2015).
56. Yu, R., Du, Q.-X., Zou, B.-K., Wen, Z.-Y. & Chen, C.-H. Synthesis and characterization of perovskite-type (Li,Sr)(Zr,Nb)O3 quaternary solid electrolyte for all-solid-state batteries. *J. Power Sources* **306**, 623–629 (2016).
57. Kasper, H. M. A new series of rare earth garnets Ln3+3M2Li+3O12(M = Te, W). *Inorg. Chem.* **8**, 1000–1002 (1969).
58. Murugan, R., Thangadurai, V. & Weppner, W. Fast Lithium Ion Conduction in Garnet-Type Li7La3Zr2O12. *Angew. Chem. Int. Ed.* **46**, 7778–7781 (2007).
59. Geiger, C. A. *et al. Inorg. Chem.* **50**, 1089–1097 (2011).
60. Buannic, L. *et al.* Dual Substitution Strategy to Enhance Li+ Ionic Conductivity in Li7La3Zr2O12 Solid Electrolyte. *Chem. Mater.* **29**, 1769–1778 (2017).
61. Larraz, G., Orera, A. & Sanjuán, M. L. Cubic phases of garnet-type Li7La3Zr2O12: the role of hydration. *J. Mater. Chem. A* **1**, 11419–11428 (2013).
62. Buschmann, H. *et al.* Structure and dynamics of the fast lithium ion conductor “Li7La3Zr2O12”. *Phys. Chem. Chem. Phys.* **13**, 19378–19392 (2011).
63. Ibarra, J. *et al.* Influence of composition on the structure and conductivity of the fast ionic conductors La2/3−xLi3xTiO3 (0.03≤x≤0.167). *Solid State Ion.* **134**, 219–228 (2000).
64. Kothari, D. H. & Kanchan, D. K. Effect of doping of trivalent cations Ga3+, Sc3+, Y3+ in Li1.3Al0.3Ti1.7 (PO4)3 (LATP) system on Li+ ion conductivity. *Phys. B Condens. Matter* **501**, 90–94 (2016).
65. Abrahams, I. & Bruce, P. G. Defect clustering in the superionic conductor lithium germanium vanadate. *Acta Crystallogr. B* **47**, 696–701 (1991).
66. Whittingham, M. S. Lithium Batteries and Cathode Materials. *Chem. Rev.* **104**, 4271–4302 (2004).
67. Miles, M. H. Recent advances in lithium battery technology. in *GaAs IC Symposium. IEEE Gallium Arsenide Integrated Circuit Symposium. 23rd Annual Technical Digest 2001 (Cat. No.01CH37191)* 219–222 (2001). doi:10.1109/GAAS.2001.964382.
68. Mizushima, K., Jones, P. C., Wiseman, P. J. & Goodenough, J. B. LixCoO2 (0. *Mater. Res. Bull.* **15**, 783–789 (1980).
69. Julien, C. M., Mauger, A., Zaghib, K. & Groult, H. Comparative Issues of Cathode Materials for Li-Ion Batteries. *Inorganics* **2**, 132–154 (2014).
70. Arai, H., Okada, S., Ohtsuka, H., Ichimura, M. & Yamaki, J. Characterization and cathode performance of Li1 − xNi1 + xO2 prepared with the excess lithium method. *Solid State Ion.* **80**, 261–269 (1995).
71. Gummow, R. J. & Thackeray, M. M. An Investigation of Spinel-Related and Orthorhombic LiMnO2 Cathodes for Rechargeable Lithium Batteries. *J. Electrochem. Soc.* **141**, 1178 (1994).
72. Zhu, X. *et al.* LiMnO2 cathode stabilized by interfacial orbital ordering for sustainable lithium-ion batteries. *Nat. Sustain.* **4**, 392–401 (2021).
73. Shizuka, K. *et al.* Characterization of Li1+yNixCo1−2xMnxO2 positive active materials for lithium ion batteries. *J. Power Sources* **146**, 589–593 (2005).
74. Oh, S. W., Park, S.-H., Amine, K. & Sun, Y.-K. Synthesis and characterization of spherical morphology [Ni0.4Co0.2Mn0.4]3O4 materials for lithium secondary batteries. *J. Power Sources* **160**, 558–562 (2006).

75. Kim, M.-H., Shin, H.-S., Shin, D. & Sun, Y.-K. Synthesis and electrochemical properties of Li[Ni0.8Co0.1Mn0.1]O2 and Li[Ni0.8Co0.2]O2 via co-precipitation. *J. Power Sources* **159**, 1328–1333 (2006).
76. Noh, H.-J., Youn, S., Yoon, C. S. & Sun, Y.-K. Comparison of the structural and electrochemical properties of layered Li[NixCoyMnz]O2 (x = 1/3, 0.5, 0.6, 0.7, 0.8 and 0.85) cathode material for lithium-ion batteries. *J. Power Sources* **233**, 121–130 (2013).
77. Li, T. *et al.* Degradation Mechanisms and Mitigation Strategies of Nickel-Rich NMC-Based Lithium-Ion Batteries. *Electrochem. Energy Rev.* **3**, 43–80 (2020).
78. Padhi, A. K., Nanjundaswamy, K. S., Masquelier, C., Okada, S. & Goodenough, J. B. Effect of Structure on the Fe3 + / Fe2 + Redox Couple in Iron Phosphates. *J. Electrochem. Soc.* **144**, 1609 (1997).
79. Zhang, W.-J. Structure and performance of LiFePO4 cathode materials: A review. *J. Power Sources* **196**, 2962–2970 (2011).
80. Li, G., Azuma, H. & Tohda, M. LiMnPO4 as the Cathode for Lithium Batteries. *Electrochem. Solid-State Lett.* **5**, A135 (2002).
81. Amine, K., Yasuda, H. & Yamachi, M. Olivine LiCoPO4 as 4.8 V Electrode Material for Lithium Batteries. *Electrochem. Solid-State Lett.* **3**, 178 (2000).
82. Vijaya Babu, K., Seeta Devi, L., Veeraiah, V. & Anand, K. Structural and dielectric studies of LiNiPO4 and LiNi0.5Co0.5PO4 cathode materials for lithium-ion batteries. *J. Asian Ceram. Soc.* **4**, 269–276 (2016).
83. Martha, S. K. *et al.* On the Thermal Stability of Olivine Cathode Materials for Lithium-Ion Batteries. *J. Electrochem. Soc.* **158**, A1115 (2011).
84. Yamada, A. *et al.* Olivine-type cathodes: Achievements and problems. *J. Power Sources* **119–121**, 232–238 (2003).
85. Ludwig, J. & Nilges, T. Recent progress and developments in lithium cobalt phosphate chemistry- Syntheses, polymorphism and properties. *J. Power Sources* **382**, 101–115 (2018).
86. Choy, J.-H., Kim, D.-H., Kwon, C.-W., Hwang, S.-J. & Kim, Y.-I. Physical and electrochemical characterization of nanocrystalline LiMn2O4 prepared by a modified citrate route. *J. Power Sources* **77**, 1–11 (1999).
87. Thackeray, M. M. Spinel Electrodes for Lithium Batteries. *J. Am. Ceram. Soc.* **82**, 3347–3354 (1999).
88. Shigemura, H. *et al.* Structure and Electrochemical Properties of LiFe x Mn2 − x O 4 (0 ⩽ x ⩽ 0.5) Spinel as 5 V Electrode Material for Lithium Batteries. *J. Electrochem. Soc.* **148**, A730 (2001).
89. Arora, P., Popov, B. N. & White, R. E. Electrochemical Investigations of Cobalt-Doped LiMn2 O 4 as Cathode Material for Lithium-Ion Batteries. *J. Electrochem. Soc.* **145**, 807 (1998).
90. Liu, D. *et al.* Spinel materials for high-voltage cathodes in Li-ion batteries. *RSC Adv.* **4**, 154–167 (2013).
91. Fergus, J. W. Recent developments in cathode materials for lithium ion batteries. *J. Power Sources* **195**, 939–954 (2010).
92. Moorhead-Rosenberg, Z., Chemelewski, K. R., Goodenough, J. B. & Manthiram, A. Magnetic measurements as a viable tool to assess the relative degrees of cation ordering and Mn3+ content in doped LiMn1.5Ni0.5O4 spinel cathodes. *J. Mater. Chem. A* **1**, 10745–10752 (2013).
93. Friedrich, F. *et al.* Editors' Choice—Capacity Fading Mechanisms of NCM-811 Cathodes in Lithium-Ion Batteries Studied by X-ray Diffraction and Other Diagnostics. *J. Electrochem. Soc.* **166**, A3760 (2019).

94. Yoshinari, T. *et al.* Quantitative Elucidation of the Non-Equilibrium Phase Transition in LiFePO4 via the Intermediate Phase. *Chem. Mater.* **31**, 7160–7166 (2019).
95. H, B., Jo, T., W, L. & Gc, F. A neutron diffraction study of Ni substituted LiMn2O4. *Solid State Ion.* **112**, 165–168 (1998).
96. McClelland, I. *et al.* In Situ Diffusion Measurements of a NASICON-Structured All-Solid-State Battery Using Muon Spin Relaxation. *ACS Appl. Energy Mater.* **4**, 1527–1536 (2021).
97. McClelland, I. *et al.* The Role of the Reducible Dopant in Solid Electrolyte–Lithium Metal Interfaces. *Chem. Mater.* **34**, 5054–5064 (2022).
98. Amores, M. *et al.* Li1.5La1.5MO6 (M = W6+, Te6+) as a new series of lithium-rich double perovskites for all-solid-state lithium-ion batteries. *Nat. Commun.* **11**, 6392 (2020).
99. Jansen, M. Conceptual Inorganic Materials Discovery – A Road Map. *Adv. Mater.* **27**, 3229–3242 (2015).
100. MacLeod, B. P., Parlane, F. G. L., Brown, A. K., Hein, J. E. & Berlinguette, C. P. Flexible automation accelerates materials discovery. *Nat. Mater.* **21**, 722–726 (2022).
101. McFarland, E. W. & Weinberg, W. H. Combinatorial approaches to materials discovery. *Trends Biotechnol.* **17**, 107–115 (1999).
102. West, A. R. *Solid State Chemistry and its Applications*. (Wiley-Blackwell, 2014).
103. Bunaciu, A. A., Udriştioiu, E. gabriela & Aboul-Enein, H. Y. X-Ray Diffraction: Instrumentation and Applications. *Crit. Rev. Anal. Chem.* **45**, 289–299 (2015).
104. Johnson, M. W. & David, W. I. F. *HRPD: the high resolution powder diffractometer at the SNS*. 23 (1985).
105. Rietveld, H. M. The Rietveld method. *Phys. Scr.* **89**, 098002 (2014).
106. Larson, A. C. & von Dreele, A. C. GSAS general structure analysis system operation manual. *ResearchGate* https://www.researchgate.net/publication/292406120_GSAS_general_structure_analysis_system_operation_manual.
107. Toby, B. H. & Von Dreele, R. B. GSAS-II: the genesis of a modern open-source all purpose crystallography software package. *J. Appl. Crystallogr.* **46**, 544–549 (2013).
108. *The Rietveld Method*. (Oxford University Press, 1995).
109. Yang, X. & Rogach, A. L. Electrochemical Techniques in Battery Research: A Tutorial for Nonelectrochemists. *Adv. Energy Mater.* **9**, 1900747 (2019).
110. Elgrishi, N. *et al.* A Practical Beginner's Guide to Cyclic Voltammetry. *J. Chem. Educ.* **95**, 197–206 (2018).
111. Palagonia, M. S., Erinmwingbovo, C., Brogioli, D. & La Mantia, F. Comparison between cyclic voltammetry and differential charge plots from galvanostatic cycling. *J. Electroanal. Chem.* **847**, 113170 (2019).
112. Gateman, S. M. *et al.* On the use of a constant phase element (CPE) in electrochemistry. *Curr. Opin. Electrochem.* **36**, 101133 (2022).
113. Hebb, M. H. Electrical Conductivity of Silver Sulfide. *J. Chem. Phys.* **20**, 185–190 (2004).
114. Tubandt, C. *Handb. Exp.* **12**, (1932).
115. Sayers, D. E., Stern, E. A. & Lytle, F. W. New Technique for Investigating Noncrystalline Structures: Fourier Analysis of the Extended X-Ray---Absorption Fine Structure. *Phys. Rev. Lett.* **27**, 1204–1207 (1971).

116. Reif, B., Ashbrook, S. E., Emsley, L. & Hong, M. Solid-state NMR spectroscopy. *Nat. Rev. Methods Primer* **1**, 1–23 (2021).
117. Bloembergen, N., Purcell, E. M. & Pound, R. V. Relaxation Effects in Nuclear Magnetic Resonance Absorption. *Phys. Rev.* **73**, 679–712 (1948).
118. El-Shinawi, H., Paterson, G. W., MacLaren, D. A., Cussen, E. J. & Corr, S. A. Low-temperature densification of Al-doped Li7La3Zr2O12: a reliable and controllable synthesis of fast-ion conducting garnets. *J. Mater. Chem. A* **5**, 319–329 (2016).
119. Hussain, F., Li, P. & Li, Z. Theoretical Insights into Li-Ion Transport in LiTa2PO8. *J. Phys. Chem. C* **123**, 19282–19287 (2019).
120. Huang, B. *et al.* Li-ion conductivity and stability of hot-pressed LiTa2PO8 solid electrolyte for all-solid-state batteries. *J. Mater. Sci.* **56**, 2425–2434 (2021).
121. Thompson, T. *et al.* A Tale of Two Sites: On Defining the Carrier Concentration in Garnet-Based Ionic Conductors for Advanced Li Batteries. *Adv. Energy Mater.* **5**, 1500096 (2015).
122. Thangadurai, V., Kaack, H. & Weppner, W. J. F. Novel Fast Lithium Ion Conduction in Garnet-Type Li5La3M2O12 (M = Nb, Ta). *J. Am. Ceram. Soc.* **86**, 437–440 (2003).
123. Li, Y., Han, J.-T., Wang, C.-A., Xie, H. & Goodenough, J. B. Optimizing Li+ conductivity in a garnet framework. *J. Mater. Chem.* **22**, 15357–15361 (2012).
124. Zhao, N. *et al.* Solid Garnet Batteries. *Joule* **3**, 1190–1199 (2019).
125. Logéat, A. *et al.* From order to disorder: The structure of lithium-conducting garnets Li7−xLa3TaxZr2−xO12 (x=0–2). *Solid State Ion.* **206**, 33–38 (2012).
126. Cussen, E. J. The structure of lithium garnets: cation disorder and clustering in a new family of fast Li+ conductors. *Chem. Commun.* **0**, 412–413 (2006).
127. El Shinawi, H. & Janek, J. Stabilization of cubic lithium-stuffed garnets of the type “Li7La3Zr2O12” by addition of gallium. *J. Power Sources* **225**, 13–19 (2013).
128. Shannon, R. D. Revised effective ionic radii and systematic studies of interatomic distances in halides and chalcogenides. *Acta Crystallogr. Sect. A* **32**, 751–767 (1976).
129. Yang, T. *et al.* The synergistic effect of dual substitution of Al and Sb on structure and ionic conductivity of Li7La3Zr2O12 ceramic. *Ceram. Int.* **44**, 1538–1544 (2018).
130. Hagman, L.-O., Kierkegaard, P., Karvonen, P., Virtanen, A. I. & Paasivirta, J. The Crystal Structure of NaM2IV(PO4)3; MeIV = Ge, Ti, Zr. *Acta Chem. Scand.* **22**, 1822–1832 (1968).
131. Aono, H., Sugimoto, E., Sadaoka, Y., Imanaka, N. & Adachi, G. Ionic Conductivity of Solid Electrolytes Based on Lithium Titanium Phosphate. *J. Electrochem. Soc.* **137**, 1023–1027 (1990).
132. Reiff, W. M., Zhang, J. H. & Torardi, C. C. Topochemical Lithium Insertion into Fe2(MoO4)3: Structure and Magnetism of Li2Fe2(MoO4)3. *J. Solid State Chem.* **62**, 231–240 (1986).
133. Barim, G., Cottingham, P., Zhou, S., Melot, B. C. & Brutchey, R. L. Investigating the Mechanism of Reversible Lithium Insertion into Anti-NASICON Fe2(WO4)3. *ACS Appl. Mater. Interfaces* **9**, 10813–10819 (2017).
134. Alvarez-Vega, M., Amador, U. & Dompablo, M. E. A. Electrochemical Study of Li3Fe(MoO4)3 as Positive Electrode in Lithium Cells. *J. Electrochem. Soc.* **152**, A1306–A1311 (2005).
135. Mikhailova, D. *et al.* Li3V(MoO4)3: A New Material for Both Li Extraction and Insertion. *Chem. Mater.* **22**, 3165–3173 (2010).

136. Feng, K., Wang, F., Zhang, H., Li, X. & Zhang, H. Li3Cr(MoO4)3: a NASICON-type high specific capacity cathode material for lithium ion batteries. *J. Mater. Chem. A* **6**, 19107–19112 (2018).
137. Prabaharan, S. R. S., Fauzi, A., Michael, M. S. & Begam, K. M. New NASICON-type Li2Ni2(MoO4)3 as a positive electrode material for rechargeable lithium batteries. *Solid State Ion.* **171**, 157–165 (2004).
138. El-Shinawi, H., Regoutz, A., Payne, D. J., Cussen, E. J. & Corr, S. A. NASICON LiM2(PO4)3 electrolyte (M = Zr) and electrode (M = Ti) materials for all solid-state Li-ion batteries with high total conductivity and low interfacial resistance. *J. Mater. Chem. A* **6**, 5296–5303 (2018).
139. Ozima, M., Sato, S. & Zoltai, T. The crystal structure of a lithium–nickel molybdate, Li2Ni2Mo3O12, and the systematics of the structure type. *Acta Crystallogr. Sect. B* **33**, 2175–2181 (1977).
140. Sebastian, L., Piffard, Y., Shukla, A. K., Taulelle, F. & Gopalakrishman, J. Synthesis, structure and lithium-ion conductivity of Li2-2xMg2+x(MoO4)3 and Li3M(MoO4)3 (M = Cr, Fe). *J. Mater. Chem.* **13**, 1797–1802 (2003).
141. Smit, J. P., McDonald, T. M. & Poeppelmeier, K. R. Li3Ti0.75(MoO4)3: A lyonsite-type oxide. *Solid State Sci.* **10**, 396–400 (2008).
142. Bugaris, D. E. & zur Loye, H.-C. Li3Al(MoO4)3, a lyonsite molybdate. *Acta Crystallogr. C* **68**, i34-36 (2012).
143. Gillie, L. J. *et al.* Synthesis, structural characterization and Li+ ion conductivity of a new vanado-molybdate phase, LiMg3VMo2O12. *J. Solid State Chem.* **183**, 2589–2597 (2010).
144. Sarapulova, A., Mikhailova, D., Senyshyn, A. & Ehrenberg, H. Crystal structure and magnetic properties of Li,Cr-containing molybdates Li3Cr(MoO4)3, LiCr(MoO4)2 and Li1.8Cr1.2(MoO4)3. *J. Solid State Chem.* **182**, 3262–3268 (2009).
145. Cussen, E., Corr, S., Clough, J., El-Shinawi, H. & Thomas, C. Earth Abundant NASICON Materials for Lithium Battery Applications, Li3Fe(MoO4)3 and Li1.6Mn2.2(MoO4)3. *STFC ISIS Neutron Muon Source* (2020).
146. Kresse, G. & Hafner, J. Ab initio molecular dynamics for liquid metals. *Phys. Rev. B* **47**, 558–561 (1993).
147. Blöchl, P. E. Projector augmented-wave method. *Phys. Rev. B* **50**, 17953–17979 (1994).
148. Perdew, J. P., Burke, K. & Ernzerhof, M. Generalized Gradient Approximation Made Simple. *Phys. Rev. Lett.* **77**, 3865–3868 (1996).
149. Dudarev, S. L., Botton, G. A., Savrasov, S. Y., Humphreys, C. J. & Sutton, A. P. Electron-energy-loss spectra and the structural stability of nickel oxide: An LSDA+U study. *Phys. Rev. B* **57**, 1505–1509 (1998).
150. Irvine, J. T. S., Sinclair, D. C. & West, A. R. Electroceramics: Characterization by Impedance Spectroscopy. *Adv. Mater.* **2**, 132–138 (1990).
151. Chen, S. *et al.* Lithiated bimetallic oxide, Li3Fe(MoO4)3, as a high-performance anode material for lithium-ion batteries and its multielectron reaction mechanism. *J. Power Sources* **476**, 228656 (2020).
152. Knauth, P. Inorganic solid Li ion conductors: An overview. *Solid State Ion.* **180**, 911–916 (2009).
153. Gong, Z. & Yang, Y. Recent advances in the research of polyanion-type cathode materials for Li-ion batteries. *Energy Environ. Sci.* **4**, 3223–3242 (2011).

154. Padhi, A. K., Nanjundaswamy, K. S. & Goodenough, J. B. Phospho-olivines as Positive-Electrode Materials for Rechargeable Lithium Batteries. *J. Electrochem. Soc.* **144**, 1188 (1997).
155. Nytén, A., Abouimrane, A., Armand, M., Gustafsson, T. & Thomas, J. O. Electrochemical performance of Li2FeSiO4 as a new Li-battery cathode material. *Electrochem. Commun.* **7**, 156–160 (2005).
156. Recham, N. *et al.* A 3.6 V lithium-based fluorosulphate insertion positive electrode for lithium-ion batteries. *Nat. Mater.* **9**, 68–74 (2010).
157. Smit, J. P., Stair, P. C. & Poeppelmeier, K. R. The Adaptable Lyonsite Structure. *Chem. – Eur. J.* **12**, 5944–5953 (2006).
158. Dompablo, M. E. A. y de, Alvarez-Vega, M., Baehtz, C. & Amador, U. Structural Evolution of Li3+xFe(MoO4)3 upon Lithium Insertion in the Compositional Range $0 \leqslant x \leqslant 1$. *J. Electrochem. Soc.* **153**, A275–A281 (2006).
159. Ravel, B. & Newville, M. ATHENA, ARTEMIS, HEPHAESTUS: data analysis for X-ray absorption spectroscopy using IFEFFIT. *J. Synchrotron Radiat.* **12**, 537–541 (2005).
160. Catti, M. & Montero-Campillo, M. First-principles modelling of lithium iron oxides as battery cathode materials. *J. Power Sources* **196**, 3955–3961 (2011).
161. Zhou, W., Wang, Y., Zhang, L., Song, G. & Cheng, S. Capacitive nanosized spinel α-LiFe5O8 as high performance cathodes for lithium-ion batteries. *Int. J. Electrochem. Sci.* **10**, 5061–5068 (2015).
162. Armstrong, A. R., Tee, D. W., La Mantia, F., Novák, P. & Bruce, P. G. Synthesis of Tetrahedral LiFeO2 and Its Behavior as a Cathode in Rechargeable Lithium Batteries. *J. Am. Chem. Soc.* **130**, 3554–3559 (2008).
163. Li, J., Luo, J., Wang, L. & He, X. Recent Advances in the LiFeO2-based Materials for Li-ion Batteries. *Int. J. Electrochem. Sci.* **6**, 1550–1561 (2011).
164. Sakurai, Y., Arai, H., Okada, S. & Yamaki, J. Low temperature synthesis and electrochemical characteristics of LiFeO2 cathodes. *J. Power Sources* **68**, 711–715 (1997).
165. Lee, Y. S., Sato, S., Sun, Y. K., Kobayakawa, K. & Sato, Y. A new type of orthorhombic LiFeO2 with advanced battery performance and its structural change during cycling. *J. Power Sources* **119–121**, 285–289 (2003).
166. Lee, Y. S. *et al.* Structural change and capacity loss mechanism in orthorhombic Li/LiFeO2 system during cycling. *Electrochem. Commun.* **5**, 549–554 (2003).
167. Kanno, R. *et al.* Synthesis, Structure, and Electrochemical Properties of a New Lithium Iron Oxide, LiFeO2, with a Corrugated Layer Structure. *J. Electrochem. Soc.* **143**, 2435 (1996).
168. Johnson, C. S. *et al.* Li2O Removal from Li5FeO4: A Cathode Precursor for Lithium-Ion Batteries. *Chem. Mater.* **22**, 1263–1270 (2010).
169. Zhang, Q. *et al.* Excess Li2O Additives to Promote Grain Boundary Growth and Improve Ionic Conductivity of LiTa2PO8 Solid Electrolytes. *Front. Mater.* **8**, (2021).
170. Na, Y. *et al.* Novel fast lithium-ion conductor LiTa2PO8 enhances the performance of poly(ethylene oxide)-based polymer electrolytes in all-solid-state lithium metal batteries. *Chin. Chem. Lett.* **33**, 4037–4042 (2022).
171. Xiao, Z., Chi, Z., Song, L., Cao, Z. & Li, A. LiTa2PO8 coated nickel-rich cathode material for improved electrochemical performance at high voltage. *Ceram. Int.* (2019) doi:10.1016/j.ceramint.2019.12.064.
172. Ge, X. *et al.* Li2Ni(WO4)2/C: A potential tungstate anode material for lithium ion batteries. *J. Alloys Compd.* **888**, 161535 (2021).

173. Li, C.-L. & Fu, Z.-W. Electrochemical characterization of amorphous LiFe(WO4)2 thin films as positive electrodes for rechargeable lithium batteries. *Electrochimica Acta* **53**, 6434–6443 (2008).